

# Detection of Gravitational Anomaly at Low Acceleration from a Highest-quality Sample of 36 Wide Binaries with Accurate 3D Velocities

K.-H. CHAE , <sup>1,\*</sup> B.-C. LEE, <sup>2</sup> X. HERNANDEZ, <sup>3</sup> V. G. ORLOV, <sup>3</sup> D. LIM, <sup>4</sup> D. A. TURNSHEK, <sup>5,6</sup> AND Y.-W. LEE<sup>4,7</sup>

<sup>1</sup>Department of Physics and Astronomy, Sejong University, 209 Neungdong-ro Gwangjin-gu, Seoul 05006, Republic of Korea

<sup>2</sup>Korea Astronomy and Space Science Institute, 776 Daedeokdae-ro, Yuseong-gu, Daejeon 34055, Republic of Korea

<sup>3</sup>Universidad Nacional Autónoma de México, Instituto de Astronomía, A. P. 70-264, 04510, CDMX, México

<sup>4</sup>Center for Galaxy Evolution Research, Yonsei University, 50 Yonsei-ro, Seodaemun-gu, Seoul 03722, Republic of Korea

<sup>5</sup>Department of Physics and Astronomy, University of Pittsburgh, Pittsburgh, PA 15260, USA

<sup>6</sup>Pittsburgh Particle Physics, Astrophysics, and Cosmology Center (PITT PACC), Pittsburgh, PA 15260, USA

<sup>7</sup>Department of Astronomy, Yonsei University, 50 Yonsei-ro, Seodaemun-gu, Seoul 03722, Republic of Korea

## ABSTRACT

We set out to accurately measure gravity in the low-acceleration range ( $10^{-11}, 10^{-9}$ )  $\text{m s}^{-2}$  from 3D motions of isolated wide binary stars. Gaia DR3 provides precise measurements of the four sky-plane components of the 3D relative displacement and velocity ( $\mathbf{r}, \mathbf{v}$ ) for a wide binary, but not comparably precise line-of-sight (radial) separation and relative velocity  $v_r$ . Based on our new observations and the public databases/publications, we assemble a sample of 36 nearby (distance  $< 150\text{pc}$ ) wide binaries in the low-acceleration regime with accurate values of  $v_r$  (uncertainty  $< 100 \text{ m s}^{-1}$ ). Kinematic contaminants such as undetected stellar companions are well under control using various observational diagnostics such as Gaia's `ruwe` parameter, the color-magnitude diagram, multi-epoch observations of radial velocities, Speckle interferometric follow-up observations, and requiring Hipparcos-Gaia proper motion consistency. For the parameter  $\Gamma \equiv \log_{10} \sqrt{\gamma}$  with  $\gamma \equiv G/G_N$  (where  $G$  is a parameter generalizing Newton's constant  $G_N$  in elliptical orbits), we find  $\Gamma = 0.102^{+0.023}_{-0.021}$ , inconsistent with standard gravity at  $4.9\sigma$ , giving a gravity boost factor of  $\gamma = 1.600^{+0.171}_{-0.141}$  under the assumption of elliptical orbits and angular momentum conservation. Four wide binaries have 3D relative velocities exceeding their estimated Newtonian escape velocities with  $1 < v_{\text{obs}}/v_{\text{escN}} \leq 1.2$ . These systems are unlikely to be chance associations and are expected in a nonstandard paradigm such as Milgromian dynamics (MOND). The hypothesis that Newtonian gravity can be extrapolated to the low-acceleration limit is falsified by this independent study with accurate 3D velocities. Future radial velocity monitoring and Speckle interferometric imaging for larger samples will be useful to refine the present result.

**Keywords:** Binary stars (154) — Gravitation (661) — Modified Newtonian dynamics (1069) — Non-standard theories of gravity (1118) — Wide binary stars (1801)

## 1. INTRODUCTION

Einstein (A. Einstein 1916) invented general relativity as a relativistic theory of gravity whose nonrelativistic limit is Poisson's equation, Newtonian gravitation. For the past century this Newton-Einstein standard gravity has been the basis for the modern cosmological paradigm and the requirement of dark matter from astronomical observations. However, Newtonian gravity applicable in the nonrelativistic regime was based on the empirical laws of planetary motions (discovered by Kepler four centuries ago) in the high-acceleration  $g_N > 10^{-7} \text{ m s}^{-2}$  regime. Hereafter,  $g_N$  refers to Newton's constant ( $G_N$ )

times mass over distance squared for the system under consideration, i.e.,  $g_N = G_N M_{\text{tot}}/r^2$  for a binary with total mass  $M_{\text{tot}}$  and 3D separation  $r$ .

From an empirical point of view, Poisson's equation was shown to be broken by Le Verrier's work as gravity gets sufficiently strong, already in the 19th century even before any relativistic theory existed. While a relativistic theory is successful in the strong-gravity regime, the hypothesis that Poisson's equation can be extrapolated indefinitely into the low-acceleration limit requires a direct empirical verification. General relativity's success in strong-gravity regimes does not guarantee its correctness in the low-acceleration limit (perhaps, as the classically perfect theory of Maxwell's electrodynamics has fundamental limitations). Any piece of scientific truth is eventually determined by experimental/observational

\* corresponding author: chae@sejong.ac.kr  
 kyuhyunchae@gmail.com

facts. The same holds for any hypothetically dominant dark matter component as introduced to force agreement with standard gravity, hence the ongoing worldwide campaigns attempting a direct detection of any such component (see, e.g., the report by [J. Billard et al. 2022](#) and Section 27 of [S. Navas et al. 2024](#)), without any positive signal up to now (e.g., [N. Carlin et al. 2025](#)).

Milgrom ([M. Milgrom 1983](#)) first noticed/suggested that galactic rotation curves start to deviate significantly from Newton's  $r^{-2}$  law only around a critical acceleration  $a_0$  near  $10^{-10} \text{ m s}^{-2}$ . Milgrom's proposal, known as modified Newtonian dynamics (MOND), posits a modification of standard gravitational dynamics in the low acceleration regime to break the strong equivalence principle (while keeping Einstein's equivalence principle and Galileo's universality of free fall) and makes a number of salient predictions for gravitational dynamics in astrophysical systems ([R. H. Sanders & S. S. McGaugh 2002](#); [B. Famaey & S. S. McGaugh 2012](#); [I. Banik & H. Zhao 2022](#); [D. Merritt 2020](#)), including the idiosyncratic external field effects (EFE; [M. Milgrom 1983](#); [K.-H. Chae & M. Milgrom 2022](#)) in the internal dynamics of freely falling systems under external fields.

Wide binary stars provide a unique probe to test standard gravity and MOND, as first proposed in [X. Hernandez et al. \(2012\)](#), with more recent examples such as [R. Scarpa et al. \(2017\)](#); [C. Pittordis & W. Sutherland \(2018\)](#); [I. Banik & H. Zhao \(2018\)](#). From a theoretical point of view, binaries of point-like masses are the simplest possible systems to test gravity, and wide binaries can have sufficiently low internal acceleration to probe the 'dark matter' regime, while any conceivable effect of hypothetical dark matter is negligible, given the stringent limits on this component locally, coming from observed vertical kinematics of disk stars (e.g., [J. I. Read 2014](#)). From an observational point of view, these binaries can be found in the solar neighborhood, so that their distances are directly measurable (an unusual advantage in astronomy) and their velocities can be measured with a sufficiently good precision.

The advent of the Gaia Data Release 3 (DR3; [A. Vallenari et al. 2023](#)) database ignited intensive wide binary gravity tests in recent years. Because Gaia DR3 does not generally provide sufficiently precise line-of-sight (radial) velocities, several statistical methods have been developed based only on sky-plane (tangential) velocities  $v_p$  (for a summary of the methods, see Table 3 of [K.-H. Chae 2025a](#)). Because gravity is sensitive to the 3D relative velocity  $\mathbf{v}$  between the pair at the 3D displacement  $\mathbf{r}$ , use of  $v_p$  does not allow any meaningful gravitational inference from individual wide binaries whose very long orbital periods preclude anything but essentially instantaneous observations. Thus, statistical methods requiring large numbers of wide binaries have been introduced to deal with the issues of projection effects (of  $\mathbf{v}$  onto  $v_p$ ), orbital orientation, phase occu-

pency, and false binaries (i.e. gravitationally-unbound fly-bys or chance associations).

All statistical analyses of binaries ([K.-H. Chae 2023, 2024a,b](#); [X. Hernandez 2023](#); [X. Hernandez et al. 2024b](#); [X. Hernandez & P. Kroupa 2025](#); [Y. Yoon et al. 2025](#)) covering a sufficiently broad dynamic range to include both high ( $g_N > 10^{-8} \text{ m s}^{-2}$ ) and low ( $g_N < 10^{-9} \text{ m s}^{-2}$ ) acceleration regimes show that the median value of  $v_p$  (or related quantity) is boosted about 20% in the low-acceleration regime as long as the fraction of hierarchical systems  $f_{\text{multi}}$  (with stellar multiplicity  $\geq 3$ ) is calibrated/checked using the binaries in the high-acceleration regime, regardless of the sample choices that largely dictate  $f_{\text{multi}}$ . See [X. Hernandez et al. \(2024a\)](#) for a critical review of some divergent results that are not based on the calibration of  $f_{\text{multi}}$  and do not include internal validation checks through the presence of a high acceleration Newtonian region.

Although statistical methods with  $v_p$  have been popular, it is clearly desirable to use directly measured 3D velocity  $\mathbf{v}$  for gravity tests because individual systems can be analyzed and understood in greater detail, leading to much more accurate gravity inferences. Recently, [K.-H. Chae \(2025a,b\)](#) developed a Bayesian 3D modeling methodology to infer probability density functions (PDFs) of gravity in individual systems (individually not highly restrictive broad distributions) and then to statistically consolidate them to derive the effective strength of gravity in a common acceleration regime. [K.-H. Chae \(2025a\)](#) first carried out an extensive study of 312 wide binaries using a simplified 3D model based on the Gaia DR3 3D velocities, which include relatively less precise radial velocities (RVs), and found a dichotomy such that 125 wide binaries in the strong acceleration regime  $g_N \gtrsim 10^{-8} \text{ m s}^{-2}$  agree well with Newton, while 111 wide binaries in the transition and low-acceleration regimes show a  $4.2\sigma$  anomaly. [K.-H. Chae \(2025b\)](#) carried out a pilot study of 32 wide binaries with a fully general 3D model based on accurate 3D velocities including precise HARPS RVs from [R. Saglia et al. \(2025\)](#), and found a moderate indication of dichotomy that 8 wide binaries with  $g_N < 10^{-9} \text{ m s}^{-2}$  show a gravity boost while 24 wide binaries with  $g_N > 10^{-9} \text{ m s}^{-2}$  agree well with Newton.

The key to a reliable inference of gravity with 3D motions of wide binaries is the construction of a sample of pure binaries free of undetected kinematic contaminants, such as unresolved companion stars or resolvable but too faint stars. In this work we employ an unprecedented combination of observational diagnostics to have a full control of potential kinematic contaminants. They include not only well-known diagnostics such as imposing a color-magnitude diagram (CMD) exclusion region and Gaia's  $\text{ruwe}$  limit, but also multi-epoch observations of radial velocities over more than several years and detailed Speckle interferometric imaging of the stars of many wide binaries. These diagnostics work together

to flag close/unresolved contaminants (within tens of au from the star) and more distant contaminants.

For the first time we carry out Speckle observations of 391 wide binaries selected from recent samples used by two of us (e.g., X. Hernandez et al. 2024b; K.-H. Chae 2024a). These observations form part of an ongoing campaign to image wide binaries at the diffraction limit of the 2.1 m telescope at the Observatorio Astronomico Nacional (SPM) using Speckle interferometry. These speckle observations will not only flag certain individual binaries but also give us the measured probability that the stringently selected samples will have resolvable faint companions. On the other hand, we collect as many high-precision radial velocities measured with different telescopes and, more importantly, at different epochs separated by at least several years. The collection includes our new observations of 60 wide binaries with the Las Cumbres Observatory (LCO) Network of Robotic Echelle Spectrographs (NRES) and 6 wide binaries with the GEMINI-North Observatory MAROON-X spectrograph (hereafter MAROON-X). It also includes wide binaries with radial velocities selected from HARPS (R. Saglia et al. 2025), SDSS4 DR17 APOGEE (hereafter APOGEE),<sup>1</sup> and R. Scarpa et al. (2017). In addition, we use the comparison of Hipparcos and Gaia proper motions to have a control in the selection process.

Since many previous studies (e.g., K.-H. Chae 2024a,b; Y. Yoon et al. 2025; K.-H. Chae 2025a,b) of wide binaries including the recent 3D analyses already confirm that Newton is verified at least for  $g_N > 10^{-8} \text{ m s}^{-2}$ , we focus on the low-acceleration regime only. We construct an extremely curated sample of 36 pure wide binaries in the low-acceleration regime that have accurate and precise relative RVs with measurement error  $< 100 \text{ m s}^{-1}$ . Our new sample is  $\approx 4$  times as large as the R. Saglia et al. (2025) sample of wide binaries having radial velocity measurements in the low-acceleration regime, with comparable data qualities, and thus our inferred constraints on gravity can be expected to have twice the precision than the pilot study by K.-H. Chae (2025b).

In Section 2 we briefly describe theoretical motivations and the Bayesian 3D modeling methodology. In Section 3, we describe the process of selecting the statistical sample of wide binaries to be used for gravity inference. We present the results on inferred gravity and relevant discussions in Section 4. We give our thoughts on the meanings and implications of the results in Section 5 and conclude in Section 6 with a future outlook. The Python codes used in this work can be found at K.-H. Chae (2025c), and the observational data for our sample and the Bayesian outputs will be available on Zenodo under an open-source Creative Commons Attribution license. In Appendices A, B, C, and D, we describe the

observations or collections of RVs. In Appendix E, we describe the Speckle interferometric observations.

## 2. THEORETICAL MOTIVATION AND THE 3D MODELING METHODOLOGY

In this work we set out to measure gravity in the low-acceleration regime in the context of distinguishing between standard and nonstandard theories of gravity. Although MOND is not yet an established physical theory of relativistic gravity (not to mention quantum gravity), it is useful to consider nonrelativistic MOND models as modifications of standard gravity in the low-acceleration regime. MOND predicts that the  $r^{-2}$  law with Newton's constant  $G_N$  will no longer hold in the acceleration regime  $g_N \lesssim 10^{-9} \text{ m s}^{-2}$ . According to MOND, how gravity will behave depends on the details of the EFE. For a truly isolated system without an external field, the gravity law will gradually switch to a  $r^{-1}$  behavior between  $10^{-8} \lesssim g_N \lesssim 10^{-10} \text{ m s}^{-2}$ . In reality, common dynamical systems such as binary stars and galaxies can be subject to external fields of various strength, and consequently, in the regime of low internal acceleration, gravity is predicted by MOND to become pseudo-Newtonian, showing an  $r^{-2}$  behavior with a rescaled gravitational parameter  $G(> G_N)$  that depends on the external field (see, e.g., K.-H. Chae & M. Milgrom 2022 for specific numerical examples).

In the case of wide binaries in the solar neighborhood, the external field due to the Galaxy is  $\approx 1.8a_0$ , which is so strong in the context of MOND that the gravity boost factor is expected to be about  $G/G_N \approx 1.4$  for a test particle (e.g., I. Banik & H. Zhao 2018; K.-H. Chae & M. Milgrom 2022). Complete numerical solutions for a two-body dynamics under an external field (due to a third body) find a lower boost factor of  $1.2 - 1.3$  (J. Pfamm-Altenburg 2025) using the QUMOND formalism (M. Milgrom 2010).

To test Newtonian and MOND predictions for wide binaries of the solar neighborhood, it is convenient to approximate instantaneous orbits as elliptical even if global orbits deviate from closed ellipses as in the MOND case (J. Pfamm-Altenburg 2025). While this assumption is perfectly valid in testing Newtonian gravity, any result deviating from Newton needs to be interpreted correctly in the context of testing MOND models such as AQUAL (J. Bekenstein & M. Milgrom 1984) and QUMOND (M. Milgrom 1983), or any other alternative model of gravity of interest. Regardless of the details of any modified gravity theory, an approach, in which a  $G \rightarrow \gamma G_N$  model is tested, will reveal the presence of a gravitational anomaly if the inferred value of  $\gamma \neq 1$ .

We use the 3D modeling methodology of K.-H. Chae (2025a,b) that infers PDFs  $p_i(\Gamma)$  ( $i = 1, \dots, N_{\text{binary}}$ ) of the parameter

$$\Gamma \equiv \log_{10} \sqrt{\gamma} \equiv \log_{10} \sqrt{G/G_N} \quad (1)$$

<sup>1</sup> <https://www.sdss4.org/dr17/irspecc/radialvelocities/>

for individual systems (along with orbit and orientation parameters: see Figure 1) and then statistically consolidate them through a normalized product of  $p_i$ .

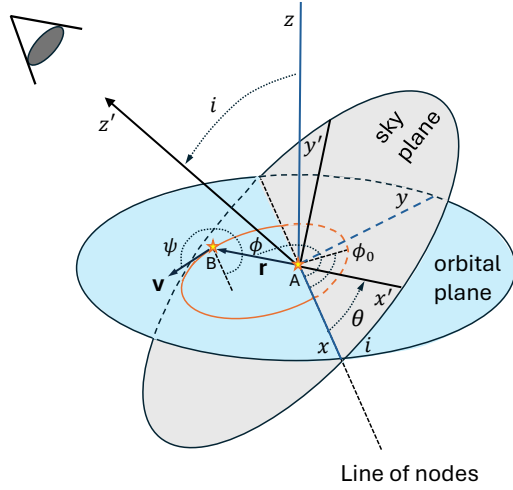


**Figure 1.** (Adapted from K.-H. Chae (2025b)) A general 3D geometry of an elliptical orbit. Here  $z'$  represents the line-of-sight (radial) direction in observer's frame with the + sign indicating the direction pointing to the observer. The relative radial velocity refers to  $v_{z'} (\equiv v_r)$ . See K.-H. Chae (2025b) for the definition of all the other parameters.

Here we briefly describe the essential points of the methodology and refer the reader to K.-H. Chae (2025a,b) for the details. Each binary has the six measured quantities of  $\mathbf{r} = \{x', y', z'\}$  and  $\mathbf{v} = \{v_{x'}, v_{y'}, v_{z'}\}$ , where  $x'$  and  $y'$  are (nearly) exact,  $v_{x'}$ ,  $v_{y'}$ , and  $v_{z'}$  are very precise, and  $z'$  is usually not so precise. Taking advantage of the fact that  $x'$  and  $y'$  are fixed by the data, we have a reduced set of free parameters  $\Theta = \{e, i, \phi_0, \Delta\phi (\equiv \phi - \phi_0), \log_{10} f_M, \Gamma\}$ , where  $e$  is the eccentricity with the range  $(0, 1)$ ,  $i$  is the inclination with the range  $(0^\circ, 180^\circ)$ ,  $\phi_0$  is the phase of the periastron with the range  $(0^\circ, 360^\circ)$ , and  $\Delta\phi$  is the phase relative to  $\phi_0$  known as the true anomaly with the range  $(0^\circ, 360^\circ)$ .<sup>2</sup> Here  $f_M$  represents the total mass of the binary system normalized by the observational mass. Inclusion of the parameter  $f_M$  in the Bayesian modeling means that we are allowing a probability distribution of mass (hence including a confidence interval on this parameter for each binary) with its prior set at the observationally inferred value.

<sup>2</sup> We note that the angle parameter  $\theta$  shown in Figure 1, which is related to the argument of the ascending node, can be calculated as a function of the free parameters.

The posterior probability of the parameters  $p(\Theta)$  is defined by

$$\ln p(\Theta) = \ln \mathcal{L} + \sum_l \ln f_{\text{pr}}(\Theta_l), \quad (2)$$

where  $\mathcal{L}$  is the likelihood function (connecting the free parameters with  $\mathbf{r}$  and  $\mathbf{v}$ ) whose details can be found in K.-H. Chae (2025b), and  $f_{\text{pr}}(\Theta_l)$  ( $l = 1, \dots, 6$ ) is the prior probability for the parameter  $\Theta_l$ . The imposed priors are as follows:  $f_{\text{pr}}(i) = \sin(i)$  (isotropic orientation),  $f_{\text{pr}}(\phi_0) = \text{uniform}$  (random orientation), and

$$f_{\text{pr}}(\Delta\phi) = \frac{(1-e^2)^{3/2}}{2\pi} \frac{1}{[1+e\cos(\Delta\phi)]^2}, \quad (3)$$

a phase occupancy probability which is inversely proportional to the scalar velocity at any given phase. Equation (3) ensures that each instantaneous motion being observed occurs at a random time during its orbital period. We also impose priors on  $e$ ,  $f_M$ , and  $\Gamma$  as follows:  $f_{\text{pr}}(e) = (1 + \alpha)e^\alpha$  taking  $\alpha = 1$  (the thermal probability distribution) as the nominal choice but considering also a full range of possibilities given by  $0 \leq \alpha \leq 1.3$  (as inferred by [H.-C. Hwang et al. \(2022\)](#) for wide binaries of the solar neighborhood), a normal probability distribution of  $\log_{10} f_M$  with  $(\mu, \sigma) = (0, 0.021)$  (i.e. 5% scatter in the observational total mass), and a uniform distribution of  $\Gamma$  in the range  $-1 < \Gamma < 1$ . We note that only the flat prior is considered for  $\Gamma$  when we seek to measure it from the binary dynamics data.

We will mainly focus on measuring gravity at low acceleration by deriving the PDF of  $\Gamma$  while treating the rest of the parameters as essentially nuisance parameters. To ensure an unbiased inference of  $\Gamma$ , it is necessary to use proper priors on the nuisance parameters as given above (in particular, the priors on inclination  $i$  and orbit true anomaly  $\Delta\phi$ ). For example, observational identification of a wide binary is blind to inclination or orbit true anomaly, so a sufficiently large sample of wide binaries should follow the distributions expected from randomness. Thus, the posterior PDFs of the nuisance parameters will provide internal self-consistency checks of the results.

As an auxiliary analysis, we will also carry out Bayesian modeling of the observed 3D motions at fixed gravity models with fixed values of  $\Gamma$  including  $\Gamma = 0$  (i.e., the Newtonian case). The primary purpose of this auxiliary analysis will be to estimate the Newtonian escape velocity for each binary at a fixed Newtonian or pseudo-Newtonian gravity model. We will use the estimated Newtonian escape velocities in conjunction with various observational diagnostics to assemble gravitationally-bound pure binary systems, as will be described in the next section. The pilot study by [K.-H. Chae \(2025b\)](#) based on the benchmark sample by [R. Saglia et al. \(2025\)](#) will provide a guidance in this regard. In particular, the [R. Saglia et al. \(2025\)](#) (sub)sample

of 8 (or 9) wide binaries in the low-acceleration regime ( $< 10^{-9} \text{ m s}^{-2}$ ) includes one system where the observed 3D velocity exceeds the Newtonian escape velocity by about 12%. That system is, however, extremely unlikely to be a chance association in the 3D space based on various observational diagnostics and statistical properties of the solar neighborhood. It will be interesting to see how our enlarged sample turns out to be.

### 3. ASSEMBLING A CAREFULLY CURATED WIDE BINARY SAMPLE WITH ACCURATE 3D VELOCITIES

To probe gravity in the low-acceleration regime through 3D modeling of wide binaries, we need kinematically uncontaminated pure binaries with accurate and precise values of the 6 components of  $\mathbf{r}$  and  $\mathbf{v}$  (Figure 1). Since the currently available observation facilities do not permit a sufficiently precise measurement of radial separation  $z'$ , it is unavoidable to work with only 5 precise components along with generally imprecise  $z'$ . Because Gaia DR3 provides sufficiently precise values for the 4 sky-projected quantities  $x'$ ,  $y'$ ,  $v_{x'}$ , and  $v_{y'}(\equiv v_{z'}) = -(RV_B - RV_A)$  where  $RV_A$  and  $RV_B$  are, respectively, the RVs of the brighter and fainter components relative to the Sun in the usual sense of the sign (i.e., the positive sign representing the direction of moving away from the Sun). Throughout, the brighter and fainter components are denoted by  $A$  and  $B$ , respectively.

To collect *pure* wide binaries with accurate and precise  $v_r$  in the low-acceleration regime, we follow three steps. In the first step, we collect as many as possible wide binaries with relatively precise RVs for both components and carry out Bayesian modeling for all the systems. In the second step, we select wide binaries that have low internal acceleration ( $< 10^{-9} \text{ m s}^{-2}$  based on the Bayesian modeling results) and pass the basic observational criteria required for pure binaries. In the final step, we select the clean sample that is most likely to be free from any kinematic contamination based on various observational diagnostics and the Bayesian modeling results.

#### 3.1. Step 1: Construction of a large sample of wide binaries with relatively precise radial velocities

The collection includes our new observations carried out during 2024-2025 as well as public database/publications. New RVs are available for 60 wide binaries from LCO (Appendix A) and for 6 wide binaries from MAROON-X (Appendix B). For the case of LCO observations, RVs were measured independently at two epochs separated by a few months for 18 of them. We also collect wide binaries with

precise RVs from public databases and individually published results: 195 wide binaries within 300 pc from APOGEE (Appendix D), 32 wide binaries with HARPS RVs from R. Saglia et al. (2025), and 24 wide binaries from R. Scarpa et al. (2017) after excluding obvious chance-alignment and kinematically contaminated cases (see Appendix C). Because some wide binaries are included more than once in various samples, we have 306 unique wide binaries with relatively precise RVs (compared to Gaia DR3 RVs). This combined sample will be our raw or scratch sample.

Figure 2 shows the distribution of the reported nominal uncertainties of  $v_r$  for the systems in the raw sample. All systems satisfy  $\sigma_{v_r} < 350 \text{ m s}^{-1}$  by selection, and the majority have  $\sigma_{v_r} < 100 \text{ m s}^{-1}$ . Table 1 lists wide binaries for which independent measurements of  $v_r$  were made with different instruments at different epochs. Time baselines between different observations considered in this work are summarized in Figure 3. For all but one system (the fourth) two independent values are consistent with each other. The first (obs1) values may be more accurate (and are more precise in most cases), and so only the first values are included in the raw sample. The fourth system (Gaia DR3 5607190344506642432 & 5607189485513198208) with the HARPS value of  $v_r = -0.080 \pm 0.003 \text{ km s}^{-1}$  from R. Saglia et al. (2025) will be used despite the inconsistency with the Scarpa value of  $v_r = -0.441 \pm 0.032 \text{ km s}^{-1}$  from R. Scarpa et al. (2017), because the HARPS measurements are generally reliable and the HARPS value is consistent with the Gaia DR3<sup>3</sup> value of  $v_r = -0.290 \pm 0.184 \text{ km s}^{-1}$ .

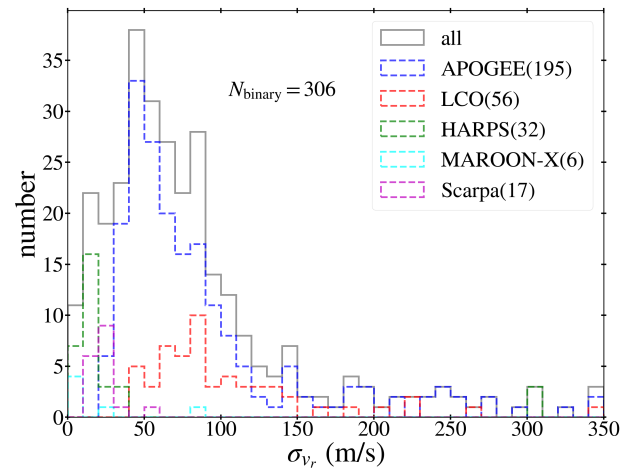


**Figure 2.** The distribution of nominal uncertainties of  $v_r(\equiv RV_A - RV_B)$  for the raw sample of 306 unique wide binaries assembled from various observations and database/publications.

**Table 1. Wide binaries with two measurements of  $v_r$  from independent observations with different instruments**

Gaia DR3 identifier Star A	Gaia DR3 identifier Star B	$s^a$	$v_r^b$	$v_r^b$	obs1/obs2 <sup>c</sup>	time baseline <sup>d</sup> [yr]
		[kau]	[km s $^{-1}$ ]	[km s $^{-1}$ ]		
2776055105362407680	2776054899203977728	4.83	$-0.468 \pm 0.017$	$-0.605 \pm 0.150$	HARPS/LCO	3
4940794866807373952	4940794488850252928	4.94	$0.449 \pm 0.004$	$0.387 \pm 0.069$	HARPS/LCO	3
5060104351007433472	5060105897197110144	9.08	$-0.254 \pm 0.035$	$-0.377 \pm 0.024$	HARPS/Scarpa	5
5607190344506642432	5607189485513198208	12.33	$-0.080 \pm 0.003$	$-0.441 \pm 0.032$	HARPS/Scarpa	5
3285218186904332288	3285218255623808640	1.42	$0.590 \pm 0.017$	$0.572 \pm 0.020$	HARPS/Scarpa	5
4249652990144051840	4249652783985617920	2.74	$0.140 \pm 0.004$	$0.061 \pm 0.026$	HARPS/Scarpa	5
2201661297490051968	2201661091331626752	8.37	$-0.018 \pm 0.006$	$0.002 \pm 0.110$	MAROON-X/LCO	0.3
1172915990414659328	1172920487244742912	24.68	$0.043 \pm 0.033$	$-0.027 \pm 0.077$	APOGEE/LCO	6
1282815063829295360	1282817022334383232	16.77	$-0.283 \pm 0.041$	$-0.170 \pm 0.021$	LCO/Scarpa	11
3230677565443833088	3230677874682668672	4.97	$-0.076 \pm 0.057$	$-0.135 \pm 0.022$	LCO/Scarpa	11
3550081879381593728	3550084490721711872	7.87	$-0.595 \pm 0.082$	$-0.410 \pm 0.029$	LCO/Scarpa	11

<sup>a</sup>Sky-projected separation between the pair from K. El-Badry et al. (2021).

<sup>b</sup>Relative radial velocity between the pair  $v_r \equiv \text{RV}_A - \text{RV}_B$

<sup>c</sup>Two independent observations at different epochs. Only the value from obs1 will be used in this work.

<sup>d</sup>Approximate median time baseline between obs1 and obs2.

We note that the acquired values of  $v_r$ , except for those from R. Saglia et al. (2025), do not include corrections for gravitational redshifts or convective flows in stellar atmospheres. Following the recommendation of R. Saglia et al. (2025), we will quadratically add 40 m s $^{-1}$  to all nominal uncertainties of  $v_r$  when using them for modeling.

Individual Bayesian 3D modeling is carried out for each binary from the raw sample either with a fixed value of  $\Gamma$  (including the Newtonian case) or allowing it to vary within the range  $-1 < \Gamma < 1$ . These Bayesian outputs will be used in the selection of wide binaries in the low-acceleration regime and in the derivation of the value of  $\Gamma$  through statistical consolidation. Since the Bayesian outputs provide orbit solutions, we can estimate various quantities for each system, including the Newtonian gravitational acceleration defined above and the Newtonian escape velocity  $v_{\text{escN}} \equiv \sqrt{2G_N M_{\text{tot}}/r}$  where  $r$  is estimated from the Bayesian outputs.

### 3.2. Step 2: Selection of the basic-cut sample of wide binaries in the low-acceleration regime

In the second step, we select a statistical sample of wide binaries in the low-acceleration regime that have sufficiently precise  $v_r$  and are likely to be free from any kinematic contaminants based on various observational

diagnostics available at present. We first require basic selection and quality cuts of the following:

- Newtonian gravitational acceleration  $g_N < 10^{-9} \text{ m s}^{-2}$  where  $g_N$  is derived from Bayesian reconstructed orbits in generalized gravity.
- Distance of the binary system from the Sun is less than 150 pc.
- Relative RV  $v_r$  and relative 3D velocity  $v_{\text{obs}} = |\mathbf{v}_{\text{obs}}|$  have measurement errors less than 100 m s $^{-1}$ .
- Both stars have Gaia's  $\text{ruwe} < 1.25$ . (This threshold follows R. Saglia et al. (2025) but a slightly different threshold such as  $< 1.20$  or  $< 1.30$  yields consistent results.)
- Both stars are below a color-dependent luminosity cut line in the main sequence of the color-magnitude diagram as shown in Figure 4. This threshold helps remove unresolved close binaries, i.e., photometric binaries.

The above selection criteria retain only wide binaries of low internal acceleration that are relatively nearby and thus have highest data qualities. The criteria also help remove cases with potential kinematic contaminants towards the goal of selecting pure binary individuals. Only 75 systems (about 25%) of the raw sample pass the above cuts. This basic-cut sample is listed in Table 2. In the table, we provide the measured relative

<sup>3</sup> <https://gea.esac.esa.int/archive/>

	<b>Gaia DR3</b> (2014.07 – 2017.05)	<b>APOGEE-2</b> (2017.03 – 2021.01)	<b>LCO</b> (2024.12 – 2025.03)	<b>HARPS</b> (2018 – 2019)	<b>MAROON-X</b> (2024 Fall)	<b>Scarpa</b> (2013.01, 2013.12)	<b>Hipparcos</b> (late 1989 – mid 1993)
<b>Gaia DR3</b> (2014.07 – 2017.05)		3 yr	9 yr	3 yr	9 yr	2 yr	25 yr
<b>APOGEE-2</b> (2017.03 – 2021.01)	3 yr		6 yr	1 yr	6 yr	4 yr	
<b>LCO</b> (2024.12 – 2025.03)	9 yr	6 yr		6 yr	0.3 yr	11 yr	
<b>HARPS</b> (2018 – 2019)	3 yr	1 yr	6 yr		6 yr	5 yr	
<b>MAROON-X</b> (2024 Fall)	9 yr	6 yr	0.3 yr	6 yr		11 yr	
<b>Scarpa</b> (2013.01, 2013.12)	2 yr	4 yr	11 yr	5 yr	11 yr		

**Figure 3.** Summary of individual (given in parentheses at the top row and the left column) and pairwise time baselines for the various observations of radial velocities used. All given entries represent approximate median values. Hipparcos epoch is for observations of proper motions.

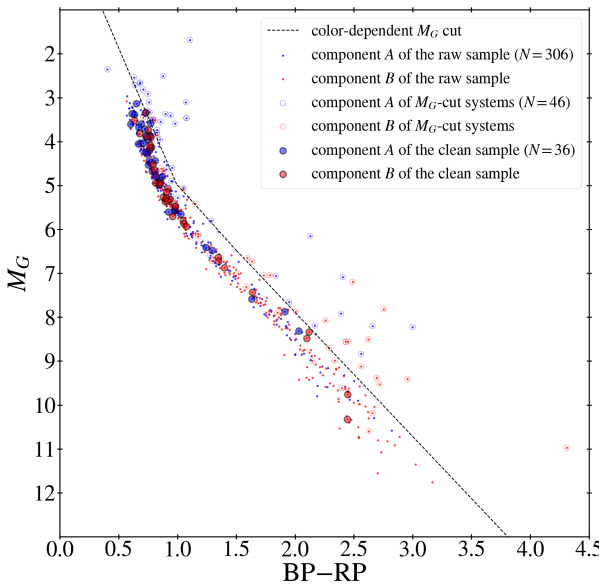


**Figure 4.** This figure shows the color-magnitude diagram of stars in the raw sample of 306 wide binaries using Gaia's BP–RP color and absolute magnitude  $M_G$  in Gaia's  $G$  band. All stars in the clean sample are fainter than the color-dependent  $M_G$  cut line.

radial velocity  $v_r$  along with its observational source. In the table, we also provide the ratio of the relative 3D velocity to the Newtonian escape velocity  $v_{\text{obs}}/v_{\text{escN}}$ , and selection merits for the final clean sample to be described below. The distribution of  $v_{\text{obs}}/v_{\text{escN}}$  for the basic-cut sample can be found in Figure 5. It shows that this sample includes cases with  $> 1$  and even with  $> 1.2$ .

**Table 2.** Measured  $v_r$  and Bayesian inferred  $v_{\text{obs}}/v_{\text{escN}}$  and  $\Gamma$  in the basic-cut sample

ID	Gaia DR3 identifier Star A/B	$d_M^a$	$v_{r,\text{DR3}}^b$	$v_r^c$	$v_{\text{obs}}/v_{\text{escN}}^d$	$\Gamma^e$	$v_r$ source	merits <sup>f</sup>
		[pc]	[km s <sup>-1</sup> ]	[km s <sup>-1</sup> ]				
1	2642922251741817216/2642922286101533952	56.01	0.503 $\pm$ 0.657	-0.156 $\pm$ 0.040	0.33 $\pm$ 0.09	-0.342 <sup>+0.255</sup> <sub>-0.162</sub>	APOGEE <sup>g</sup>	4
2	3840226230398314368/3840219358450646656	118.00	4.099 $\pm$ 3.087	-0.140 $\pm$ 0.085	0.78 $\pm$ 0.44	-0.698 <sup>+0.391</sup> <sub>-0.145</sub>	APOGEE	None
3	3861880665230888960/3858878375716469120	131.31	0.527 $\pm$ 0.327	0.386 $\pm$ 0.051	1.16 $\pm$ 0.09	0.400 <sup>+0.234</sup> <sub>-0.142</sub>	APOGEE	4
4	315289980082496000/315289980082496256	82.89	-1.707 $\pm$ 2.100	-0.869 $\pm$ 0.061	1.17 $\pm$ 0.08	0.338 <sup>+0.228</sup> <sub>-0.117</sub>	APOGEE	None
5	26273461577051716352/2627346535662838272	147.70	-0.929 $\pm$ 1.605	0.145 $\pm$ 0.057	0.53 $\pm$ 0.08	-0.025 <sup>+0.240</sup> <sub>-0.117</sub>	APOGEE	4
6	2581807955200716800/2581806619466249728	145.88	N/A	-0.011 $\pm$ 0.072	1.26 $\pm$ 0.10	0.425 <sup>+0.225</sup> <sub>-0.129</sub>	APOGEE	None
7	2594556109625136128/2594555491149842432	110.38	0.805 $\pm$ 5.848	0.128 $\pm$ 0.092	0.47 $\pm$ 0.25	-0.331 <sup>+0.312</sup> <sub>-0.260</sub>	APOGEE	None
8	783007245705158400/783007280064896128	134.55	-0.006 $\pm$ 2.106	-0.437 $\pm$ 0.051	1.26 $\pm$ 0.12	0.339 <sup>+0.232</sup> <sub>-0.121</sub>	APOGEE	None
9	1459718891236328192/1459715764500136192	137.77	-4.574 $\pm$ 3.297	-0.019 $\pm$ 0.065	0.65 $\pm$ 0.12	0.078 <sup>+0.262</sup> <sub>-0.145</sub>	APOGEE	None
10	1476646250703083264/1476646285062821888	139.05	0.142 $\pm$ 3.252	-0.172 $\pm$ 0.092	0.55 $\pm$ 0.11	-0.132 <sup>+0.263</sup> <sub>-0.086</sub>	APOGEE	None
11	1534089651581519488/1534086421765263360	120.28	-1.159 $\pm$ 2.037	-0.433 $\pm$ 0.081	1.45 $\pm$ 0.22	0.402 <sup>+0.240</sup> <sub>-0.154</sub>	APOGEE	None
12	1555391177542038400/1555388222603962752	105.41	0.204 $\pm$ 3.896	-0.119 $\pm$ 0.079	0.75 $\pm$ 0.06	0.173 <sup>+0.266</sup> <sub>-0.123</sub>	APOGEE	None
13	1580778076392231424/1580778213830765824	138.25	-1.838 $\pm$ 2.721	-0.142 $\pm$ 0.085	0.84 $\pm$ 0.13	0.062 <sup>+0.245</sup> <sub>-0.103</sub>	APOGEE	None
14	1331462302965590400/1331462302965590144	117.89	5.305 $\pm$ 2.730	0.986 $\pm$ 0.082	1.21 $\pm$ 0.09	0.355 <sup>+0.244</sup> <sub>-0.115</sub>	APOGEE	None
15	1403853152105526272/1403852430551017984	54.69	3.987 $\pm$ 2.311	0.015 $\pm$ 0.087	0.44 $\pm$ 0.10	-0.149 <sup>+0.185</sup> <sub>-0.081</sub>	APOGEE	None
16	1240752559313435520/1240752559313476224	108.20	1.124 $\pm$ 3.164	0.004 $\pm$ 0.072	0.66 $\pm$ 0.07	0.061 <sup>+0.261</sup> <sub>-0.103</sub>	APOGEE	4
17	5262754514488149632/5262754273969986688	138.99	0.309 $\pm$ 0.224	-0.049 $\pm$ 0.048	0.61 $\pm$ 0.07	0.059 <sup>+0.260</sup> <sub>-0.119</sub>	APOGEE	None
18	4757024829820200704/4757026135488693760	89.24	1.003 $\pm$ 0.526	0.633 $\pm$ 0.084	1.27 $\pm$ 0.06	0.563 <sup>+0.186</sup> <sub>-0.104</sub>	APOGEE	None
19	690460424271103360/690272545221668096	109.64	-0.074 $\pm$ 1.335	-0.126 $\pm$ 0.062	0.60 $\pm$ 0.12	0.019 <sup>+0.263</sup> <sub>-0.129</sub>	APOGEE	None
20	694284491350980864/694284628789933568	37.84	0.259 $\pm$ 0.552	-0.276 $\pm$ 0.100	0.66 $\pm$ 0.12	0.089 <sup>+0.249</sup> <sub>-0.141</sub>	APOGEE	4
21	4763619318293079168/47636189010272182400	77.02	-2.327 $\pm$ 2.076	-0.180 $\pm$ 0.075	0.51 $\pm$ 0.11	-0.085 <sup>+0.255</sup> <sub>-0.136</sub>	APOGEE	None
22	1444305829863259648/1444305937237949184	136.58	-0.282 $\pm$ 1.320	0.349 $\pm$ 0.038	0.61 $\pm$ 0.10	0.008 <sup>+0.267</sup> <sub>-0.154</sub>	APOGEE	None
23	972821779152541824/972815560039899264	113.05	-0.828 $\pm$ 1.575	-0.160 $\pm$ 0.048	0.65 $\pm$ 0.15	0.063 <sup>+0.277</sup> <sub>-0.159</sub>	APOGEE	4
24	1172915590414659328/1172920487244742912	53.42	-0.006 $\pm$ 0.360	0.043 $\pm$ 0.033	0.39 $\pm$ 0.05	-0.172 <sup>+0.234</sup> <sub>-0.113</sub>	APOGEE	1, 2, 4, 5
25	5305981470567619456/5305981745445719680	93.79	-0.132 $\pm$ 0.257	-0.337 $\pm$ 0.086	0.93 $\pm$ 0.07	0.243 <sup>+0.231</sup> <sub>-0.117</sub>	LCO	2
26	3749791158495959552/3749791055416743552	69.89	0.401 $\pm$ 0.247	0.383 $\pm$ 0.073	0.54 $\pm$ 0.11	-0.064 <sup>+0.260</sup> <sub>-0.148</sub>	LCO	2
27	1282815063829295360/1282817022334383232	55.00	-0.327 $\pm$ 0.174	-0.283 $\pm$ 0.041	0.75 $\pm$ 0.11	0.120 <sup>+0.252</sup> <sub>-0.132</sub>	LCO	1, 2, 5, 6
28	3793107930900527616/3793106419072038272	86.00	-0.748 $\pm$ 0.266	0.260 $\pm$ 0.094	0.62 $\pm$ 0.22	-0.224 <sup>+0.304</sup> <sub>-0.239</sub>	LCO	None
29	1258410612976538368/1258410750415492864	44.12	-0.192 $\pm$ 0.189	-0.632 $\pm$ 0.082	0.88 $\pm$ 0.08	0.316 <sup>+0.231</sup> <sub>-0.139</sub>	LCO	None
30	3170300942420466176/3170394607068638336	121.69	-0.750 $\pm$ 0.320	-0.055 $\pm$ 0.058	0.47 $\pm$ 0.08	-0.087 <sup>+0.256</sup> <sub>-0.120</sub>	LCO	2
31	565177595332649688/5651752515687994368	55.09	0.131 $\pm$ 0.245	-0.119 $\pm$ 0.081	0.36 $\pm$ 0.08	-0.205 <sup>+0.241</sup> <sub>-0.123</sub>	LCO	2
32	5741345125461459200/5741344919302959360	105.03	-0.631 $\pm$ 0.254	-0.327 $\pm$ 0.042	0.94 $\pm$ 0.07	0.240 <sup>+0.248</sup> <sub>-0.117</sub>	LCO	1, 2
33	3116331104937277952/3116324881524878208	73.86	-0.181 $\pm$ 0.245	-0.345 $\pm$ 0.060	1.20 $\pm$ 0.16	0.313 <sup>+0.239</sup> <sub>-0.130</sub>	LCO	2
34	3230677565443833088/3230677874682668672	63.74	-0.328 $\pm$ 0.189	-0.076 $\pm$ 0.057	0.37 $\pm$ 0.08	-0.225 <sup>+0.307</sup> <sub>-0.112</sub>	LCO	2, 5
35	5185524920830592128/5185536774940328448	38.40	0.103 $\pm$ 0.301	0.276 $\pm$ 0.086	0.52 $\pm$ 0.17	-0.164 <sup>+0.268</sup> <sub>-0.167</sub>	LCO	None
36	1967283042361454848/1967282939282261120	82.84	-0.514 $\pm$ 0.236	-0.561 $\pm$ 0.082	0.96 $\pm$ 0.11	0.226 <sup>+0.223</sup> <sub>-0.125</sub>	LCO	1
37	6570796871887419648/6570797524722448896	78.18	-0.259 $\pm$ 0.215	0.105 $\pm$ 0.069	0.33 $\pm$ 0.10	-0.299 <sup>+0.223</sup> <sub>-0.122</sub>	LCO	None
38	3158926322836178816/3158878734598549376	78.03	0.065 $\pm$ 0.606	0.023 $\pm$ 0.066	0.43 $\pm$ 0.07	-0.117 <sup>+0.230</sup> <sub>-0.111</sub>	LCO	1
39	1938247517245907456/1938247654684985216	59.47	-0.067 $\pm$ 0.187	-0.055 $\pm$ 0.046	0.88 $\pm$ 0.04	0.247 <sup>+0.224</sup> <sub>-0.124</sub>	LCO	6
40	181516553636339072/1815165883534980992	91.65	-0.075 $\pm$ 0.274	-0.853 $\pm$ 0.047	1.47 $\pm$ 0.09	0.408 <sup>+0.215</sup> <sub>-0.103</sub>	LCO	None
41	1719835231806217472/1719835407900844544	99.62	-0.192 $\pm$ 0.361	-0.297 $\pm$ 0.060	0.63 $\pm$ 0.09	0.040 <sup>+0.249</sup> <sub>-0.130</sub>	LCO	None
42	3550081879381593728/3550084490721711872	33.55	-0.692 $\pm$ 0.233	-0.595 $\pm$ 0.082	1.09 $\pm$ 0.14	0.277 <sup>+0.239</sup> <sub>-0.131</sub>	LCO	5
43	1760471948915107200/1760477618271932672	75.42	0.011 $\pm$ 0.212	0.947 $\pm$ 0.047	1.09 $\pm$ 0.06	0.338 <sup>+0.238</sup> <sub>-0.124</sub>	LCO	None
44	4763357363943383808/4763357260864168320	90.68	-0.194 $\pm$ 0.276	-0.283 $\pm$ 0.092	0.93 $\pm$ 0.06	0.206 <sup>+0.268</sup> <sub>-0.098</sub>	LCO	None
45	1003223614961194752/1003223584897948160	103.02	-0.054 $\pm$ 0.315	-0.430 $\pm$ 0.077	0.74 $\pm$ 0.09	0.123 <sup>+0.247</sup> <sub>-0.123</sub>	LCO	1
46	1142787168495168000/1142786996696476288	105.48	-0.101 $\pm$ 0.349	-0.317 $\pm$ 0.075	0.54 $\pm$ 0.10	-0.027 <sup>+0.267</sup> <sub>-0.138</sub>	LCO	None
47	5038962632187714432/5038962219872444160	115.58	0.142 $\pm$ 0.263	0.212 $\pm$ 0.088	0.40 $\pm$ 0.17	-0.352 <sup>+0.293</sup> <sub>-0.179</sub>	LCO	None
48	2932313231147240960/2932313196787509376	137.36	0.023 $\pm$ 0.231	-0.073 $\pm$ 0.085	0.49 $\pm$ 0.09	-0.056 <sup>+0.272</sup> <sub>-0.120</sub>	LCO	None
49	3487243037508315648/3487237024554098560	79.73	0.037 $\pm$ 0.214	0.170 $\pm$ 0.060	0.52 $\pm$ 0.11	-0.085 <sup>+0.248</sup> <sub>-0.137</sub>	LCO	None
50	4599984642025088128/4599984504586131456	69.75	-0.215 $\pm$ 0.269	0.086 $\pm$ 0.062	0.51 $\pm$ 0.09	-0.023 <sup>+0.253</sup> <sub>-0.128</sub>	LCO	1
51	4430185068482324864/4430185034123000960	100.24	-0.108 $\pm$ 0.276	-0.025 $\pm$ 0.072	0.48 $\pm$ 0.10	-0.100 <sup>+0.268</sup> <sub>-0.106</sub>	LCO	1

**Table 2** continued

Table 2 (continued)

52	5899243585161684864/5899244375435693952	80.48	$-0.904 \pm 0.217$	$-0.566 \pm 0.056$	$0.85 \pm 0.09$	$0.191^{+0.258}_{-0.133}$	LCO	None
53	2776055105362407680/2776054899203977728	108.61	$-0.596 \pm 0.286$	$-0.468 \pm 0.017$	$0.93 \pm 0.06$	$0.314^{+0.254}_{-0.154}$	HARPS	3, 5
54	4940794866807373952/4940794488850252928	116.26	$0.354 \pm 0.215$	$0.449 \pm 0.004$	$0.90 \pm 0.02$	$0.222^{+0.233}_{-0.108}$	HARPS	2, 3, 5
55	4722135642226902656/4722111590409480064	12.04	$-0.505 \pm 0.177$	$-0.464 \pm 0.028$	$0.70 \pm 0.04$	$0.079^{+0.254}_{-0.108}$	HARPS	3
56	5060104351007433472/5060105897197110144	35.90	$-0.421 \pm 0.169$	$-0.254 \pm 0.035$	$0.65 \pm 0.12$	$0.031^{+0.247}_{-0.146}$	HARPS	3, 5
57	4666907551119833984/4666907516760096512	55.00	$-0.319 \pm 0.179$	$-0.197 \pm 0.013$	$0.45 \pm 0.08$	$-0.139^{+0.272}_{-0.130}$	HARPS	3
58	5607190344506642432/5607189485513198208	38.08	$-0.284 \pm 0.188$	$-0.080 \pm 0.003$	$0.35 \pm 0.04$	$-0.299^{+0.254}_{-0.162}$	HARPS	3, 5
59	4235732073427592704/4235731867269159680	100.27	$-1.092 \pm 0.239$	$-0.861 \pm 0.015$	$1.12 \pm 0.03$	$0.339^{+0.246}_{-0.113}$	HARPS	3
60	6458951765971500672/6458952345790198144	44.30	$-0.344 \pm 0.175$	$0.064 \pm 0.012$	$0.45 \pm 0.12$	$-0.125^{+0.255}_{-0.133}$	HARPS	3
61	2201661297490051968/2201661091331626752	107.50	$-0.347 \pm 0.367$	$-0.018 \pm 0.006$	$0.62 \pm 0.07$	$0.056^{+0.244}_{-0.116}$	MAROON-X	5
62	1871558941576158464/1871559697490418816	92.44	$0.426 \pm 0.438$	$-0.024 \pm 0.009$	$0.35 \pm 0.07$	$-0.243^{+0.223}_{-0.114}$	MAROON-X	1
63	1942384773344557184/1942384872124424832	52.00	$0.648 \pm 0.312$	$0.266 \pm 0.084$	$0.66 \pm 0.15$	$-0.114^{+0.056}_{-0.050}$	MAROON-X	None
64	1762461893163118464/1762461309047562368	121.93	$0.535 \pm 0.347$	$0.220 \pm 0.004$	$0.55 \pm 0.05$	$0.012^{+0.262}_{-0.127}$	MAROON-X	None
65	4230699363889120128/4230699329529382400	79.48	$0.018 \pm 0.540$	$-0.278 \pm 0.022$	$0.79 \pm 0.07$	$0.055^{+0.244}_{-0.102}$	MAROON-X	1
66	3400292798990117888/3394298532176344960	14.54	$-0.332 \pm 0.186$	$-0.253 \pm 0.052$	$0.61 \pm 0.11$	$-0.044^{+0.265}_{-0.171}$	Scarpa	6
67	3975129194660883328/3975223065466473216	39.41	$0.164 \pm 0.242$	$0.141 \pm 0.021$	$0.25 \pm 0.06$	$-0.361^{+0.251}_{-0.130}$	Scarpa	None
68	6193279279612173952/6193280031230266752	29.90	$-1.280 \pm 0.193$	$-1.014 \pm 0.025$	$1.67 \pm 0.06$	$0.519^{+0.187}_{-0.103}$	Scarpa	None
69	1440518669436791296/1440425863783337856	45.59	$-0.494 \pm 0.183$	$-0.442 \pm 0.034$	$0.78 \pm 0.07$	$0.120^{+0.247}_{-0.116}$	Scarpa	6
70	10584899657116672/10608573516849536	47.06	$-0.676 \pm 0.195$	$-0.856 \pm 0.027$	$1.27 \pm 0.04$	$0.399^{+0.213}_{-0.105}$	Scarpa	None
71	3359808231100381312/3359820016490648576	47.63	$0.995 \pm 0.208$	$0.791 \pm 0.017$	$1.11 \pm 0.01$	$0.711^{+0.131}_{-0.116}$	Scarpa	None
72	692119656035933568/692120029700390912	48.74	$-0.404 \pm 0.189$	$-0.292 \pm 0.015$	$0.69 \pm 0.09$	$0.233^{+0.320}_{-0.209}$	Scarpa	None
73	1019361632454363904/1019174509319377536	29.18	$-1.115 \pm 0.181$	$-1.337 \pm 0.016$	$1.52 \pm 0.03$	$0.558^{+0.175}_{-0.100}$	Scarpa	None
74	777967084390189696/777967702865481344	45.87	$1.273 \pm 0.201$	$1.353 \pm 0.015$	$1.39 \pm 0.02$	$0.586^{+0.175}_{-0.095}$	Scarpa	None
75	2882262637207289216/2882262529831237120	40.92	$0.668 \pm 0.181$	$0.747 \pm 0.021$	$0.92 \pm 0.03$	$0.218^{+0.223}_{-0.105}$	Scarpa	6

<sup>a</sup> Error-weighted mean of the measured distances of Stars A & B.

<sup>b</sup>  $\text{RV}_A - \text{RV}_B$  from Gaia DR3

<sup>c</sup>  $\text{RV}_A - \text{RV}_B$  from other sources

<sup>d</sup> The scalar 3D relative velocity over the Newtonian escape velocity

<sup>e</sup> Bayesian-inferred value of  $\Gamma$  (Equation (1)). The quoted uncertainties are from one half of the 95% width.

<sup>f</sup> Selection merits (those marked with ‘None’ will not be included for gravity inference: see the text for the details): (1) Non-detection of additional faint stars from the Speckle observations of the fields around both stars; (2) LCO RVs at two (or three) epochs are consistent within  $2\sigma$ ; (3) HARPS RVs from R. Saglia et al. (2025); (4) APOGEE RVs with  $\text{VSCATT} < 0.1 \text{ km s}^{-1}$ ; (5) Two independent values are available from two different sources/telescopes (see Table 1) and consistent with each other; (6) Precise Gaia DR3 values (with error  $< 0.19 \text{ km s}^{-1}$ ) are available and agree within  $< 0.1 \text{ km s}^{-1}$  with the given values.

<sup>g</sup> Here APOGEE refers to either APOGEE-1 or APOGEE-2(N or S). Note that most RVs used happen to come from APOGEE-2.

Although the basic cut is already strict to the point that many true pure binaries may have been excluded, the sample may still include contaminated or unreliable cases as Figure 5 indicates. For example, a star with a faint close companion can still have  $\text{ruwe} < 1.25$ . In addition, even for a true pure binary, a reported value of  $v_r$  with a small measurement error generally requires independent confirmation due to any possibilities of unknown systematic errors.

### 3.3. Step 3: Selection of the clean sample of wide binaries in the low-acceleration regime

The driving philosophy of our sample selection is to maximally control systematic uncertainties even if statistical power is significantly sacrificed. Therefore, we require that each binary satisfy at least one of the fol-

lowing additional criteria to remove potentially contaminated or unreliable systems:

- (1) Speckle interferometric observations of the fields around both stars were carried out and no objects were detected. In addition, the measured value of  $v_r$  (whatever its source is) is consistent with the Gaia DR3 value within  $2\sigma$ .
- (2) Both stars were observed at two epochs with the LCO and two independent values of  $v_r$  are consistent with each other within  $2\sigma$ .
- (3)  $v_r$  values come from the HARPS RVs of the R. Saglia et al. (2025) sample.
- (4)  $v_r$  values come from APOGEE, and value(s) of VSCATTER (scatter from multiple visits in an obser-

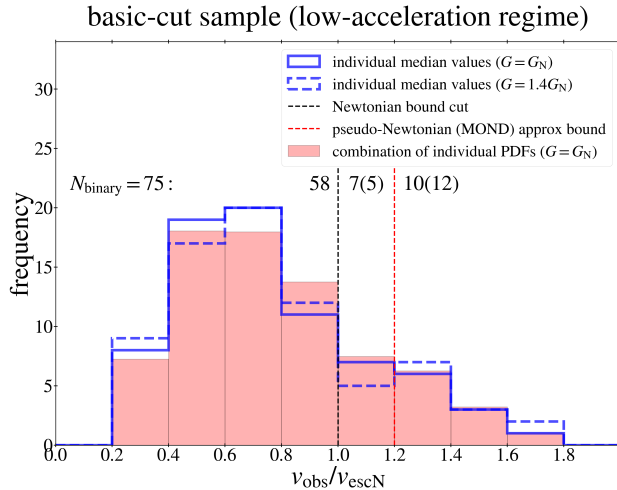


**Figure 5.** The distribution of  $v_{\text{obs}}/v_{\text{escN}}$  is shown for the basic-cut sample of 75 wide binaries that may include kinematically contaminated cases. Here  $v_{\text{obs}}$  is the magnitude of the observed relative 3D velocity between the pair while  $v_{\text{escN}}$  is the Newtonian escape velocity predicted by 3D elliptical orbit modeling with a fixed value of  $G = G_N(\Gamma = 0)$  or  $1.4G_N(\Gamma \approx 0.07)$ , which encompass the current range of the effective gravitational constant for Newtonian and MOND models. Both the distribution of the individual median values and that of random values from the Bayesian MCMC samples are shown. The numbers indicated are from the median distributions. Pseudo-Newtonian (MOND) approximate bound of 1.2 is based on numerical MOND solutions (K.-H. Chae & M. Milgrom 2022) in the regime with acceleration  $< a_0$  for a test particle assuming one-particle equivalent description.

vation) is(are) available and its (maximum) value is less than  $100 \text{ m s}^{-1}$ .

- (5) Two independent values of  $v_r$  are available from two different sources/telescopes and are consistent with each other (see Table 1).
- (6) Unusually precise Gaia DR3 values (with error  $< 190 \text{ m s}^{-1}$ ) are available and agree within  $100 \text{ m s}^{-1}$  with the values from other sources.

Some systems satisfy multiple selection merits. In Table 2, we indicate the selection merit(s) for each binary.

We note that the targets of Speckle observations were selected from the samples recently defined and used by two of us (e.g. X. Hernandez et al. 2024b; K.-H. Chae 2024a). These samples were selected with a number of indirect criteria to exclude apparent binaries hosting unresolved close companion star(s). The Speckle observations (Appendix E) show that only 5% of the target systems potentially have additional faint star(s), confirming that the employed criteria were efficient in selecting

samples of pure binaries in a *statistical* sense. By comparison, in random samples of local stars of comparable mass, Speckle studies generally identify about 40% unresolved binaries.

Only 37 systems satisfy at least one of the requirements listed above. We manually check all objects found in the 3D space around each binary using the Gaia DR3 archive, and find that in one pair (Gaia DR3 1762461893163118464 & 1762461309047562368) there is a third star that may perturb the system. So we exclude this system and are left with 36 systems, which will define our clean sample that also passes additional tests as will be shown in the following two subsections. Aside from the membership inclusion criteria mentioned above, no system having Speckle observations identifying any extra component (some of which might just be background sources) was included in the final clean sample. The properties of the clean sample will be described in Section 3.4.

### 3.3.1. Additional check: Testing Gaia-Hipparcos proper motion consistency over 25 years

We check whether the Gaia DR3 proper motions (PMs) of the stars in the clean sample are consistent with the Hipparcos PMs measured about 25 years earlier than Gaia. Although the Hipparcos precision is poorer by an order-of-magnitude and not all binaries in the Gaia DR3 were observed by Hipparcos, the comparison between the two can provide an additional test. We only consider the relative PM between the pair for this test because it is free from issues of absolute calibrations between the two observations (T. D. Brandt 2018) and what is relevant for internal dynamics is the relative velocity. We find that 41 binaries from the raw sample (including 13 that satisfy the above selection merits) have the Hipparcos PMs for both stars.

Figure 6 shows the comparison between the two observations in terms of the sky-projected relative velocity components  $v_{x'}$  and  $v_{y'}$  derived from the PMs for 41 systems from the raw sample including 13 systems belonging to the clean sample. First of all, all 13 systems from the clean sample satisfy the Gaia-Hipparcos consistency at least within  $3\sigma$ , while there are cases that do not satisfy such a consistency.

Three binaries show  $> 5\sigma$  discrepancy between Gaia DR3 and Hipparcos, strongly indicating that these binaries have been undergoing kinematic perturbations during the time baseline of  $\approx 25$  years (see Figure 3) between the two observations. If this is true, the Bayesian modeling results for these systems are very likely to display abnormal properties in the posterior PDFs of the parameters beyond the ranges predicted by any viable gravity models including Newton and MOND. Indeed, we find that the posterior PDFs for the systems return abnormally large values of  $\Gamma > 0.5$  and  $v_{\text{obs}}/v_{\text{escN}} > 1.3$ . Interestingly, all these systems are from the Scarpa sample (Gaia DR3 777967084390189696 &

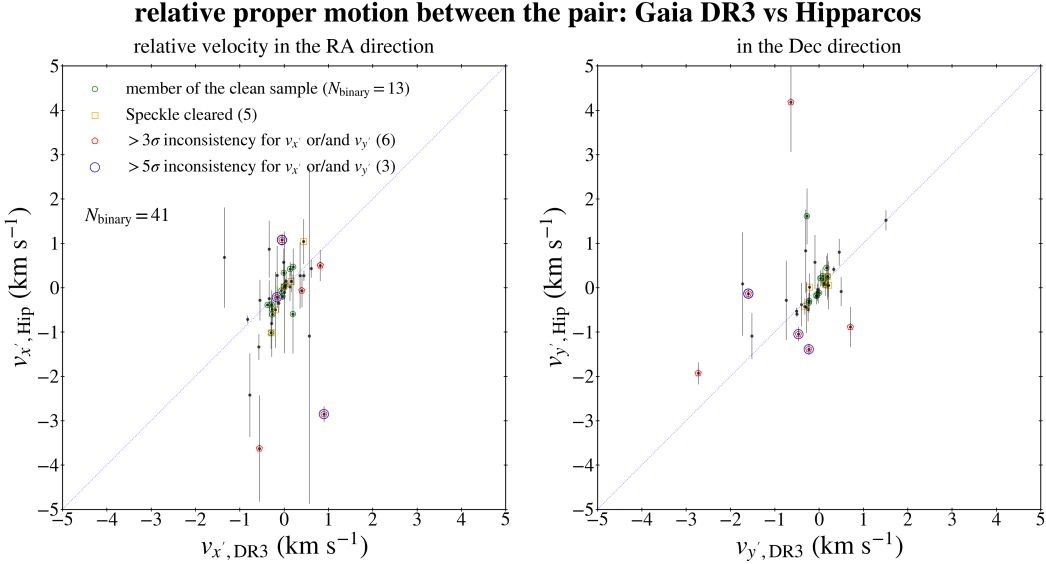


**Figure 6.** This figure compares sky-projected transverse velocities derived from the relative proper motions (PMs) between the pair reported in Gaia DR3 and Hipparcos for 41 wide binaries selected from the raw sample. The three systems with the  $> 5\sigma$  discrepancies between the two observations show abnormal properties in the posterior PDFs of the parameters from Bayesian modeling (see the text).

777967702865481344, Gaia DR3 6193279279612173952 & 6193280031230266752, and Gaia DR3 1754191435419155456 & 1754191229260708736: the former two are included in the basic-cut sample of Table 2 while the latter is not), and none of them satisfy any of the selection merits for the clean sample and were therefore excluded. We note also that two of these systems fail the velocity threshold introduced by K.-H. Chae (2024a) (see Appendix C).

While the  $> 5\sigma$  discrepancy between Gaia DR3 and Hipparcos PMs appears to be a decisive indicator of kinematic contaminants, the interpretation of the less strong discrepancy  $> 3\sigma$  (but not  $> 5\sigma$ ) is unclear. Three systems exhibit such discrepancies but no abnormalities in the PDF of  $\Gamma$  or the inferred value of  $v_{\text{obs}}/v_{\text{escN}}$ . This may indicate that a  $3\sigma$ -threshold in the Gaia-Hipparcos comparison is not effective or reliable. However, the detail on the threshold appears to be irrelevant for the present clean sample because none of the 13 systems from the clean sample show a  $> 3\sigma$  discrepancy.

The remarkable agreement between the Gaia-Hipparcos  $> 5\sigma$  discrepancy and the Bayesian-inferred large value of  $v_{\text{obs}}/v_{\text{escN}} \gtrsim 1.3$  in identifying kinematically contaminated systems suggests that the PDF of  $\Gamma$  (as was already discussed in K.-H. Chae (2025a)) or the quantity  $v_{\text{obs}}/v_{\text{escN}}$  may be used when the direct observational test such as the Gaia-Hipparcos PM test is not available. As will be shown below, all systems from the clean sample have  $v_{\text{obs}}/v_{\text{escN}} \lesssim 1.2$  in concordance with the Gaia-Hipparcos test results.

### 3.3.2. Additional check: Comparing metallicities of the two components

While the formation and long-term survival mechanisms of gravitationally-bound wide binaries are not well understood, wide binary stars are thought to be formed in a common interstellar gas cloud, through mechanisms such as dissolution of star clusters (e.g., M. B. N. Kouwenhoven et al. 2010; N. Moeckel & C. J. Clarke 2011, dynamical unfolding of triples (B. Reipurth & S. Mikkola 2012)), formation from adjacent cores (A. Tokovinin 2017), gravitational capture (M. Rozner & H. B. Perets 2023)), and star formation in the turbulent interstellar medium (S. Xu et al. 2023). If the two main-sequence stars of a wide binary are born together from a common cloud, they will have identical or similar chemical compositions regardless of their ages or formation mechanisms. Observational studies generally find that metallicities of the two stars match well (e.g., J. J. Andrews et al. 2019; K. Hawkins et al. 2020; T. Nelson et al. 2021; D. Lim et al. 2024).

Thus, we seek to check whether our wide binaries satisfy the expected consistency of metallicities between the two components. In general, high-SNR and high-resolution spectra are needed to measure metallicities of stars, but we collect metallicities from the public databases/publications for as many stars of our sample as possible. Figure 7 shows the metallicities collected from APOGEE,<sup>4</sup> HARPS (R. Saglia et al. 2025),

<sup>4</sup> <https://www.sdss4.org/dr17/irspect/abundances/>

## metallicities for wide binaries

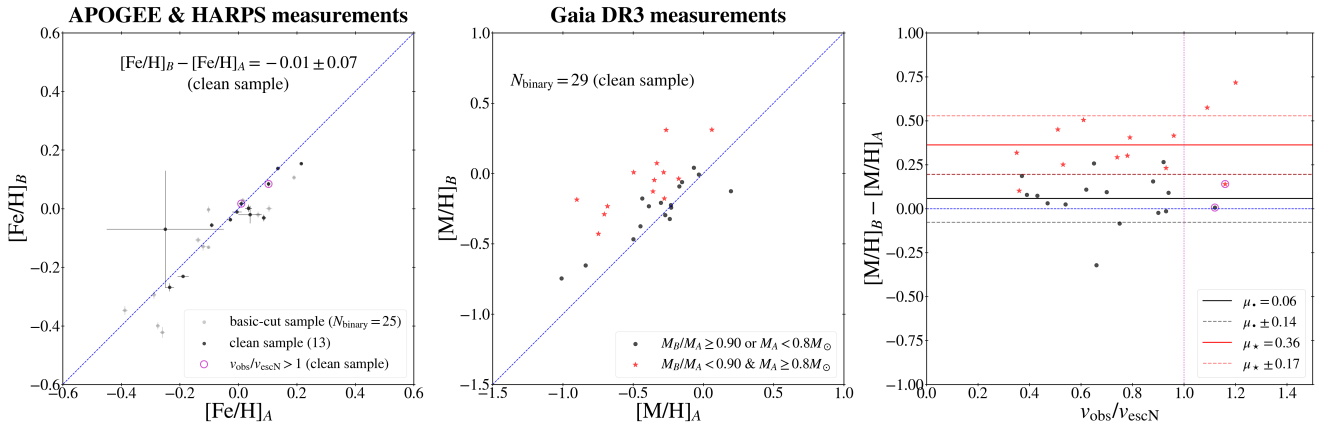


**Figure 7.** The left panel shows APOGEE and HARPS measurements of iron abundances  $[\text{Fe}/\text{H}]$  for the stars of 25 wide binaries from the basic-cut sample including 13 from the clean sample. The brighter ( $A$ ) and the fainter ( $B$ ) components of binaries show a negligible difference:  $[\text{Fe}/\text{H}]_B - [\text{Fe}/\text{H}]_A = -0.01 \pm 0.07$ . Two systems (marked by encircled points) gravitationally unbound by Newtonian gravity ( $v_{\text{obs}} > v_{\text{escN}}$ ) also have nearly equal values of  $[\text{Fe}/\text{H}]$  for the two components. The middle panel shows Gaia DR3 metallicities  $[\text{M}/\text{H}]$  (R. Andrae et al. 2023) for 29 wide binaries from the clean sample. There is a good correlation between the two components of the binaries. The right panel shows the systematic difference between the two components. The systematic difference is largely due to the binaries marked by red five-pointed stars in which component A is brighter (more massive) than component B, which is consistent with the known systematic for Gaia’s  $[\text{M}/\text{H}]$  (R. Andrae et al. 2023). See the text for the details.

and Gaia DR3 (R. Andrae et al. 2023). The former two provide accurate and precise results based on high-resolution spectra while the latter provides much less precise results.

The left panel of Figure 7 compares APOGEE or HARPS iron abundances  $[\text{Fe}/\text{H}]$  of the the brighter ( $A$ ) and the fainter ( $B$ ) components of 25 (17 APOGEE + 8 HARPS) wide binaries selected from the basic-cut sample that include 13 wide binaries of the clean sample. The metallicity difference  $[\text{Fe}/\text{H}]_B - [\text{Fe}/\text{H}]_A$  is consistent with zero with an rms scatter  $< 0.1$ . In particular, the 13 wide binaries of the clean sample have  $[\text{Fe}/\text{H}]_B - [\text{Fe}/\text{H}]_A = -0.01 \pm 0.07$ . Moreover, the two systems with  $v_{\text{obs}}/v_{\text{escN}} > 1$  from the clean sample satisfy well the expected property  $[\text{Fe}/\text{H}]_B \simeq [\text{Fe}/\text{H}]_A$  of true binaries.

The middle panel of Figure 7 shows Gaia DR3 metallicities  $[\text{M}/\text{H}]$  (where M represents all metal elements) for the 29 wide binaries of the clean sample for which this quantity is available for both components. The two metallicities  $[\text{M}/\text{H}]_A$  and  $[\text{M}/\text{H}]_B$  are well correlated, but there is a clear systematic shift for those with relatively large mass difference ( $M_B/M_A < 0.9$ ) between the two components while there is no tangible shift for those with similar masses or those having relatively small masses regardless of mass ratio. The selective systematic difference is well consistent with the known systematic of the Gaia DR3 general stellar parameterizer for photometric (GSP-Phot)  $[\text{M}/\text{H}]$  as a function of effective temperature  $T_{\text{eff}}$ . Figure 11 of R. Andrae et al.

(2023) shows that  $[\text{M}/\text{H}]$  for stars with  $T_{\text{eff}} \lesssim 4500\text{K}$  have no systematic shift while  $[\text{M}/\text{H}]$  has a systematic shift  $\approx -0.4 - -0.3$  dex for  $T_{\text{eff}} > 4600\text{K}$ , which corresponds to  $M \approx 0.8M_{\odot}$  (Figure 7 of Z. Eker et al. (2015)). Moreover, the same figure shows that the scatter around the median systematic shift is large  $\gtrsim 0.3$  dex. Thus, the measured statistic of  $[\text{M}/\text{H}]_B - [\text{M}/\text{H}]_A = 0.36 \pm 0.17$  dex (i.e., the more massive star has a lower value) is well consistent with random fluctuations.

The above results demonstrate that all available metallicities for our clean sample of wide binaries are consistent with the current understanding of wide binary stars that the two components have identical or similar metallicities.

### 3.4. Properties of the clean sample

The clean sample was defined with various selection merits, and additional checks (Sections 3.3.1 and 3.3.2) using the comparison of Gaia and Hipparcos relative PMs and the comparison of metallicities of the two components have not found any noticeable issue in the clean sample. Thus, all 36 wide binaries from the clean sample will be used to infer gravity. Here we describe key statistical properties of the clean sample.

The distribution of  $v_{\text{obs}}/v_{\text{escN}}$  for the clean sample can be found in Figure 8. Compared with Figure 5, all the systems with  $v_{\text{obs}}/v_{\text{escN}} > 1.2$  (or 1.22 for  $G = 1.4G_{\text{N}}$ ) and three (or one) systems with  $1 < v_{\text{obs}}/v_{\text{escN}} \leq 1.2$  are removed, but four systems with  $1 < v_{\text{obs}}/v_{\text{escN}} \lesssim 1.2$  remain. It is interesting to note that although the

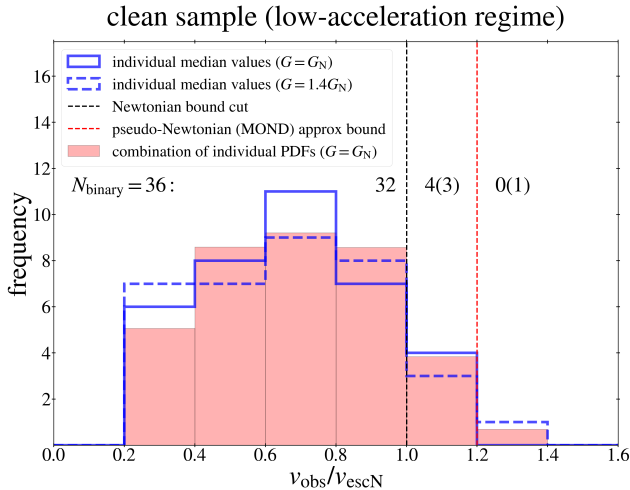


**Figure 8.** Same as Figure 5 but for the clean sample. There are no cases with  $v_{\text{obs}}/v_{\text{escN}} > 1.22$  for this sample.

quality cuts introduced in going from Figure 5 to Figure 8 do not include the  $v_{\text{obs}}/v_{\text{escN}}$  ratio in any way, the above requirements for the stability and reliability of radial velocities naturally remove all cases with  $v_{\text{obs}}/v_{\text{escN}} > 1.22$ .

Figure 9 shows the distribution of the magnitude of three relative velocity components for the clean sample. For a randomly selected sample, the three components are expected to be statistically equivalent if they are measured with comparable precision. Indeed, the three components are consistent with one another, in terms of both the overall shape and the median value.

In Figure 10, we compare various independently measured values of  $v_r$ . Because the major criterion used to define the clean sample is the availability of multiple values of  $v_r$  measured at multiple (mostly two) epochs (although the time difference between epochs is quite diverse: see Figure 3), it is interesting to check/test how well independent values match each other. The left panel of Figure 10 compares the values ( $v_r$ ) of the clean sample listed in Table 2 with the Gaia DR3 values ( $v_{r,\text{DR3}}$ ) that happen to be available for all the binaries of the sample. They are consistent with each other up to their measurement errors. The difference  $v_{r,\text{DR3}} - v_r$  has a mean of  $-0.034 \text{ km s}^{-1}$  and an rms scatter of  $0.385 \text{ km s}^{-1}$ . We find that  $v_{r,\text{DR3}}$  has a much larger rms scatter of  $0.475 \text{ km s}^{-1}$  (due to the larger measurement errors) compared with  $0.312 \text{ km s}^{-1}$  for  $v_r$ . The latter is close to the intrinsic scatter. For the subsample with relative precise  $v_{r,\text{DR3}}$  (with error  $< 0.3 \text{ km s}^{-1}$ ),  $v_{r,\text{DR3}}$  has a much smaller scatter of  $0.377 \text{ km s}^{-1}$  which is similar to  $v_r$ 's scatter of  $0.354 \text{ km s}^{-1}$  for the same binaries. For this subsample, there is an excellent match between  $v_r$  and  $v_{r,\text{DR3}}$  that were observed at different epochs separated by 2 - 9 years (Figure 3).

The middle panel of Figure 10 compares two independent values measured by the LCO at two epochs separated by a few months (see Appendix A.1). In 14 of the 18 systems, two values agree well within  $2\sigma$ . For the rest, one system agrees within  $3\sigma$ , but the other systems are discrepant by  $> 3\sigma$ . All such cases were excluded from the clean sample. In one system (Stars HD 101574 and BD-01 2557, Table 4) there is a large discrepancy between two measurements of  $v_r$  with different telescopes (within the LCO) due to the discrepant RV values for HD 101574 (see Appendix A.1). It is unclear whether this kind of discrepancy is due to intrinsic variations from kinematic perturbations or issues in measurements. Whatever the case, this possibility of large measurement-to-measurement variation highlights the importance of reproduction and confirmation of  $v_r$  values.

In the right panel of Figure 10, black dots compare two independent values of  $v_r$  measured with different telescopes at two epochs separated by 3 - 11 years (except for one system which has a 0.3 year baseline) for 9 wide binaries satisfying the selection merit #(5). The values  $v_{r,\text{obs1}}$  and  $v_{r,\text{obs2}}$ , star identifiers, and observation sources of the 9 systems can be found in Table 1 and Table 2. They match well each other within a few times the small nominal errors except for one system, which is not discarded as already mentioned in Section 3.1. We note that nominal measurement errors for some systems shown in the panel are extremely small ( $< 10 \text{ m s}^{-1}$ ), but realistic errors considering the effects of gravitational redshift and convective flow may be at least a few tens of  $\text{m s}^{-1}$  (R. Saglia et al. 2025). Magenta circles shown in the left panel are reproduced here to show all possible multi-epoch measurements that are reasonably precise. Because seven systems from the subsample represented by magenta circles are also included in the list of Table 1, there are only 25 systems with multi-epoch values. For 21 of them, time baselines are in the range of 3 - 11 years (see Figure 3).

Regarding masses of the stars to be used as the observational input, individual estimates are available for wide binaries from the R. Saglia et al. (2025) sample and the LCO sample (Appendix A). For wide binaries for which individual estimates are not available from stellar modeling, we use the mass-magnitude relation derived by K.-H. Chae (2023) to estimate the mass of a star. As explicitly shown in K.-H. Chae (2025a) and Y. Yoon et al. (2025), the K.-H. Chae (2023) masses agree well with the Gaia DR3 FLAME masses for stars similar to those used in this work whenever the latter are available from the Gaia archive (note that not for all stars FLAME masses are available). Figure 11 shows the distribution of our masses and a comparison with the corresponding FLAME masses for those stars that have the FLAME masses. We note that our masses are statistically consistent with the FLAME masses with an rms scatter of 5% and our Bayesian methodology al-

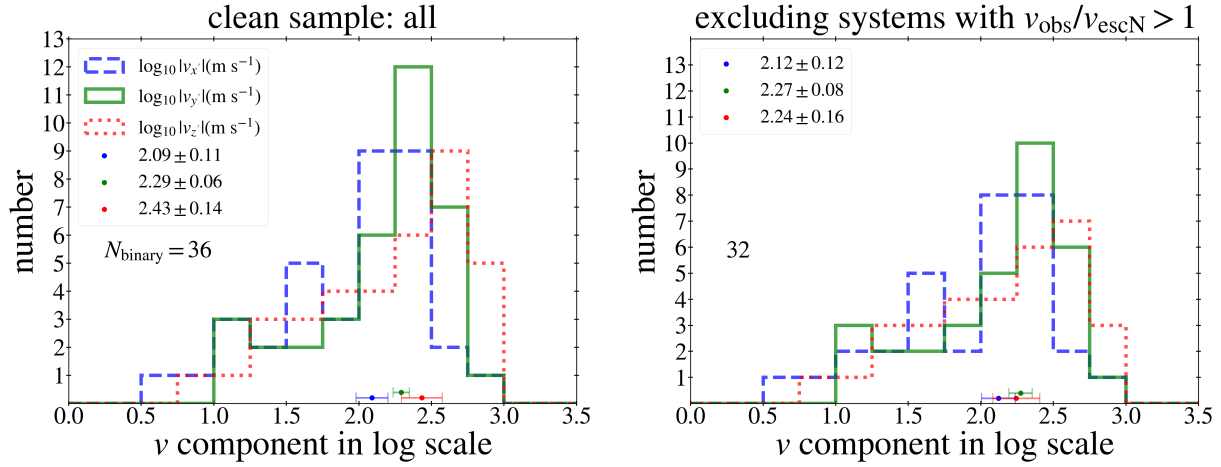


**Figure 9.** The distribution of the magnitude of relative velocity component is shown for the clean sample of wide binaries. The left panel shows the distribution for all wide binaries while the right panel shows the distribution excluding four systems that are not gravitationally bound by Newtonian gravity. In both panels, all three components are statistically consistent with one another, dots with error bars giving the mean velocity values for the 3 velocity components and their confidence intervals.

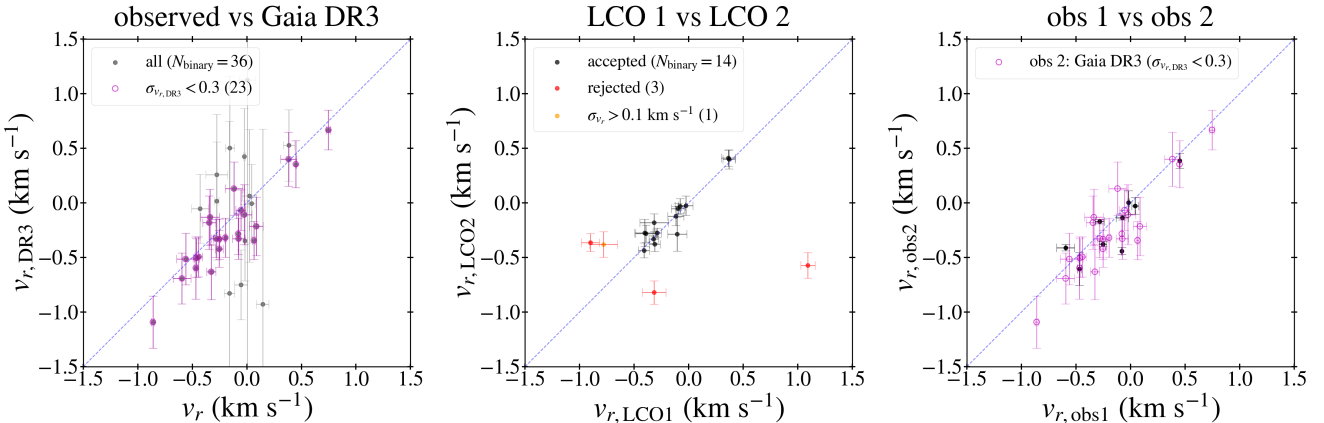


**Figure 10.** The relative radial velocity ( $v_r$ ) measurements from different observations are compared for the wide binaries of the clean sample. The left panel compares the values collected in this work with the values from the Gaia DR3 database. Relatively precise DR3 values represented with magenta color match excellently with  $v_r$ . The middle panel compares two independent measurements within the LCO network as described in Appendix A.1. Those with  $> 2\sigma$  discrepancy (marked by red dots) are precluded in this work. The right panel compares two independent measurements from different observations/sources separated by more than several years. Black dots are from Table 1 and magenta circles are from the left panel. Seven systems are represented by both black dots and magenta circles, meaning that this panel includes only 25 unique systems (see the text for the details).

lows for the uncertainty of mass through the parameter  $\log_{10} f_M$ .

#### 4. RESULTS ALONG WITH RELEVANT DISCUSSIONS

We now present our inference of gravity at low acceleration ( $< 10^{-9} \text{ m s}^{-2}$ ) through the parameter  $\Gamma$  (Equation (1)) by applying the Bayesian methodology (Section 2) to the clean sample of wide binaries described in 3. First of all, we note that the measured 3D ve-

locity components suffer from minor geometric effects known as perspective effects (E. J. Shaya & R. P. Olling 2011; Y. Yoon et al. 2025), and thus we actually use velocities corrected from those described in Section 3 for perspective effects. The data file including the corrected velocities will be available on Zenodo. While the priors on inclination ( $i$ ) and orbit true anomaly ( $\Delta\phi$ ) described in Section 2 are fixed because they are statistical properties that a random sample of orbits must satisfy, we consider a wide range of possibilities on the

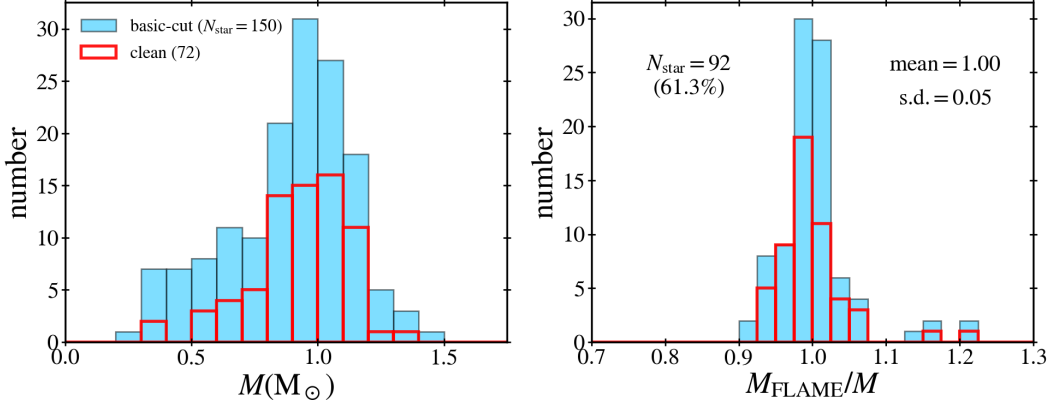


**Figure 11.** The left panel shows the distribution of masses of the stars to be used in this work. The right panel compares the Gaia DR3 FLAME masses with our masses for those stars whose FLAME masses are available. The two masses agree well with a scatter of only 5%.

prior probability distribution on eccentricity ( $e$ ):  $\alpha = 0$  (flat),  $\alpha = 1$  (thermal), and  $\alpha = 1.3$  (superthermal for Gaia DR3 wide binaries of relevance: H.-C. Hwang et al. 2022) in  $f_{\text{pr}}(e) = (1 + \alpha)e^\alpha$ . Our nominal choice will be the thermal distribution and it is implicitly assumed if not stated otherwise.

In Figure 12, we first examine the individual PDFs of  $\Gamma$  for all 75 wide binaries with precise  $v_r$  (uncertainty  $< 100 \text{ m s}^{-1}$ ) of the basic-cut sample listed in Table 2. This sample includes both the clean sample and the rest. Since the systems not included in the clean sample cannot be verified to be uncontaminated on the basis of the currently available observational information, this figure may include kinematically contaminated cases, although it probably contains mostly pure binaries. Indeed, there are clear outliers with the PDFs of  $\Gamma$  covering only the range  $\Gamma > 0.2$ . These abnormal PDFs do not overlap with one narrow PDF peaked at a negative value. In other words, the former and the latter are mutually exclusive, meaning that they cannot obey the same gravity law if their 3D velocities are not contaminated. For this reason, this basic-cut sample is not used to derive a consolidated value of  $\Gamma$ . However, it will be interesting to investigate those wide binaries with abnormal PDFs in the future, as one such individual system alone, if it is a pure binary with accurate data, can rule out certain gravity models.

#### 4.1. Main results

The top left panel of Figure 13 shows the PDFs of  $\Gamma$  for the clean sample of 36 wide binaries. In contrast to Figure 12, all individual PDFs behave well and overlap well with one another without exception. This is expected if all wide binaries obey the same gravity law and all velocities are uncontaminated and reliably measured. In other words, individual PDFs will represent only random scatters around the underlying gravity law. The properties of the individual PDFs are reassuring of the reliability of all the data involved and the process of

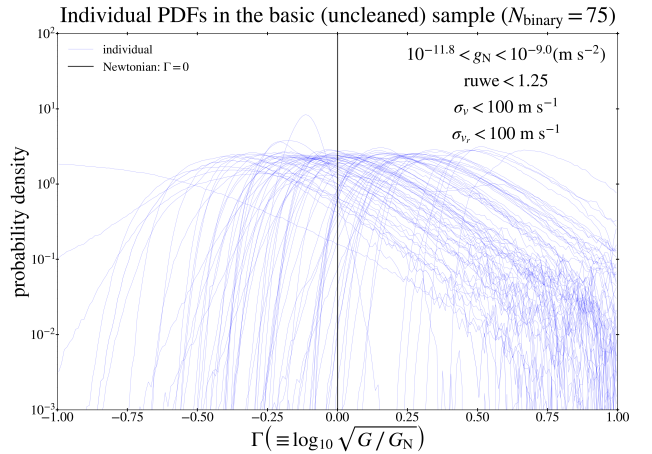


**Figure 12.** This figure shows the individual PDFs of  $\Gamma$  for the entire sample of Table 2. Most PDFs overlap one another reasonably well. However, there are several individual cases peaked at large positive values of  $\Gamma$  that does not overlap with one narrowly peaked at a negative value. It turns out that none of these mutually excluding systems are included in the clean sample.

selecting the clean sample. Then, the underlying gravity (parameterized by  $\Gamma$  in the present study) may be recovered by the statistical consolidation described in Section 2.2 of K.-H. Chae (2025a) based on T. P. Hill & J. Miller (2011).

The top left panel of Figure 13 shows the statistical consolidation for all wide binaries of the clean sample, while the other panels show various subsamples. The subsamples are considered to test how an increased precision of velocities or/and a designed control of unusually higher velocities (within the clean sample) can affect the inference of gravity. The consolidated PDF for the entire clean sample is well outside the Newtonian value

$\Gamma = 0$ , in stark contrast with the samples with stronger internal acceleration ( $> 10^{-9} \text{ m s}^{-2}$ ) presented in K.-H. Chae (2025a,b). As can be seen from the curve displayed on the logarithmic scale, the consolidated PDF is approximately Gaussian but not quite exactly. There is a mild left-right asymmetry, and the curve does not decline exactly like Gaussian. We find  $\Gamma = 0.102^{+0.023}_{-0.021}$ , a  $60^{+17}_{-15}\%$  boost to Newtonian gravity, where the quoted formal uncertainties represent the halves of the 95.4% bounds (rather than the 68.3% bounds) from the central median. Based on the Gaussian-like formal uncertainties or the actual PDF, Newton is ruled out at  $\gtrsim 5\sigma$ . In contrast, the predicted range of MOND gravity models is consistent with the consolidated PDF within  $2\sigma$ .

In the bottom left panel of Figure 13, we consider a subsample with highest-precision  $v_r (= v_z')$  with uncertainties  $< 50 \text{ m s}^{-1}$ , to be fully comparable with the precision of the transverse velocity components  $v_{x'}$  and  $v_{y'}$ . This subsample of 19 wide binaries gives essentially the same value of  $\Gamma$  with somewhat larger statistical uncertainties due to the smaller sample size. Again, it is reassuring of our conclusions that increasing the precision cut on the radial velocities yields consistent results when compared to the full clean sample, showing convergence and robustness regarding this parameter.

In the right panels of Figure 13, we consider the subsamples obtained by excluding systems with unusually high 3D velocity  $v_{\text{obs}} (> v_{\text{escN}})$  from the corresponding left-panel samples, where  $v_{\text{escN}}$  is the Newtonian escape velocity as would be obtained through modeling the system assuming Newtonian gravity with a fixed value of  $\Gamma$  (see Figure 8). Based on the Newtonian modeling results, the excluded systems are likely to be *individually* incompatible with Newtonian gravity unless they are flybys with parabolic or hyperbolic orbits caught in instantaneous relative motion by chance or their current velocity data suffer from unknown systematic errors. While these systems can be compatible with MOND gravity with boosted effective gravitational constant, some or all of these systems may be regarded potentially suspicious from the viewpoint of standard gravity. Thus, it is of interest to check whether the MONDian nature of the consolidated PDF persists even if these systems are excluded.

The right panels of Figure 13 show that the consolidated value of  $\Gamma$  is significantly reduced, as expected from numerical experiments. For example, modeling and consolidating simulated data (assuming Newtonian gravity) shown in Figures 4 and 8 of K.-H. Chae (2025a) demonstrate that selectively removing individual PDFs covering only higher values of  $\Gamma$  will result in a biased consolidated PDF that is shifted from the assumed gravity. However, the consolidated PDFs are still inconsistent with Newton at a  $> 2\sigma$  level. In other words, the sample as a whole appears to have an anomaly or MOND(-like) signal that cannot be naturally removed. If one wants to interpret our results for the full clean

sample within a Newtonian framework, one needs to assume that all  $v_{\text{obs}} > v_{\text{escN}}$  cases, however unlikely they are (see below), must be unbound systems, the removal of which should yield agreement with Newtonian expectations, as all remaining binaries are individually consistent with Newtonian expectations. However, this is not the case. Even removing all  $v_{\text{obs}} > v_{\text{escN}}$  binaries leaves us with a sample that collectively is still discrepant with the Newtonian hypothesis. Since the included binaries are individually consistent with Newton, it is clear that being inconsistent with Newton as a sample stems from requiring orbital parameter distributions (typically inclination and orbital phase) which are at odds with the isotropy and Keplerian assumptions of the method.

Interestingly, the consolidated PDFs excluding systems with  $v_{\text{obs}}/v_{\text{escN}} > 1$  agree well with the gravity boost range predicted by MOND gravity numerical simulations (K.-H. Chae & M. Milgrom 2022; J. Pfamm-Altenburg 2025) although the distinction from Newton is less pronounced. Thus, it is tempting to exclude the systems with  $v_{\text{obs}}/v_{\text{escN}} > 1$  even from a MOND point of view, but we believe that such a choice is not warranted for several reasons.

First of all, the systems with  $v_{\text{obs}}/v_{\text{escN}} > 1$  have passed all predefined observational selection criteria for pure wide binaries as the other systems. There is no compelling reason to exclude them on the basis of the currently available observational information. Table 3 summarizes some properties of interest for these systems. All these systems have relatively precise values of  $v_r$  from Gaia DR3 (Gaia uncertainties smaller than  $\approx 0.3 \text{ km s}^{-1}$  are rare: see K.-H. Chae 2025a) and they all agree excellently with the more precise independent values measured at different epochs. In all cases, the radial separation is consistent with zero up to the measurement errors. In three cases, the projected separation is less than 20 kau and the metallicity difference between the two stars is nearly zero or not significant considering the Gaia DR3 [M/H] realistic errors (see Section 3.3.2). One system (ID #33) may have a moderate issue. The projected separation is relatively large with  $s = 30.34 \text{ kau}$  and the metallicity difference is the largest among the clean sample with  $\Delta[M/H] \equiv [M/H]_A - [M/H]_B \approx -0.7$ . Because the two stars of this system have effective temperatures  $> 4600\text{K}$ , the Gaia DR3 metallicity difference cannot be specifically explained by the known bias. However, the  $1\sigma$  range of realistic errors of [M/H] can be as large as  $\approx 0.7$  (see Figure 11 of R. Andrae et al. (2023)). Moreover,  $v_r$  of this system was measured twice by the LCO and it is consistent with the relatively precise Gaia DR3 value from about 10 years earlier epoch. Thus, even this system needs not be excluded.

Here it is interesting to note that the presence of  $v_{\text{obs}}/v_{\text{escN}} > 1$  was first noticed in the R. Saglia et al. (2025) sample with the occurrence rate of 1/8 among low-acceleration systems (K.-H. Chae 2025b). In our

## Bayesian inference of $\Gamma$ at $g_N < 10^{-9} \text{ m s}^{-2}$ with the thermal prior on eccentricity

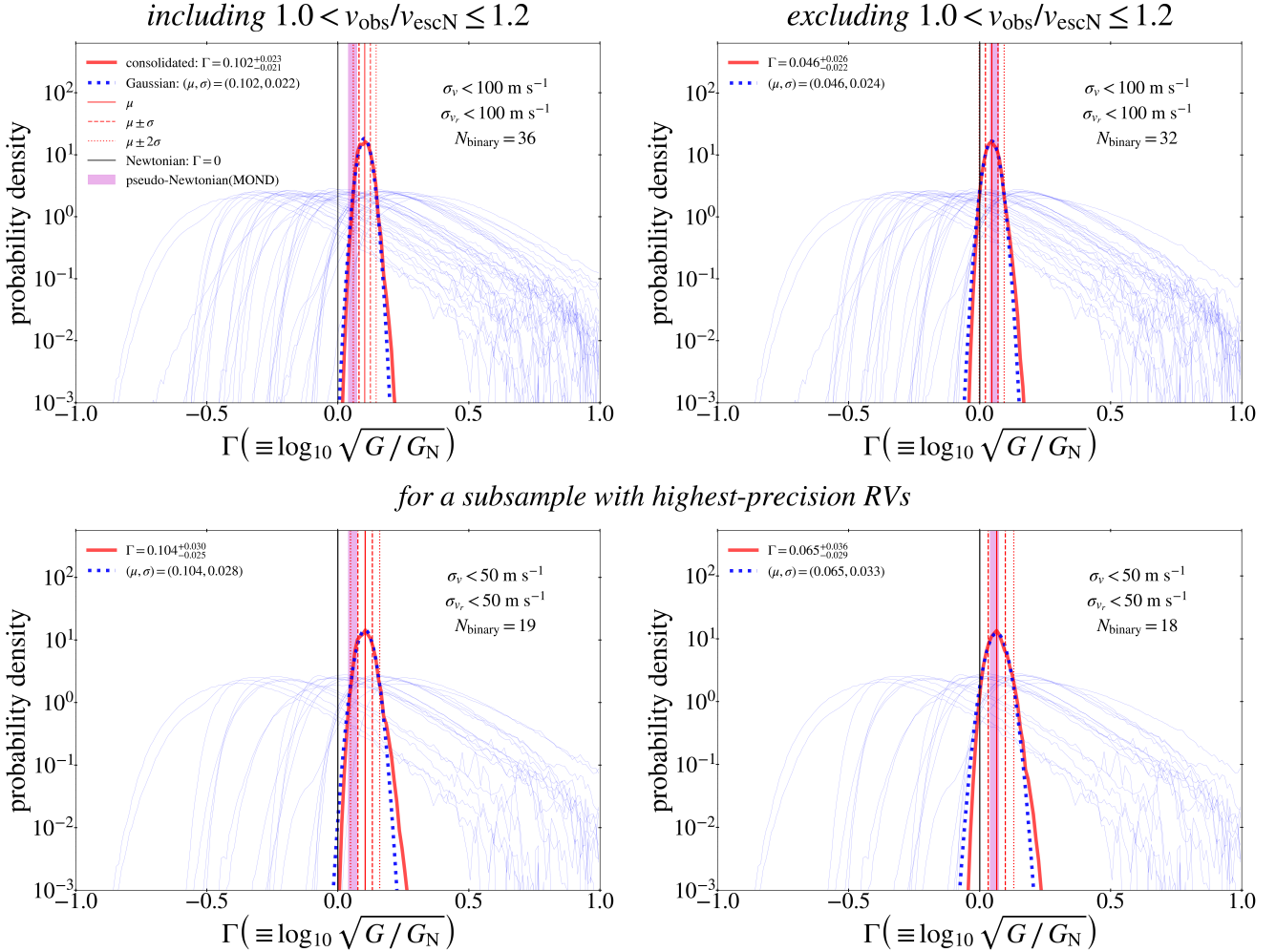


**Figure 13.** This figure shows results on the Bayesian inference of  $\Gamma$  for the clean sample. In each panel thin blue curves represent individual PDFs and thick red curve is the consolidated PDF. The left panels show results including wide binaries with  $1.0 < v_{\text{obs}}/v_{\text{escN}} \leq 1.2$  while the right panels show results excluding them.

clean sample we have identified 3 more cases from the newly added 28 wide binaries. Thus, these newly added systems suggest that cases with  $1 < v_{\text{obs}}/v_{\text{escN}} \lesssim 1.2$  (mildly gravitationally-unbound from the Newtonian perspective) are common with an occurrence rate of about  $\approx 0.1$ , confirming that the system discovered by R. Saglia et al. (2025) is not a fluke.

Secondly, the (mildly) Newtonian-unbound systems are not particularly different from the Newtonian-bound systems with  $0.9 \lesssim v_{\text{obs}}/v_{\text{escN}} < 1$ . Table 3 summarizes the key properties of the data and the inferred values of  $\Gamma$  for 11 wide binaries with  $v_{\text{obs}}/v_{\text{escN}} \gtrsim 0.9$

that are most responsible for the amplitude of the gravitational anomaly in the clean sample. The values of  $v_p$  (the scalar sky-plane relative velocity) and  $|v_r|$  are statistically similar between the two subsamples with  $v_{\text{obs}}/v_{\text{escN}} > 1$  or  $0.9 \lesssim v_{\text{obs}}/v_{\text{escN}} < 1$ . The inferred PDFs of  $\Gamma$  are all similar with similar median values in the range  $0.22 \leq \Gamma \leq 0.40$  and similar confidence widths. No individual PDF is abnormal compared with the other PDFs. This means that the gravitational anomaly is not driven by a few exceptional systems but by the collective properties of many systems.

**Table 3. Some properties of wide binaries with  $v_{\text{obs}}/v_{\text{escN}} \gtrsim 0.9$  from the clean sample:** the first four are the Newtonian unbound systems with  $v_{\text{obs}}/v_{\text{escN}} > 1$ .

ID <sup>a</sup>	$d_M$ <sup>b</sup> [pc]	$v_p$ <sup>c</sup> [km s <sup>-1</sup> ]	$v_r$ <sup>d</sup> [km s <sup>-1</sup> ]	$v_{r,\text{DR3}}$ <sup>e</sup> [km s <sup>-1</sup> ]	$v_{\text{obs}}$ <sup>f</sup> [km s <sup>-1</sup> ]	$s$ <sup>g</sup> [kau]	$z'$ <sup>h</sup> [kau]	$\Gamma$ <sup>i</sup>	$v_r$ source
3	131.31	$0.369 \pm 0.019$	$0.386 \pm 0.051$	$0.527 \pm 0.327$	$0.534 \pm 0.039$	19.32	$74.0 \pm 94.4$	$0.400^{+0.234}_{-0.142}$	APOGEE
33	73.86	$0.243 \pm 0.010$	$-0.345 \pm 0.060$	$-0.181 \pm 0.245$	$0.422 \pm 0.049$	30.34	$41.1 \pm 37.1$	$0.313^{+0.239}_{-0.130}$	LCO
42	33.55	$0.228 \pm 0.005$	$-0.595 \pm 0.082$	$-0.692 \pm 0.233$	$0.637 \pm 0.076$	7.870	$-7.34 \pm 7.35$	$0.277^{+0.239}_{-0.131}$	LCO
59	100.27	$0.383 \pm 0.009$	$-0.861 \pm 0.015$	$-1.092 \pm 0.239$	$0.942 \pm 0.014$	5.779	$46.1 \pm 52.0$	$0.339^{+0.246}_{-0.113}$	HARPS
25	93.79	$0.580 \pm 0.009$	$-0.337 \pm 0.086$	$-0.132 \pm 0.257$	$0.670 \pm 0.043$	6.524	$13.3 \pm 31.4$	$0.243^{+0.231}_{-0.117}$	LCO
32	105.03	$0.344 \pm 0.008$	$-0.327 \pm 0.042$	$-0.631 \pm 0.254$	$0.474 \pm 0.029$	13.10	$5.01 \pm 52.0$	$0.240^{+0.248}_{-0.117}$	LCO
36	82.84	$0.328 \pm 0.006$	$-0.561 \pm 0.082$	$-0.514 \pm 0.236$	$0.650 \pm 0.071$	6.694	$22.7 \pm 23.6$	$0.226^{+0.223}_{-0.125}$	LCO
39	59.47	$0.475 \pm 0.006$	$-0.055 \pm 0.046$	$-0.067 \pm 0.187$	$0.478 \pm 0.008$	11.054	$42.9 \pm 20.2$	$0.247^{+0.224}_{-0.124}$	LCO
53	108.61	$0.341 \pm 0.013$	$-0.468 \pm 0.017$	$-0.596 \pm 0.286$	$0.579 \pm 0.015$	4.829	$98.8 \pm 56.1$	$0.314^{+0.254}_{-0.154}$	HARPS
54	116.26	$0.660 \pm 0.009$	$0.449 \pm 0.004$	$0.354 \pm 0.215$	$0.799 \pm 0.008$	4.935	$-18.5 \pm 50.6$	$0.222^{+0.233}_{-0.108}$	HARPS
75	40.92	$0.280 \pm 0.004$	$0.747 \pm 0.021$	$0.668 \pm 0.181$	$0.798 \pm 0.020$	4.703	$-3.0 \pm 9.6$	$0.218^{+0.223}_{-0.105}$	Scarpa

<sup>a</sup> See Table 2.

<sup>b</sup> Error-weighted mean of the measured distances of Stars A & B.

<sup>c</sup> Scalar relative sky-plane velocity  $v_p$  ( $\equiv \sqrt{v_{x'}^2 + v_{y'}^2}$ ).

<sup>d</sup> Relative radial velocity between the pair  $v_r \equiv \text{RV}_A - \text{RV}_B$  from Table 2.

<sup>e</sup> Relative radial velocity between the pair from Gaia DR3.

<sup>f</sup> Scalar relative 3D velocity  $v_{\text{obs}}$  ( $\equiv \sqrt{v_p^2 + v_r^2}$ ).

<sup>g</sup> Sky-plane 2D separation between the pair from K. El-Badry et al. (2021).

<sup>h</sup> Relative distance (radial separation) between the pair,  $z' = -(d_B - d_A)$ .

<sup>i</sup> The gravity anomaly parameter given by Equation (1).

Thirdly, these wide binaries selected from the solar neighborhood of  $d < 150$  pc are extremely unlikely to be random chance associations. With a local number density of stars  $n$  estimated from the Gaia DR3 database and the well-known distribution of peculiar velocity components in the solar neighborhood, we estimate that a randomly selected star to have a fly-by with projected separation  $s < s_{\text{max}}$ , radial separation  $l < l_{\text{max}}$ , and scalar relative 3D velocity  $v (\equiv \sqrt{v_{x'}^2 + v_{y'}^2 + v_{z'}^2}) < v_{\text{max}}$  is

$$p_{\text{chance}} \approx (1.4 - 3.4) \times 10^{-8} \frac{n}{0.15 \text{ pc}^{-3}} \times \left( \frac{s_{\text{max}}}{30 \text{ kau}} \right)^2 \frac{l_{\text{max}}}{100 \text{ kau}} \left( \frac{v_{\text{max}}}{1 \text{ km s}^{-1}} \right)^3, \quad (4)$$

where the 1-dimensional velocity dispersion of peculiar velocities is assumed to be in the range  $30 - 40 \text{ km s}^{-1}$ . For the clean sample, the nominal choices of Equation (4) are conservative, and thus for a sample of 2 million stars within 150 pc, we expect  $\lesssim 0.04$  cases, meaning that practically no fly-by cases meeting the thresholds should be observed. Thus, the observed 4

cases from the clean sample are extremely unlikely to be chance associations unrelated to gravity. Moreover, the 4 cases are a lower limit to the true number of binaries with  $v_{\text{obs}} > v_{\text{escN}}$  because they were selected from samples of wide binaries that meet extremely strict observational constraints (e.g., many from the basic-cut sample were excluded for now, but some of them could be included in the future, once more high quality multi-epoch radial velocities are available). In other words, not all pairs within 150 pc have sufficient data to check whether they meet the selection criteria of the clean sample.

Lastly, existing MOND gravity models *do* predict<sup>5</sup> the range of  $v_{\text{obs}}/v_{\text{escN}}$  observed in the clean sample. Moreover, whatever MOND gravity models predict, they (i.e. nonrelativistic gravity models) are far from an established theory. Thus, even the predictions of the current MOND models need to be taken with a grain of salt. Above all, because this work is about a measurement of  $\Gamma$ , it should not be controlled by any existing gravity models.

<sup>5</sup> We thank Cezary Migaszewski for sharing numerical simulations results prior to publication.

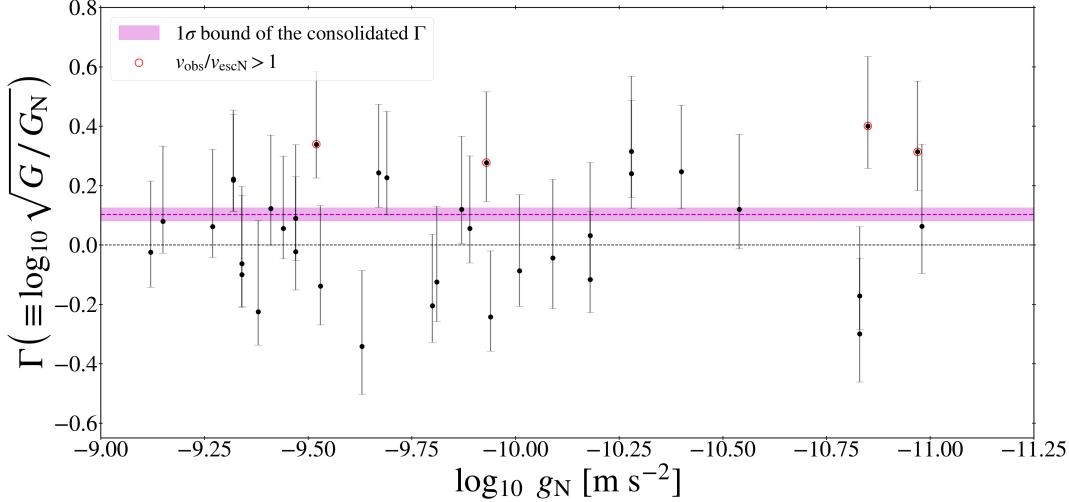


**Figure 14.** This figure shows the inferred value of  $\Gamma$  as a function of the internal acceleration  $g_N$  for the clean sample of 36 wide binaries shown in the top left panel of Figure 13.

Having noted in the above that the systems with  $v_{\text{obs}}/v_{\text{escN}} > 1$  need not be excluded from observational and theoretical points of view, we now examine whether  $\Gamma$  shows any trend with the internal acceleration  $g_N$  within our considered limit  $g_N < 10^{-9} \text{ m s}^{-2}$ . Figure 14 shows the individually inferred values of  $\Gamma$  with respect to  $\log_{10} g_N$  for the clean sample. First of all, individual values provide insights why the consolidated value (which corresponds to the effective or representative value for the whole population) of  $\Gamma$  cannot be zero. All individual values of  $\Gamma < 0$  are consistent with zero within about  $1.5\sigma$ . However, there are 10 individual values of  $\Gamma > 0$  that are  $\gtrsim 2\sigma$  away from zero. These values shift the consolidated value by  $\approx +0.1$  so that all values agree with the shifted consolidated value within  $\approx 2\sigma$ .

Now while it is not easy to find a well-defined trend of  $\Gamma$  with  $g_N$  from this small sample, it is clear that a consolidated  $\Gamma$  is clearly  $> 0$  in the lowest acceleration regime that is fully MONDian with  $\lesssim 10^{-10} \text{ m s}^{-2}$ . Also, a subsample of the relatively higher acceleration range  $10^{-9.5} < g_N < 10^{-9} \text{ m s}^{-2}$  does not include any case with  $v_{\text{obs}}/v_{\text{escN}} > 1$  and has a relatively lower value for the consolidated  $\Gamma$ . This would be qualitatively in agreement with the general trend of MOND gravity. We refrain from further analysis on this point here, as our intent is to focus on a determination of the effective value of  $\Gamma$ , a well-defined quantity useful to assess the presence (or absence) of a gravitational anomaly with respect to Newtonian gravity.

#### 4.2. Additional and auxiliary results

In this subsection we present additional results obtained by varying the prior on eccentricity from the nominal choice of the thermal prior. We also check the posterior distributions of the orbit and orientation pa-

rameters with respect to the prior distributions required by the randomness of the sample.

Although our nominal choice is the thermal distribution, the most relevant distribution of eccentricities for wide binaries with  $s > 1$  kau would be a superthermal distribution of  $\alpha \approx 1.3$  in  $f_{\text{pr}}(e) = (1 + \alpha)e^\alpha$ , according to the H.-C. Hwang et al. (2022) Bayesian study of a large number of wide binaries with precise projected displacements and velocities. Thus, we consider a superthermal prior with  $\alpha = 1.3$ . It turns out that the results with the superthermal prior are nearly indistinguishable from the results with the thermal prior. For the whole clean sample, we have  $\Gamma = 0.103^{+0.027}_{-0.021}$ . This is not surprising because the moderate difference between the thermal distribution and the specific superthermal distribution can make only a tiny effect on the parameter inference when the precise 3D velocities along with the nearly exact two sky-projected displacements have some constraining power on the orbital parameters. We also consider the uninformative flat prior on eccentricity to investigate the role of the eccentricity prior in the gravity inference and at the same time to gauge the power of our sample in constraining the eccentricity distribution.

Figure 15 shows the results on  $\Gamma$  with the flat prior on eccentricity. Compared with the nominal results, the inferred value of  $\Gamma$  is slightly reduced to  $\Gamma = 0.092^{+0.021}_{-0.017}$  but the significance of the deviation from Newton is somewhat stronger (a  $5.4\sigma$  deviation) because individual PDFs get somewhat narrower, and consequently the consolidated PDF is also narrower. Thus, perhaps contrary to expectation, the flat prior on eccentricity actually makes Newtonian gravity even more strongly discrepant with our wide binary sample.

Figure 16 shows the posterior distributions of the orbit, inclination, and mass parameters for the two Bayesian results with the thermal or flat prior on ec-

## Bayesian inference of $\Gamma$ at $g_N < 10^{-9} \text{ m s}^{-2}$ with the flat prior on eccentricity

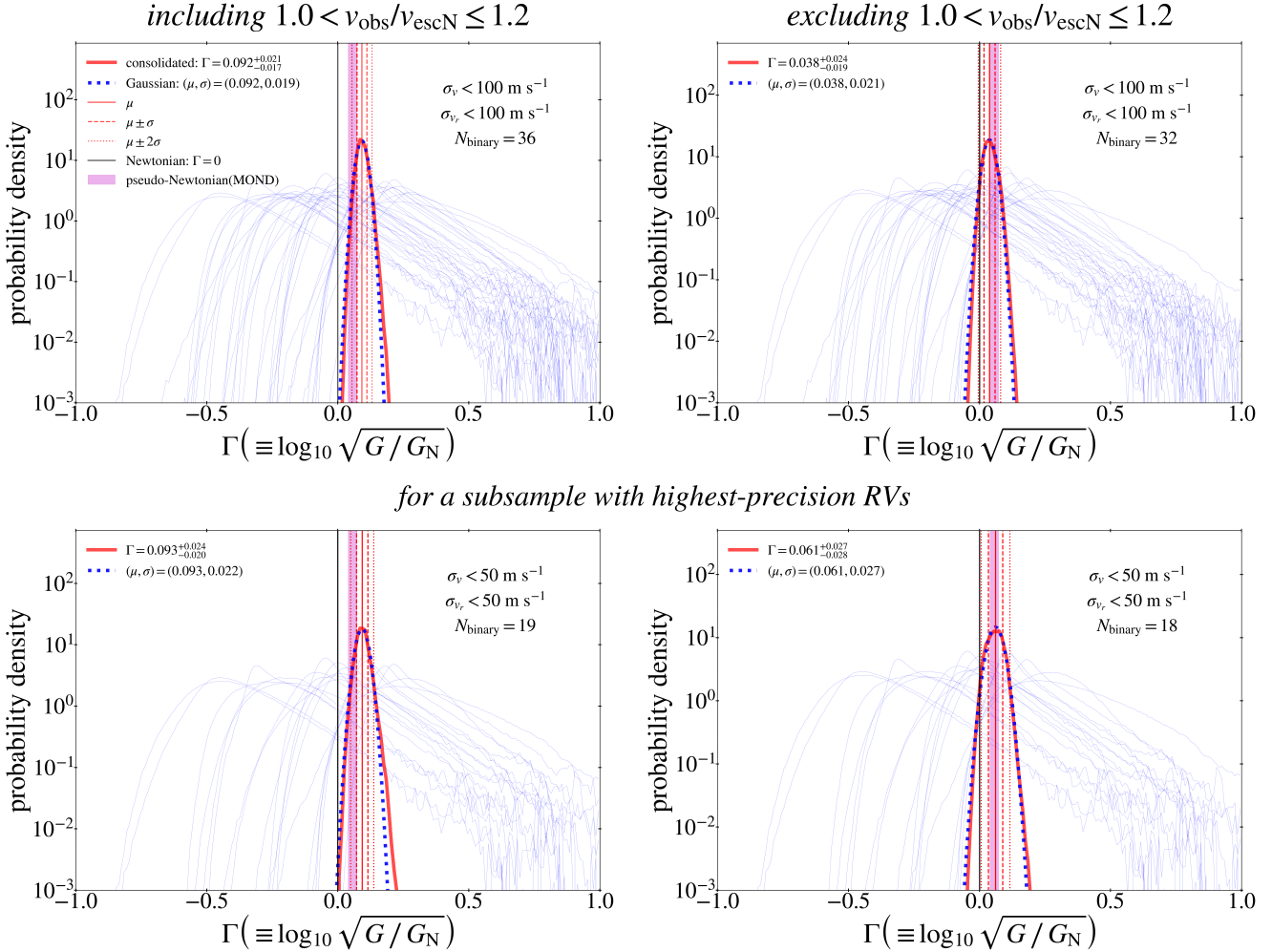


**Figure 15.** Same as Figure 13 but with the flat prior on eccentricity.

centricity. Due to the degeneracy between the gravity parameter  $\Gamma$  and the other parameters in fitting the data  $(\mathbf{r}, \mathbf{v})$ , when  $\Gamma$  is free while the other parameters are constrained by their priors, the posterior distributions of the latter are expected to collectively follow the prior distributions as a population. If the posterior distribution of a parameter is significantly different from the prior individually or collectively, that would strongly indicate that the kinematic data prefer a value or distribution different from the prior.

Figure 16 shows that the parameters overall follow the prior distributions. In particular, the posterior distribution of the orbit true anomaly parameter  $\Delta\phi (= \phi - \phi_0)$  is well consistent with the  $e$ -convolved distribution fulfilling the required self-consistency. This means that the inferred PDFs of  $\Gamma$  are based on orbital inclination and occupancy distributions consistent with isotropy and random presentations.

For the thermal prior, the posterior distribution of  $e$  matches well the prior distribution. However, for the flat prior, the posterior distribution of  $e$  is tilted toward the upper limit indicating that the data prefer a non-flat distribution with  $\alpha > 0$ . However, the relatively moderate tilt may indicate that the kinematic data alone (when  $\Gamma$  is free) are not sufficient to constrain well the orbit parameters, especially due to the large uncertainty of the radial separation  $z'$ .

Finally, we note that if gravity is fixed (e.g., Newtonian or a boosted gravity), the orbit and orientation parameters can be significantly constrained by the data  $(\mathbf{r}, \mathbf{v})$ , and the posterior distributions of the parameters, in particular the orbit true anomaly parameter  $\Delta\phi$ , can be used to test the assumed gravity model, as was investigated in the pilot study by K.-H. Chae (2025b). In such a test, priors should not be imposed on the orbit and orientation parameters because gravity is fixed (so

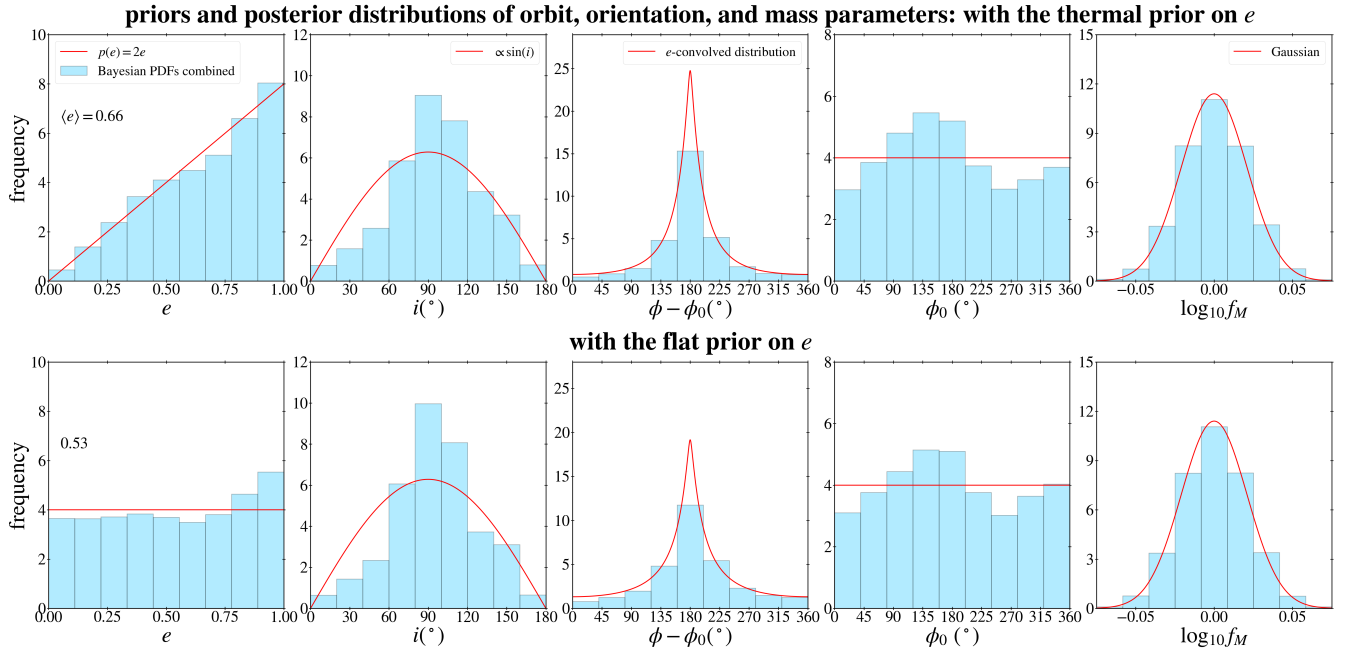


**Figure 16.** Posterior distributions of the orbit, inclination, and mass parameters are compared with the priors represented by red lines/curves. The histogram of a parameter represents the composite of the individual posterior PDFs of the parameter for all 36 wide binaries in the clean sample. The prior distribution of  $\Delta\phi (= \phi - \phi_0)$  is the function (with a rescaled amplitude) given by Equation (3) convolved with  $e$  shown in the leftmost column.

the degeneracy between gravity and orbit parameters is not a concern) and we seek to test the distributions required by the assumed gravity without the influence of any priors. As already noted with a small sample of 8 or 9 wide binaries with  $g_N < 10^{-9} \text{ m s}^{-2}$  by R. Saglia et al. (2025) and K.-H. Chae (2025b), Newtonian gravity requires a biased distribution of  $\Delta\phi$  towards the periastron to compensate for the boosted gravity obtained for the correct prior distribution (see Figure 16), violating Kepler’s second law in a statistical sense for the population. With a 4 times larger low-acceleration sample than the R. Saglia et al. (2025) sample, the statistical significance is now clearly stronger. Thorough statistical tests of Newtonian gravity as well as control boosted gravity (toy) models will be presented in a separate work as those work involves statistical methods such as the Kolmogorov-Smirnov test, the Anderson-Darling test, and Bayesian information criterion (see K.-H. Chae 2025b). We stress that this work is mainly devoted to the construction of the wide binary sample and the “measurement” of  $\Gamma$ , which is the most reliable and straightforward representation of the data (without requiring additional statistical methods) that can be readily carried out with the available code (K.-H. Chae 2025b).

### 4.3. Exploring possible systematic errors: Can the gravitational anomaly be removed?

So far we have presented the main and additional results on the gravity inference along with relevant discussions based on the currently available observational information. Here we further consider extreme possibilities to check whether the low-acceleration gravitational anomaly from the clean sample can be removed. The gravity inference may be affected by variation in modeling inputs or sample selection criteria.

As for modeling inputs, we have already considered a sufficiently wide range of possibilities for the orbit eccentricity. It was also shown that our adopted stellar masses agree well with the Gaia FLAME masses (Figure 11) whenever the latter are available. However, given that gravity inference is directly and significantly affected by the input mass, here we consider the possibility that the masses of all our stars might be 10% larger than the values we have adopted. This is in part motivated from the study by R. Saglia et al. (2025) who quote a maximum of 10% systematic error for their masses based on the HARPS spectra. Our sample is a composite of several subsamples and masses were estimated through independent methods for different subsamples. So it is unlikely that all stellar masses are systematically biased in the same direction by 10%. Thus, the uniform increase of 10% for all stars is an extreme possibility. Figure 17 shows the result on  $\Gamma$  with the increased mass. The inferred value is reduced to  $\Gamma = 0.086^{+0.025}_{-0.020}$ , which

is however still inconsistent with Newtonian at a more than  $4\sigma$  level. This shows that any reasonable adjustment of the currently estimated stellar masses cannot remove the gravitational anomaly.

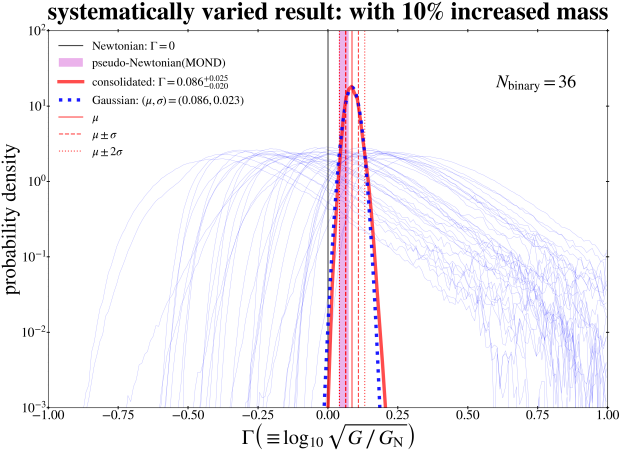


**Figure 17.** Same as the top left panel of Figure 13 but with all masses of the stars increased by 10%.

As for sample selection criteria, we have employed the philosophy of sacrificing statistical significance to maximize the purity of the sample, by taking only wide binaries that pass all the stringent selection criteria *and* have additional observational indicators for kinematically uncontaminated pure binaries. This is why only 17% of the raw sample with relatively precise  $v_r$  (Figure 2) survived in the final clean sample. The purity of the clean sample may be reaffirmed by the fact that none of the posterior PDFs of  $\Gamma$  are abnormal, and in particular, our recovered distributions of orbital phases and inclinations are consistent with isotropy and angular momentum conservation expectations, as shown in Figure 16. However, it is interesting to note that some component stars of our pure binaries are classified as unresolved binaries according to the Gaia DR3 multiple-star classifier (MSC; M. Fouesneau et al. 2023), making binaries triples or quadruples. In line with R. Saglia et al. (2025), we did not use the MSC because it is not reliable on an individual basis.

It turns out that the R. Saglia et al. (2025) sample and our clean sample include systems listed as triples or quadruples in the MSC-based **Object Type** given in the Gaia DR3 online archive. This classification is known to be significant only in a qualitative and statistical sense. Considering our general philosophy of this work, we consider removing systems marked as triples/quadruples by the MSC. Figure 18 shows the result on gravity after excluding the 12 systems (i.e. one third of our clean sample) that include MSC-based unresolved binary stars. The inferred value of  $\Gamma = 0.096^{+0.031}_{-0.028}$  for the remaining 24 binaries is nearly indistinguishable from that for the

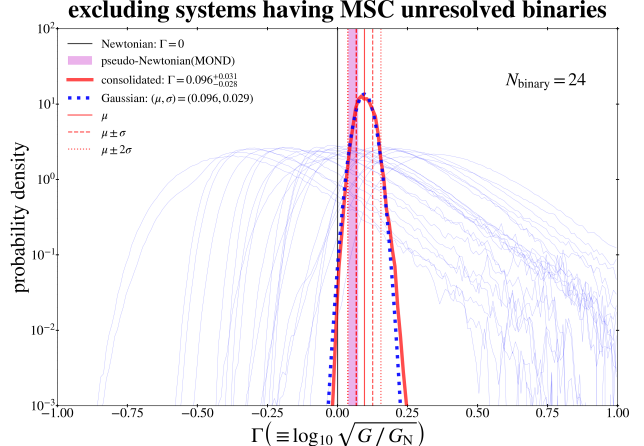


**Figure 18.** Same as the top left panel of Figure 13 but for a subsample excluding systems marked as unresolved binaries (potentially triples or quadruples) in the Gaia DR3 multiple-star classifier.

entire sample other than the slightly increased statistical errors consistent with the reduced sample size. This indicates that the excluded systems are not special but random. If they were triples/quadruples, the inferred  $\Gamma$  for them would be abnormally large because of the systematically underestimated masses and the kinematic contamination due to multiplicity. In that hypothetical case, our inference would shift into accordance with Newtonian expectations once such cases were removed, which is not what happens. This exercise demonstrates that the gravitational anomaly found cannot be removed by invoking hidden unresolved close binaries as per the Gaia DR3 MSC in our clean sample.

Regarding the sample selection, it is of interest to consider only wide binaries whose  $v_r$  are stable over more than several years from direct multi-epoch observations. Speckle observations show that our targets have a low chance of about 5% to have a faint Speckle resolved companion. Since only 10 wide binaries from the clean sample were directly verified to be free of resolved faint companion from our Speckle observations, it is in principle possible that the remaining 26 wide binaries may include one or two cases that may have a faint companion more than tens of kau apart from a component star. However, removing *any* one or two wide binaries from our clean sample has a negligible effect on the inferred value of  $\Gamma$ . Thus, the reaming concern is any unresolved companion within tens of kau from a component star.

Companions of relatively close separation less than several tens au may be missed by Speckle observations with a probability increasing with distance because the same angular resolution limit means an increasing limit of physical separation. Our clean sample already excludes a relatively larger distance of  $> 150$  pc. However, if kinematic contamination in the intermediate separa-

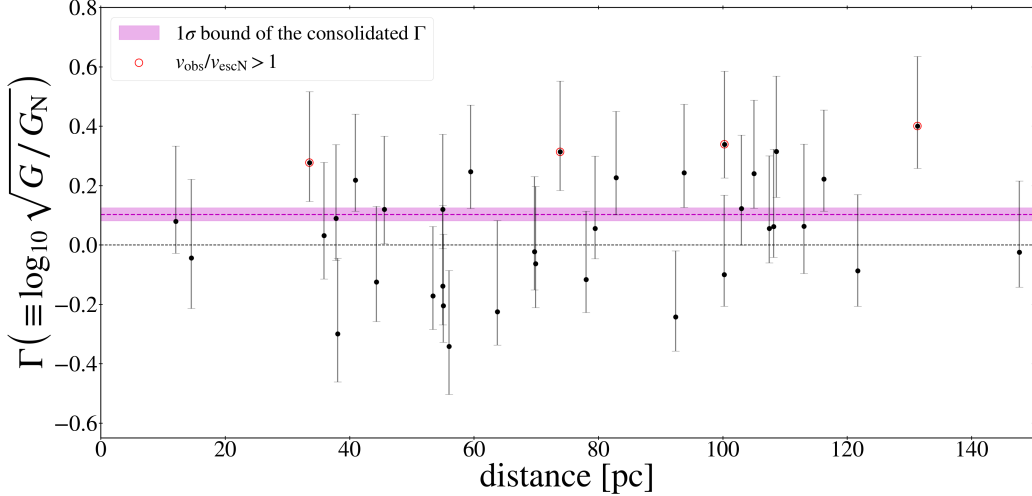


**Figure 19.** Same as Figure 14 but with respect to distance to the binary system.

tion (that cannot be flagged by Gaia’s `ruwe` values: see below) from  $\approx 10$  au to several tens au is present, it is expected to cause a trend in the inferred  $\Gamma$  with distance in our clean sample as wide binaries are distributed over a broad distance range of  $10 < d < 150$  pc. Figure 19 exhibits the individual values of  $\Gamma$  with respect to the distances of the binaries in the clean sample. There is not obvious trend of  $\Gamma$  with  $d$  and the four systems with  $v_{\text{obs}}/v_{\text{escN}} > 1$  are distributed over the entire distance range. This indicates that significant kinematic contamination in the intermediate range is unlikely.

Close companions ( $\lesssim 10$  au) will have kinematic effects on either tangential velocities (preferentially when the orbit of the companion is close to face-on) or radial velocities (preferentially when the orbit of the companion is close to edge-on). The kinematic effects on tangential velocities can be flagged by Gaia’s `ruwe` (V. Belokurov et al. 2020) while those on radial velocities can be flagged through a monitoring observation covering a significant fraction of the orbital period. Because we have already required  $\text{ruwe} < 1.25$ , requiring an observed stability of  $v_r$  over more than several years can complete the observational requirement for pure binaries. Figure 20 shows the inference of  $\Gamma$  for 21 wide binaries with time baselines of 3 - 11 years taken (excluding shorter baseline cases) from those shown in the right panel of Figure 10. Again, the inferred value of  $\Gamma = 0.121^{+0.034}_{-0.026}$  is strongly discrepant with Newton.

Therefore, it seems impossible to remove the gravitational anomaly seen in the clean sample within any conceivable variation of the currently available observational information. Yet, one might be still skeptical of the gravitational anomaly and want to find a way to remove it. As a cautionary tale of any fabricated result through an intentional or unintentional distortion of our sample (or any other samples present and future), we carry out an exercise of deliberately removing choice

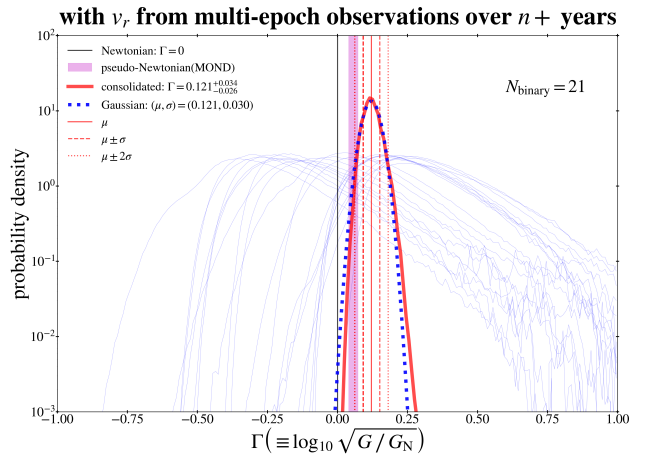


**Figure 20.** Same as the top left panel of Figure 13 but for a subsample with  $v_r$  stable from two observations separated by 3 - 11 years (except for 4 systems from those shown in the right panel of Figure 10).

systems in order to produce a Newtonian result. For this we consider selectively removing wide binaries that are responsible for the gravitational anomaly. Figure 21 shows a contrived result obtained by removing 9 wide binaries (a quarter of the clean sample) that have highest  $v_{\text{obs}}/v_{\text{escN}}$  values. This is a false result that appears to agree with Newton remarkably well. The removal of the 9 systems with the smallest values of  $v_{\text{obs}}/v_{\text{escN}}$  would correspondingly shift our results to artificially large values of  $\Gamma$ , while removing 9 random binaries on average leaves our inference unchanged, beyond the expected increase of the confidence intervals due to the reduced sample.

The Gaia limiting magnitude of 20.5 out to the limit of our sample of 150 pc implies that stellar companions

at separations beyond the Gaia resolution of 0.3 arcsec can be excluded as contaminating our sample. At closer separations, the combination of only 5% close companions identified by our Speckle campaign and the clearing of a subsample of our final clean sample through this technique, exclude a further range of potential stellar companions. In order to bring our results into consistency with Newtonian expectations we would require, as detailed above, about 9 of our binaries to be contaminated, something which would require a probability of about  $(0.05)^9$  if unresolved stellar companions were to blame. At even closer separation, where close binary periods become comparable to the Gaia DR3 temporal range of 34 months, the use of `ruwe` restrictions for all (e.g. see [A. Castro-Ginard et al. \(2024\)](#) where the presence of unresolved stellar companions of all types has been shown to be incompatible with stars in DR3 for values of `ruwe`  $> 1.15$ , a limit only one of our binaries in the clean sample crosses) and consistent multi-epoch high quality radial velocity measurements, in practice eliminate stellar companion contamination as a concern.

The only remaining potential contaminants to reconcile our observations with Newtonian gravity would be brown dwarfs at separations above about 3 au, where the inner orbital periods would be larger than 34 months. Here we enter the ‘brown dwarf dessert’, where independent observations have consistently identified an absence of brown dwarf companions to stars of the type we are using, with masses a little below one solar mass (e.g., [A. L. Kraus et al. 2011](#)). Direct searches using eclipse and lensing surveys have shown this ‘dessert’ to extend out to a few tens of au. Dynamical models of brown dwarf formation have shown instabilities in fragmenting disks to preclude the formation of stable brown dwarfs about stars of the type used here out to about 200 pc (e.g., [E. I. Vorobyov 2013](#)). Beyond such distances the kinematic signal of such a hypothetical contaminant becomes comparable to the noise level in our study, and the possibility ceases to be relevant. Hence, invoking a hypothetical distribution of undetected brown dwarf companions of sufficient frequency to explain the gravitational anomaly we detect within a Newtonian framework would not only be a contrived and *ad hoc* proposal lacking any independent evidential support, but would also run counter to all observational and theoretical knowledge on the point.

## 5. MEANINGS AND IMPLICATIONS OF THE RESULTS

In this work, we have assembled a sample of pure binaries and then focused on testing Newtonian gravity at low internal acceleration  $\lesssim 10^{-9} \text{ m s}^{-2}$  by measuring  $\Gamma$  assuming elliptical orbits. If observed wide binaries represent random phases of Newtonian elliptical orbits, the consolidated PDF of  $\Gamma$  must be consistent with zero as demonstrated for wide binaries with relatively small separation  $\lesssim 1$  kau or relatively strong internal acceleration

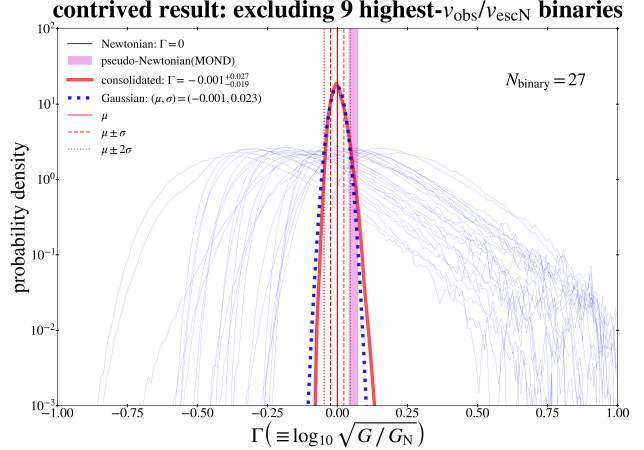


**Figure 21.** Same as the top left panel of Figure 13 but for a subsample selectively excluding a quarter of the sample. The excluded 9 wide binaries are those having the highest values of  $v_{\text{obs}}/v_{\text{escN}}$  (see Tables 2 and 3).

$\gtrsim 10^{-8} \text{ m s}^{-2}$  ([K.-H. Chae 2025a,b](#)). If not, it simply means that Newtonian gravity is broken at low acceleration (whatever the implication for gravity may be) because the result derived assuming the Newtonian framework does not agree with the Newtonian prediction.

The inferred value of  $\Gamma$  is a pure measurement/quantification of the degree by which the data deviate from Newton under the specific assumption of elliptical orbits and angular momentum conservation. Thus, while it provides a direct test of Newtonian gravity, it is not straightforward to test specific nonstandard gravity such as MOND models ([J. Bekenstein & M. Milgrom 1984; M. Milgrom 2010](#)) using  $\Gamma$ . The orbits of wide binaries in a nonstandard model can only be obtained by numerically solving the nonlinear field equation ([J. Pfamm-Altenburg 2025](#)). Mock data  $(\mathbf{r}, \mathbf{v})$  can be obtained from the mock orbits, and the mock data can be modeled in the same manner as the real data. Then, the inferred values of  $\Gamma$  for the mock data can be compared with those for the real data obtained here to test the assumed gravity model.

Simply obtaining a boost factor for the gravitational parameter through  $\gamma = G/G_N = 10^{2\Gamma}$  and testing a MOND model with it should be regarded as only a first-order approach. In concordance with the results mostly based on the 2D sky-plane velocities  $v_p$  from recent works led independently by two of us ([K.-H. Chae 2023, 2024a,b, 2025a,b; X. Hernandez 2023; X. Hernandez et al. 2024b; X. Hernandez & P. Kroupa 2025; Y. Yoon et al. 2025](#)), the first-order test shows that the MOND predicted gravitational boost is supported by our clean sample.

In the literature, there have been efforts (e.g., see [X. Hernandez et al. \(2024a\)](#) for a review) to discriminate

between Newton and MOND (or MOND-like gravity) in the low-acceleration regime using general samples of wide binaries that include triples and higher-order multiples (and even gravitationally unbound fly-bys). In principle, such an approach can work and should be concordant with the direct measurement of  $\Gamma$ . For that approach to work, two conditions must be met. First, the prediction of MOND models must be accurately correct. As J. Pfamm-Altenburg (2025) showed, analytical or numerical calculations under simplifying assumptions (e.g., one-particle equivalent description) can be misleading for wide binary orbital motions under the strong ( $\approx 1.8a_0$ ) external field of the Milky Way. None of the existing studies used correct numerical solutions to date. Second, the degeneracy among gravity, the fraction of triples and higher-order multiples ( $f_{\text{multi}}$ ) in a sample of apparent binaries, and the fraction of fly-bys should be well under control. The fraction  $f_{\text{multi}}$  can be calibrated using a control subsample of small-separation binaries whose individual stars are required to satisfy the same observational criteria (e.g.,  $S/N$  of velocities,  $\text{ruwe}$ , etc) as those of the main subsample of wide binaries of interest. Fly-bys can be removed by requiring a threshold on the scalar relative velocity between the pair. Unfortunately, the studies in question failed to do either calibrate  $f_{\text{multi}}$  or remove fly-bys. Our clean sample of wide binaries (and future extended samples) have no fly-bys and satisfy  $f_{\text{multi}} = 0$ , so it may be used to discriminate between Newton and MOND in the future.

As identified by recent independent studies (e.g. C. Pittordis et al. 2025), the most serious systematic up to our present study was the potential presence of undetected multiple systems. Here we have very substantially reduced that possibility through a series of independent approaches such as the use of multi-epoch radial velocity observations, the consistency of Hipparcos and Gaia proper motion observations, the presence of consistent metallicities for the two components of a binary, and the use of Speckle imaging to rule out extra components. Note that D. Manchanda et al. (2023) recently explored a range of follow-up observational techniques towards solving this issue, and identify Speckle interferometry as the leading technique towards guaranteeing pure binary samples.

## 6. SUMMARY, CONCLUSION, AND OUTLOOK

We have collected a purest possible statistical sample of 36 solar neighborhood wide binaries having low internal accelerations ( $\lesssim 10^{-9} \text{ m s}^{-2}$ ) based on an unprecedented combination of various observational data including our crucial new observations of Speckle interferometric imaging and spectroscopic measurements of radial velocities. We have then carried out the most thorough and complete study of the internal dynamics of wide binaries to date, through the Bayesian 3D modeling methodology.

We started from assembling a new collection of 306 Gaia DR3 wide binaries with relatively precise radial velocities. Speckle interferometric imaging of 414 wide binaries of similar qualities shows that about 5% can have resolvable faint companions. From the initial collection, we carefully selected a high-quality sample of 75 isolated wide binaries, based on limits such as distance  $< 150$  pc from the Sun, Gaia's  $\text{ruwe} < 1.25$ , a narrow locus in the CM diagram, and relative radial velocity ( $v_r$ ) error  $< 100 \text{ m s}^{-1}$ .

We then included in the final statistical clean sample only those wide binaries for which multi-epoch measurements of  $v_r$  showed no detectable variability, in most cases over more than several years, and/or Speckle observations have not detected any resolved faint companion. Wide binaries in the sample have highest-quality 3D relative velocities: the scalar sky-plane relative velocity  $v_p$  (between the pair) has an error smaller than  $20 \text{ m s}^{-1}$  with a median of  $7.5 \text{ m s}^{-1}$ , and the relative radial velocity  $v_r$  has an error smaller than  $100 \text{ m s}^{-1}$  with a median of  $47 \text{ m s}^{-1}$ . The clean sample is further verified by a consistency check between Hipparcos and Gaia relative proper motions over the  $\approx 25$ -year period covered by the two observations, and the metallicity consistency between the component stars of the binaries.

The Bayesian inference method of gravity (K.-H. Chae 2025a,b) using 3D relative velocities is applied to recover the effective value of the gravitational constant  $G (= \gamma G_N)$  in the low acceleration regime, under the assumption of elliptical orbits and angular momentum conservation. Despite the relatively small sample of 36 wide binaries, the 3D velocity modeling algorithm allows strong constraints on gravity. Our findings can be summarized as follows:

- We find  $\Gamma \equiv \log_{10} \sqrt{\gamma} = 0.102_{-0.021}^{+0.023}$  for the whole clean sample, a  $5\sigma$  falsification of the hypothesis that Newtonian gravity can be extrapolated to the low acceleration regime. This result cannot be significantly changed by a reasonable systematic variation of stellar masses or any other reasonable variation in sample or modeling inputs such as orbital eccentricity prior.
- We find that all binaries satisfy  $v_{\text{obs}}/v_{\text{escN}} \lesssim 1.2$  where  $v_{\text{obs}}$  is the magnitude of the observed 3D relative velocity and  $v_{\text{escN}}$  is the theoretical escape velocity assuming Newtonian gravity. The upper limit of  $\approx 1.2$  is consistent with numerical orbits from numerical solutions of MOND nonlinear field equations. However, it is unclear whether this is a coincidence due to the small sample size or systems with  $v_{\text{obs}}/v_{\text{escN}} > 1.2$  will be found in future samples.
- We find 4 Newtonian-unbound systems with  $1 < v_{\text{obs}}/v_{\text{escN}} \lesssim 1.2$  from our clean sample, with an occurrence rate of  $1/9$ . Because  $v_{\text{obs}} < 1 \text{ km s}^{-1}$

(i.e., they have essentially the same 3D velocities within the Milky Way with a small velocity gradient consistent with a relative motion under mutual gravity) in these systems, the probability that any of these systems is a chance association (fly-by) in 3D space is negligibly small. It will be interesting to see whether this occurrence rate persists in larger future samples.

Our  $2\sigma$  range of the boost factor  $1.32 < \gamma < 1.94$  can be consistent with some nonstandard theories of gravity including MOND gravity models (J. Bekenstein & M. Milgrom 1984; M. Milgrom 2010). However, the current precision is not sufficient to distinguish between such models, and a proper test of such models require additional analyses based on mock data from numerical solutions of the nonlinear gravitational field equations (see Section 5). Ongoing high quality radial velocity and Speckle interferometry observational campaigns will result in larger samples to further refine the results presented here.

#### ACKNOWLEDGMENTS

We thank Cezary Migaszewski for sharing the distributions of  $v_{\text{obs}}/v_{\text{escN}}$  obtained from numerical solutions of MOND gravity. We thank R. A. M. Cortés for the assistance with the Hipparcos archive data. We thank Arthur Kosowsky, Cezary Migaszewski, and Jan Pfamm-Altenburg for discussions. This work was supported by the National Research Foundation of Korea (NRF-2022R1A2C1092306). X.H. acknowl-

edges financial assistance from SECIHTI SNII and UNAM DGAPA PAPIIT grant IN-102624. V.O. acknowledges financial assistance from UNAM DGAPA PAPIIT grant IN-114123. D.L. acknowledges support from Basic Science Research Program through the National Research Foundation of Korea funded by the Ministry of Education (RS-2025-25419201 and RS-2022-NR070872). Y.-W.L. acknowledges support from the NRF of Korea to the Center for Galaxy Evolution Research (RS-2022-NR070872, RS-2022-NR070525). This work has made use of data from the European Space Agency (ESA) mission Gaia (<https://www.cosmos.esa.int/gaia>), processed by the Gaia Data Processing and Analysis Consortium (DPAC, <https://www.cosmos.esa.int/web/gaia/dpac/consortium>). Funding for the DPAC has been provided by national institutions, in particular the institutions participating in the Gaia Multilateral Agreement. The LCO measurements of radial velocities of stars were carried out with telescopes at McDonald Observatory in the USA, South African Astronomical Observatory (SAAO) in South Africa, and WISE Observatory in Israel. The Speckle observations reported were acquired at the Observatorio Astronómico Nacional in the Sierra San Pedro Martir (OAN-SPM), Baja California, México. We thank the daytime and night support staff at the OAN-SPM for facilitating and helping obtain our observations. The MAROON-X observations were supported by K-GMT Science Program (PID: GN-2024B-Q-122) of Korea Astronomy and Space Science Institute (KASI).

#### REFERENCES

Anders, F., Khalatyan, A., Queiroz, A. B. A., et al. 2022, *A&A*, 658, A91, doi: [10.1051/0004-6361/202142369](https://doi.org/10.1051/0004-6361/202142369)

Andrae, R., Fouesneau, M., Sordo, R., et al. 2023, *A&A*, 674, A27, doi: [10.1051/0004-6361/202243462](https://doi.org/10.1051/0004-6361/202243462)

Andrews, J. J., Anguiano, B., Chanamé, J., et al. 2019, *ApJ*, 871, 42, doi: [10.3847/1538-4357/aaf502](https://doi.org/10.3847/1538-4357/aaf502)

Banik, I., & Zhao, H. 2018, *MNRAS*, 480, 2660, doi: [10.1093/mnras/sty2007](https://doi.org/10.1093/mnras/sty2007)

Banik, I., & Zhao, H. 2022, *Symmetry*, 14, 1331, doi: [10.3390/sym14071331](https://doi.org/10.3390/sym14071331)

Bekenstein, J., & Milgrom, M. 1984, *ApJ*, 286, 7, doi: [10.1086/162570](https://doi.org/10.1086/162570)

Belokurov, V., Penoyre, Z., Oh, S., et al. 2020, *MNRAS*, 496, 1922, doi: [10.1093/mnras/staa1522](https://doi.org/10.1093/mnras/staa1522)

Billard, J., Boulay, M., Cebrián, S., et al. 2022, *Reports on Progress in Physics*, 85, 056201, doi: [10.1088/1361-6633/ac5754](https://doi.org/10.1088/1361-6633/ac5754)

Brandt, T. D. 2018, *ApJS*, 239, 31, doi: [10.3847/1538-4365/aaec06](https://doi.org/10.3847/1538-4365/aaec06)

Brown, T. M., Baliber, N., Bianco, F. B., et al. 2013, *PASP*, 125, 1031, doi: [10.1086/673168](https://doi.org/10.1086/673168)

Carlin, N., Cho, J. Y., Choi, J. J., et al. 2025, *Science Advances*, 11, eadv6503, doi: [10.1126/sciadv.adv6503](https://doi.org/10.1126/sciadv.adv6503)

Castro-Ginard, A., Penoyre, Z., Casey, A. R., et al. 2024, *A&A*, 688, A1, doi: [10.1051/0004-6361/202450172](https://doi.org/10.1051/0004-6361/202450172)

Chae, K.-H. 2023, *ApJ*, 952, 128, doi: [10.3847/1538-4357/ace101](https://doi.org/10.3847/1538-4357/ace101)

Chae, K.-H. 2024a, *ApJ*, 960, 114, doi: [10.3847/1538-4357/ad0ed5](https://doi.org/10.3847/1538-4357/ad0ed5)

Chae, K.-H. 2024b, *ApJ*, 972, 186, doi: [10.3847/1538-4357/ad61e9](https://doi.org/10.3847/1538-4357/ad61e9)

Chae, K.-H. 2025a, *ApJ*, 985, 210, doi: [10.3847/1538-4357/adce09](https://doi.org/10.3847/1538-4357/adce09)

Chae, K.-H. 2025b, arXiv e-prints, arXiv:2508.11996, doi: [10.48550/arXiv.2508.11996](https://doi.org/10.48550/arXiv.2508.11996)

Chae, K.-H. 2025c, Zenodo, doi: [10.5281/zenodo.17113129](https://doi.org/10.5281/zenodo.17113129)

Chae, K.-H., & Milgrom, M. 2022, *ApJ*, 928, 24, doi: [10.3847/1538-4357/ac5405](https://doi.org/10.3847/1538-4357/ac5405)

Einstein, A. 1916, *Annalen der Physik*, 354, 769, doi: [10.1002/andp.19163540702](https://doi.org/10.1002/andp.19163540702)

Eker, Z., Soydugan, F., Soydugan, E., et al. 2015, *AJ*, 149, 131, doi: [10.1088/0004-6256/149/4/131](https://doi.org/10.1088/0004-6256/149/4/131)

El-Badry, K., Rix, H.-W., & Heintz, T. M. 2021, *MNRAS*, 506, 2269, doi: [10.1093/mnras/stab323](https://doi.org/10.1093/mnras/stab323)

Famaey, B., & McGaugh, S. S. 2012, *Living Reviews in Relativity*, 15, 10, doi: [10.12942/lrr-2012-10](https://doi.org/10.12942/lrr-2012-10)

Fouesneau, M., Frémat, Y., Andrae, R., et al. 2023, *A&A*, 674, A28, doi: [10.1051/0004-6361/202243919](https://doi.org/10.1051/0004-6361/202243919)

Hawkins, K., Lucey, M., Ting, Y.-S., et al. 2020, *MNRAS*, 492, 1164, doi: [10.1093/mnras/stz3132](https://doi.org/10.1093/mnras/stz3132)

Hernandez, X. 2023, *MNRAS*, 525, 1401, doi: [10.1093/mnras/stad2306](https://doi.org/10.1093/mnras/stad2306)

Hernandez, X., Chae, K.-H., & Aguayo-Ortiz, A. 2024a, *MNRAS*, 533, 729, doi: [10.1093/mnras/stae1823](https://doi.org/10.1093/mnras/stae1823)

Hernandez, X., Jiménez, M. A., & Allen, C. 2012, *European Physical Journal C*, 72, 1884, doi: [10.1140/epjc/s10052-012-1884-6](https://doi.org/10.1140/epjc/s10052-012-1884-6)

Hernandez, X., & Kroupa, P. 2025, *MNRAS*, 537, 2925, doi: [10.1093/mnras/staf210](https://doi.org/10.1093/mnras/staf210)

Hernandez, X., Verteletskyi, V., Nasser, L., & Aguayo-Ortiz, A. 2024b, *MNRAS*, 528, 4720, doi: [10.1093/mnras/stad3446](https://doi.org/10.1093/mnras/stad3446)

Hill, T. P., & Miller, J. 2011, *Chaos*, 21, 033102, doi: [10.1063/1.3593373](https://doi.org/10.1063/1.3593373)

Husser, T. O., Wende-von Berg, S., Dreizler, S., et al. 2013, *A&A*, 553, A6, doi: [10.1051/0004-6361/201219058](https://doi.org/10.1051/0004-6361/201219058)

Hwang, H.-C., Ting, Y.-S., & Zakamska, N. L. 2022, *MNRAS*, 512, 3383, doi: [10.1093/mnras/stac675](https://doi.org/10.1093/mnras/stac675)

Kerp, J., Barth, W., Hofmann, K., Reinheimer, T., & Weigelt, G. 1992, in *ESO Conference on High-Resolution Imaging by Interferometry II*, ed. J. M. Beckers, & F. Merkle, Vol. 1, 269–278

Kouwenhoven, M. B. N., Goodwin, S. P., Parker, R. J., et al. 2010, *MNRAS*, 404, 1835, doi: [10.1111/j.1365-2966.2010.16399.x](https://doi.org/10.1111/j.1365-2966.2010.16399.x)

Kraus, A. L., Ireland, M. J., Martinache, F., & Hillenbrand, L. A. 2011, *ApJ*, 731, 8, doi: [10.1088/0004-637X/731/1/8](https://doi.org/10.1088/0004-637X/731/1/8)

Labeyrie, A. 1970, *A&A*, 6, 85

Lim, D., Koch-Hansen, A. J., Hong, S., Chun, S.-H., & Lee, Y.-W. 2024, *AJ*, 167, 3, doi: [10.3847/1538-3881/ad0a62](https://doi.org/10.3847/1538-3881/ad0a62)

Luna, A., & Orlov, V. G. 2020, *AJ*, 160, 9, doi: [10.3847/1538-3881/ab9120](https://doi.org/10.3847/1538-3881/ab9120)

Manchanda, D., Sutherland, W., & Pittordis, C. 2023, *The Open Journal of Astrophysics*, 6, E2, doi: [10.21105/astro.2210.07781](https://doi.org/10.21105/astro.2210.07781)

McCarthy, Jr., D. W., & Cobb, M. L. 1986, in *Society of Photo-Optical Instrumentation Engineers (SPIE) Conference Series*, Vol. 627, *Instrumentation in astronomy VI*, ed. D. L. Crawford, 797–804, doi: [10.1117/12.968161](https://doi.org/10.1117/12.968161)

McCully, C., Volgenau, N. H., Harbeck, D.-R., et al. 2018, in *Society of Photo-Optical Instrumentation Engineers (SPIE) Conference Series*, Vol. 10707, *Software and Cyberinfrastructure for Astronomy V*, ed. J. C. Guzman & J. Ibsen, 107070K, doi: [10.1117/12.2314340](https://doi.org/10.1117/12.2314340)

Merritt, D. 2020, *A Philosophical Approach to MOND: Assessing the Milgromian Research Program in Cosmology*

Milgrom, M. 1983, *ApJ*, 270, 365, doi: [10.1086/161130](https://doi.org/10.1086/161130)

Milgrom, M. 2010, *MNRAS*, 403, 886, doi: [10.1111/j.1365-2966.2009.16184.x](https://doi.org/10.1111/j.1365-2966.2009.16184.x)

Moeckel, N., & Clarke, C. J. 2011, *MNRAS*, 415, 1179, doi: [10.1111/j.1365-2966.2011.18731.x](https://doi.org/10.1111/j.1365-2966.2011.18731.x)

Navas, S., Amsler, C., Gutsche, T., et al. 2024, *PhRvD*, 110, 030001, doi: [10.1103/PhysRevD.110.030001](https://doi.org/10.1103/PhysRevD.110.030001)

Nelson, T., Ting, Y.-S., Hawkins, K., et al. 2021, *ApJ*, 921, 118, doi: [10.3847/1538-4357/ac14be](https://doi.org/10.3847/1538-4357/ac14be)

Orlov, V. G. 2021, *RMxAA*, 57, 67, doi: [10.22201/ia.01851101p.2021.57.01.04](https://doi.org/10.22201/ia.01851101p.2021.57.01.04)

Pflamm-Altenburg, J. 2025, *arXiv e-prints*, arXiv:2509.01493, doi: [10.48550/arXiv.2509.01493](https://doi.org/10.48550/arXiv.2509.01493)

Pittordis, C., & Sutherland, W. 2018, *MNRAS*, 480, 1778, doi: [10.1093/mnras/sty1578](https://doi.org/10.1093/mnras/sty1578)

Pittordis, C., Sutherland, W., & Shepherd, P. 2025, *The Open Journal of Astrophysics*, 8, 109, doi: [10.33232/001c.142887](https://doi.org/10.33232/001c.142887)

Read, J. I. 2014, *Journal of Physics G Nuclear Physics*, 41, 063101, doi: [10.1088/0954-3899/41/6/063101](https://doi.org/10.1088/0954-3899/41/6/063101)

Reipurth, B., & Mikkola, S. 2012, *Nature*, 492, 221, doi: [10.1038/nature11662](https://doi.org/10.1038/nature11662)

Rozner, M., & Perets, H. B. 2023, *ApJ*, 955, 134, doi: [10.3847/1538-4357/ace2c6](https://doi.org/10.3847/1538-4357/ace2c6)

Saglia, R., Pasquini, L., Patat, F., et al. 2025, *A&A*, 699, A151, doi: [10.1051/0004-6361/202555115](https://doi.org/10.1051/0004-6361/202555115)

Sanders, R. H., & McGaugh, S. S. 2002, *ARA&A*, 40, 263, doi: [10.1146/annurev.astro.40.060401.093923](https://doi.org/10.1146/annurev.astro.40.060401.093923)

Scarpa, R., Ottolina, R., Falomo, R., & Treves, A. 2017, *International Journal of Modern Physics D*, 26, 1750067, doi: [10.1142/S0218271817500675](https://doi.org/10.1142/S0218271817500675)

Seifahrt, A., Stürmer, J., Bean, J. L., & Schwab, C. 2018, in *Society of Photo-Optical Instrumentation Engineers (SPIE) Conference Series*, Vol. 10702, *Ground-based and Airborne Instrumentation for Astronomy VII*, ed. C. J. Evans, L. Simard, & H. Takami, 107026D, doi: [10.1117/12.2312936](https://doi.org/10.1117/12.2312936)

Shaya, E. J., & Olling, R. P. 2011, *ApJS*, 192, 2, doi: [10.1088/0067-0049/192/1/2](https://doi.org/10.1088/0067-0049/192/1/2)

Siverd, R. J., Brown, T. M., Barnes, S., et al. 2018, in Society of Photo-Optical Instrumentation Engineers (SPIE) Conference Series, Vol. 10702, Ground-based and Airborne Instrumentation for Astronomy VII, ed. C. J. Evans, L. Simard, & H. Takami, 107026C, doi: [10.1117/12.2312800](https://doi.org/10.1117/12.2312800)

Tokovinin, A. 2017, *MNRAS*, 468, 3461, doi: [10.1093/mnras/stx707](https://doi.org/10.1093/mnras/stx707)

Tokovinin, A., Mason, B. D., & Hartkopf, W. I. 2010, *The Astronomical Journal*, 139, 743, doi: [10.1088/0004-6256/139/2/743](https://doi.org/10.1088/0004-6256/139/2/743)

Vallenari, A., Brown, A. G. A., Prusti, T., et al. 2023, *A&A*, 674, A1, doi: [10.1051/0004-6361/202243940](https://doi.org/10.1051/0004-6361/202243940)

Vorobyov, E. I. 2013, *A&A*, 552, A129, doi: [10.1051/0004-6361/201220601](https://doi.org/10.1051/0004-6361/201220601)

Xu, S., Hwang, H.-C., Hamilton, C., & Lai, D. 2023, *ApJL*, 949, L28, doi: [10.3847/2041-8213/acd6f7](https://doi.org/10.3847/2041-8213/acd6f7)

Yoon, Y., Tian, Y., & Chae, K.-H. 2025, *ApJ*, 992, 102, doi: [10.3847/1538-4357/ae0190](https://doi.org/10.3847/1538-4357/ae0190)

## APPENDIX

## A. DESCRIPTION OF LCO OBSERVATIONS AND DATA REDUCTION OF RADIAL VELOCITIES

A sample of 60 wide binaries were selected from the [K. El-Badry et al. \(2021\)](#) catalog with the following requirements: (1) Both stars of a binary are brighter than  $G = 11$  mag and are in the absolute magnitude range  $3 \lesssim M_G < 8$ , (2) the sky-plane separation  $s > 3.5$  kau, and (3) the relative Gaia DR3 RV satisfies

$$|v_r| \equiv |\text{RV}_A - \text{RV}_B| < \sqrt{9(\sigma_A^2 + \sigma_B^2) + (\Delta V)^2} \quad (\text{A1})$$

where  $\Delta V = 0.9419\sqrt{M_{\text{tot}}/s} \times 1.3 \times 1.2 \text{ km s}^{-1}$  for the binary total mass  $M_{\text{tot}}$  given in  $M_{\odot}$  and the sky-plane separation  $s$  given in kau. This threshold is slightly relaxed from that given by Equations (2) and (3) of [K.-H. Chae \(2024a\)](#). We note that we impose only a requirement on the relative RV because the [K. El-Badry et al. \(2021\)](#) catalog was obtained with a requirement on the relative PM.

Spectroscopic observations were made from December 2024 to March 2025 using the fiber-fed high-resolution Las Cumbres Observatory (LCO; [T. M. Brown et al. 2013](#)) Network of Robotic Echelle Spectrographs (NRES; [R. J. Siverd et al. 2018](#)) attached to telescopes at McDonald Observatory, South African Astronomical Observatory (SAAO), South Africa, and WISE Observatory, Israel. The spectrograph provides a spectral resolution of 53,000 and covers a wavelength range of 3800 – 8600 Å. The exposure time of the observations was adjusted between 600 and 1800 seconds, depending on the brightness of the target. To prevent spectral line blending due to star rotation and maintain precision, the maximum exposure time was limited to 1800 seconds. The signal-to-noise ratio (SNR) in LCO/NRES is typically estimated per resolution element within the spectral order that includes the Mg b lines (5167 – 5184 Å). The SNRs of the observed targets ranged from approximately 15 to 100. An SNR of at least 25 is recommended to obtain accurate radial velocity (RV) measurements; however, achieving this level is challenging for targets with  $V > 10$ .

The data extracted from the LCO archive were bias and flat-field corrected images processed with the BANZAI pipeline ([C. McCully et al. 2018](#)). BANZAI-NRES is designed to handle all data from the NRES of the LCO network. Stellar RVs in LCO/NRES are estimated by comparing the BLAZ-extracted spectrum with a corresponding ZERO file, derived from PHOENIX stellar models ([T. O. Husser et al. 2013](#)). Each target star is assigned a specific ZERO file to ensure consistency. The pipeline first determines an initial redshift by cross-correlating the BLAZ and ZERO spectra. It then interpolates the ZERO spectrum to this redshift and divides each spectral order into wavelength segments. The residual redshift for each segment is then estimated along with formal errors. Finally, multiple estimates of the mean redshift are computed using different averaging methods.

The BANZAI-NRES pipeline provides extracted and wavelength-corrected spectra. If the target is a star, the pipeline also delivers RV measurements and stellar classification parameters, such as effective temperature and surface gravity. The RV precision of the BANZAI-NRES pipeline has been demonstrated to be as good as  $10 \text{ m s}^{-1}$  for bright ( $V \approx 6$ ) standard stars. For this study, we used the cross-correlation function (CCF) implemented in the pipeline, with approximate errors of  $71 \text{ m s}^{-1}$  for the entire sample. A summary of the observations can be found in Table 4.

**Table 4. Summary of Wide Binaries Observed with LCO/NRES**

ID	Name	Gaia DR3 identifier	Sep <sup>a</sup> [kau]	Mass <sup>b</sup> [ $M_{\odot}$ ]	Spec Type <sup>c</sup>	RV(DR3) <sup>d</sup> [ $\text{km s}^{-1}$ ]	RV(LCO) <sup>e</sup> [ $\text{km s}^{-1}$ ]	$v_r$ (LCO) <sup>f</sup> [ $\text{km s}^{-1}$ ]	site <sup>g</sup>
1A	BD+65 14	528186492427483392	5.246	1.18	F6V	$7.967 \pm 0.261$	$8.116 \pm 0.064$	$-0.652 \pm 0.087$	(1)
1B	BD+65 12	528187248343141376		1	G1V	$8.442 \pm 0.342$	$8.768 \pm 0.059$		(1)
2A	HD 236377	428811394564909568	5.063	1.2	F8	$-66.402 \pm 0.234$	$-66.074 \pm 0.037$	$-0.647 \pm 0.149$	(1)
2B	BD+59 32B	428811428924644352		0.85	G0	$-65.447 \pm 0.245$	$-65.427 \pm 0.144$		(1)
3A	BD-09 71	2426718786382002304	9.547	0.97		$-14.245 \pm 0.570$	$-13.311 \pm 0.084$	$-0.772 \pm 0.142$	(1)
3B	TYC 5262-512-1	2426718614583009280		0.99		$-13.280 \pm 0.487$	$-12.539 \pm 0.115$		(2)
4A	HD 4552	2776055105362407680	4.839	1.2	F8	$14.913 \pm 0.236$	$14.957 \pm 0.140$	$-0.605 \pm 0.150$	(3)
4B	BD+12 90	2776054899203977728		1.0	G0	$15.509 \pm 0.161$	$15.562 \pm 0.054$		(3)
5A	BD-03 107	2529661799483080192	5.373	1.13	F6V	$-12.528 \pm 0.274$	$-12.456 \pm 0.100$	$-0.560 \pm 0.109$	(3)
5B	TYC 4674-49-1	2529474126591876096		0.83	G6V	$-12.306 \pm 0.303$	$-11.896 \pm 0.044$		(1)
6A	HD 8745	322414398818886656	13.951	1.16	F8	$-8.390 \pm 0.130$	$-7.901 \pm 0.039$	$-0.423 \pm 0.062$	(1),(1)
6B	BD+36 251	322413681559182720		0.86	K0	$-8.050 \pm 0.173$	$-7.478 \pm 0.048$		(1),(1)

**Table 4** *continued*

Table 4 (continued)

7A	HD 9769	5038962632187714432	10.152	1.33	F5V	31.107 $\pm$ 0.144	31.413 $\pm$ 0.054	0.212 $\pm$ 0.088	(2)
7B	CD-24 668	5038962219872444160		1.09		30.965 $\pm$ 0.220	31.201 $\pm$ 0.069		(2)
8A	HD 11584	4940794866807373952	4.933	1.18	F6/8V	22.731 $\pm$ 0.145	22.773 $\pm$ 0.038	0.387 $\pm$ 0.069	(2),(2)
8B	CD-50 524	4940794488850252928		1.15		22.377 $\pm$ 0.159	22.386 $\pm$ 0.058		(3),(3)
9A	HD 18014	5185524920830592128	4.044	0.74	K4V	38.489 $\pm$ 0.141	38.950 $\pm$ 0.051	0.276 $\pm$ 0.086	(2)
9B	BD-04 488	5185536774940328448		0.7	K5V	38.386 $\pm$ 0.267	38.674 $\pm$ 0.069		(1)
10A	BD-12 743	5114547700047886976	3.670	0.91		86.111 $\pm$ 0.204	86.371 $\pm$ 0.046	-0.392 $\pm$ 0.112	(3)
10B	TYC 5307-1283-1	5114544745110388352		0.82		86.370 $\pm$ 0.229	86.763 $\pm$ 0.102		(2)
11A	HD 24820	3193531802050857472	10.787	1.24	F6V	1.067 $\pm$ 0.211	1.821 $\pm$ 0.222	0.715 $\pm$ 0.228	(2)
11B	BD-10 790	3193508059471646464		1.05		0.737 $\pm$ 0.195	1.106 $\pm$ 0.052		(2)
12A	HD 25384	5090701698022451200	5.449	1.31	F5V	5.975 $\pm$ 0.173	5.915 $\pm$ 0.097	0.072 $\pm$ 0.161	(2)
12B	TYC 5888-565-1	5090701698022451072		1.14		5.824 $\pm$ 0.238	5.843 $\pm$ 0.129		(2)
13A	HD 26440	3203601851092155776	22.891	1.07	G3V	24.222 $\pm$ 0.175	24.604 $\pm$ 0.088	-0.361 $\pm$ 0.200	(3)
13B	TYC 4729-523-1	3203683695989446400		0.95		24.626 $\pm$ 0.225	24.965 $\pm$ 0.180		(3)
14A	BD+05 650	3285755951169814656	26.874	1.12	G0	23.149 $\pm$ 0.225	23.765 $\pm$ 0.105	0.050 $\pm$ 0.120	(3)
14B	BD+05 653	3285744612456149888		1.05	G2	23.260 $\pm$ 0.307	23.715 $\pm$ 0.058		(3)
15A	HD 29356	3230677565443833088	4.972	1.16	F7/G0	38.397 $\pm$ 0.135	38.989 $\pm$ 0.042	-0.076 $\pm$ 0.057	(3),(3)
15B	HD 29355	3230677874682668672		1.15	F3/6	38.724 $\pm$ 0.133	39.065 $\pm$ 0.038		(3),(3)
16A	zeta Dor	4763906879239461632	3.760	1.09	F9VFe-0.5	-1.450 $\pm$ 0.125	-0.976 $\pm$ 0.102	-0.581 $\pm$ 0.123	(2),(2)
16B	CD-57 1079	4763897739549071744		0.57	K7V <sub>k</sub>	-1.135 $\pm$ 0.130	-0.395 $\pm$ 0.068		(3),(3)
17A	HD 35376	4763357363943383808	5.022	0.95	G3/5V	17.604 $\pm$ 0.152	17.985 $\pm$ 0.018	-0.283 $\pm$ 0.092	(2)
17B	CD-57 1160	4763357260864168320		0.82		17.798 $\pm$ 0.231	18.268 $\pm$ 0.090		(3)
18A	HD 247101	3445112363273415808	25.589	1.3		-1.655 $\pm$ 0.277	-1.822 $\pm$ 0.060	-0.147 $\pm$ 0.077	(1)
18B	HD 247123	3445112122755273472		1.14		-2.167 $\pm$ 0.195	-1.675 $\pm$ 0.049		(1)
19A	CD-22 2824	2913801715936708352	22.722	1.23	F5	-14.846 $\pm$ 0.191	-14.501 $\pm$ 0.210	-0.232 $\pm$ 0.221	(2)
19B	TYC 5945-1833-1	2913814119802247296		0.99		-14.241 $\pm$ 0.254	-14.269 $\pm$ 0.070		(3)
20A	HD 48540	2925423072806388608	22.211	1.3	F3V	1.764 $\pm$ 0.141	1.768 $\pm$ 0.121	-0.226 $\pm$ 0.132	(2)
20B	TYC 6521-2073-1	2925423931801365760		1.09		1.558 $\pm$ 0.234	1.994 $\pm$ 0.054		(2)
21A	HD 49496	1003223614961194752	4.710	1.01	G0V	-23.958 $\pm$ 0.226	-23.738 $\pm$ 0.042	-0.430 $\pm$ 0.077	(1)
21B	TYC 3778-1205-1	1003223584897948160		0.87	K2V	-23.903 $\pm$ 0.220	-23.308 $\pm$ 0.065		(1)
22A	TYC 752-1389-1	3158926322836178816	10.968	0.77		-17.510 $\pm$ 0.429	-16.958 $\pm$ 0.058	0.023 $\pm$ 0.066	(2)
22B	TYC 752-1649-1	3158878734598549376		0.89	NaN	-17.575 $\pm$ 0.427	-16.981 $\pm$ 0.032		(2)
23A	HD 51943	2932313231147240960	9.840	1.28	F5/6V	-17.921 $\pm$ 0.157	-17.739 $\pm$ 0.077	-0.073 $\pm$ 0.085	(2)
23B	CPD-19 1595	2932313196787509376		1.11	F6V	-17.943 $\pm$ 0.169	-17.666 $\pm$ 0.037		(2)
24A	HD 53566	3116331104937277952	30.340	1.26	F3/5V	-15.010 $\pm$ 0.140	-14.859 $\pm$ 0.046	-0.345 $\pm$ 0.060	(2),(2)
24B	TYC 170-2913-1	3116324881524878208		0.84	F9	-14.830 $\pm$ 0.201	-14.514 $\pm$ 0.039		(2),(2)
25A	TYC 5389-255-1	3046204180298475264	6.127	0.80	G7V	59.201 $\pm$ 0.356	59.393 $\pm$ 0.075	-0.413 $\pm$ 0.131	(2)
25B	TYC 5389-869-1	3046204150242468480		0.80	G9V	59.243 $\pm$ 0.375	59.806 $\pm$ 0.108		(2)
26A	BD+82 192	1142787168495168000	3.772	0.80	G5	11.756 $\pm$ 0.218	11.980 $\pm$ 0.054	-0.317 $\pm$ 0.075	(1)
26B	BD+82 193	1142786996696476288		0.74	G5	11.858 $\pm$ 0.272	12.297 $\pm$ 0.052		(1)
27A	TYC 1364-1623-1	3170300942420466176	9.723	1.04		-27.738 $\pm$ 0.243	-26.993 $\pm$ 0.038	-0.055 $\pm$ 0.058	(1),(2)
27B	TYC 1364-1760-1	3170394607068638336		1.01		-26.989 $\pm$ 0.207	-26.938 $\pm$ 0.044		(2),(2)
28A	HD 71050	914241517609344128	19.612	1.16	G0	-3.634 $\pm$ 0.339	-3.251 $\pm$ 0.107	0.133 $\pm$ 0.123	(1)
28B	HD 70986	914244399532441472		1.11	G5	-3.636 $\pm$ 0.322	-3.384 $\pm$ 0.061		(1)
29A	HD 72584	5755402720924702464	7.910	1.11	F6V	12.566 $\pm$ 0.259	12.674 $\pm$ 0.049	-0.196 $\pm$ 0.127	(1),(3)
29B	TYC 4874-1253-1	5755402484702384128		0.79	G3	12.516 $\pm$ 0.206	12.869 $\pm$ 0.117		(3),(3)
30A	HD 78796	5651775953326498688	7.518	0.96	G5V	-3.741 $\pm$ 0.150	-3.314 $\pm$ 0.042	-0.119 $\pm$ 0.081	(2),(3)
30B	CD-23 8096	5651752515687994368		0.8	K0	-3.872 $\pm$ 0.194	-3.195 $\pm$ 0.069		(3),(1)
31A	HD 81268	5741345125461459200	13.101	1.04	G0V	14.433 $\pm$ 0.174	14.853 $\pm$ 0.024	-0.327 $\pm$ 0.042	(1),(3)
31B	BD-08 2665	5741344919302959360		0.97	G0	15.064 $\pm$ 0.185	15.180 $\pm$ 0.034		(1),(2)
32A	HD 85137	5305981470567619456	6.524	1.14	F7V	3.841 $\pm$ 0.167	3.917 $\pm$ 0.048	-0.337 $\pm$ 0.086	(2),(2)
32B	CD-57 2838	5305981745445719680		0.84		3.974 $\pm$ 0.195	4.254 $\pm$ 0.071		(3),(3)
33A	HD 88418	3861210890850859392	10.090	1.24	F8	-43.494 $\pm$ 0.205	-42.783 $\pm$ 0.085	-0.339 $\pm$ 0.111	(2),(2)
33B	TYC 251-458-1	3861210925210595072		0.88		-42.704 $\pm$ 0.238	-42.444 $\pm$ 0.071		(3),(1)

Table 4 continued

Table 4 (continued)

34A	TYC 6068-1392-1	5668676409117097984	5.728	1.13		14.247 $\pm$ 0.340	14.649 $\pm$ 0.074	-0.254 $\pm$ 0.139	(3)
34B	TYC 6068-1401-1	5668675653202854528		1.06		14.349 $\pm$ 0.333	14.903 $\pm$ 0.118		(2)
35A	HD 92677	3749791158495959552	4.181	0.92	G6/8(IV)	1.042 $\pm$ 0.172	1.408 $\pm$ 0.045	0.383 $\pm$ 0.073	(2),(2)
35B	HD 92652	3749791055416743552		0.9	G8/K1	0.642 $\pm$ 0.177	1.025 $\pm$ 0.057		(3),(3)
36A	HD 93528	3550081879381593728	7.870	0.82	K0V	23.759 $\pm$ 0.148	24.129 $\pm$ 0.044	-0.595 $\pm$ 0.082	(2)
36B	BD-21 3153	3550084490721711872		0.7	K4.5V $\kappa$	24.451 $\pm$ 0.180	24.724 $\pm$ 0.069		(2)
37A	HD 95532	3556353734223925504	7.777	1.27	F7/8V	-27.258 $\pm$ 0.134	-26.931 $\pm$ 0.040	-0.252 $\pm$ 0.080	(3)
37B	HD 95531	3556356070686135040		1.05	G2/3(V)	-27.093 $\pm$ 0.191	-26.679 $\pm$ 0.069		(3)
38A	HD 101574	3793107930900527616	16.371	1.22	F5V	-0.382 $\pm$ 0.166	0.826 $\pm$ 0.061	0.260 $\pm$ 0.094	(2),(1)
38B	BD-01 2557	3793106419072038272		1.03		0.367 $\pm$ 0.208	0.566 $\pm$ 0.072		(3),(3)
39A	HD 103231	3487243037508315648	10.721	1.12	G0V	-8.786 $\pm$ 0.135	-8.343 $\pm$ 0.052	0.170 $\pm$ 0.060	(2)
39B	HD 103206	3487237024554098560		0.98	G6V	-8.823 $\pm$ 0.167	-8.513 $\pm$ 0.030		(2)
40A	HD 233884	787833551986183168	4.547	1.07	K0	-5.034 $\pm$ 0.199	-4.746 $\pm$ 0.079	0.386 $\pm$ 0.088	(1)
40B	TYC 3454-370-1	787833483266126080		0.86		-5.199 $\pm$ 0.244	-5.132 $\pm$ 0.038		(1)
41A	HD 105350	6147940161728145536	22.167	0.98	G5V	28.584 $\pm$ 0.142	29.068 $\pm$ 0.061	-0.250 $\pm$ 0.109	(3),(3)
41B	TYC 7763-590-1	614793751602909728		0.74		28.704 $\pm$ 0.205	29.318 $\pm$ 0.090		(2),(2)
42A	HD 107434	6151377578674752896	11.180	1.15	F6V	-10.499 $\pm$ 0.129	-10.067 $\pm$ 0.080	-0.569 $\pm$ 0.108	(2),(2)
42B	CD-37 7822	6151049133934677248		0.8		-10.061 $\pm$ 0.192	-9.499 $\pm$ 0.073		(3),(3)
43A	BD+82 377	1719835231806217472	8.476	1.07	G0	-33.369 $\pm$ 0.277	-33.532 $\pm$ 0.038	-0.297 $\pm$ 0.060	(1)
43B	BD+82 376	1719835407900844544		1.05	G5	-33.177 $\pm$ 0.232	-33.235 $\pm$ 0.047		(1)
44A	HD 123033	1258410612976538368	4.273	1.2	F6V	-20.046 $\pm$ 0.121	-19.847 $\pm$ 0.066	-0.632 $\pm$ 0.082	(3),(1)
44B	BD+26 2522	1258410750415492864		0.87	K0	-19.854 $\pm$ 0.146	-19.215 $\pm$ 0.048		(1),(3)
45A	HD 124711	1482432155767129728	12.657	1.21		-2.591 $\pm$ 0.141	-2.090 $\pm$ 0.083	-0.068 $\pm$ 0.101	(1)
45B	BD+36 2455	1479430076707007488		0.93		-2.355 $\pm$ 0.195	-2.022 $\pm$ 0.058		(1)
46A	HD 127058	5899243585161684864	6.692	1.03	F8/G0V	3.428 $\pm$ 0.148	3.955 $\pm$ 0.032	-0.566 $\pm$ 0.056	(2)
46B	CD-49 8796	5899244375435693952		0.92	G5	4.332 $\pm$ 0.159	4.521 $\pm$ 0.046		(3)
47A	BD+08 2889	1172915990414659328	24.684	0.85	G5	-18.422 $\pm$ 0.248	-17.964 $\pm$ 0.029	-0.027 $\pm$ 0.077	(2),(3)
47B	BD+08 2887	1172920487244742912		0.8	K2	-18.415 $\pm$ 0.261	-17.937 $\pm$ 0.071		(3),(3)
48A	HD 129171	1282815063829295360	16.772	1.03	G0	-11.925 $\pm$ 0.121	-11.406 $\pm$ 0.026	-0.283 $\pm$ 0.041	(1),(1)
48B	HD 129209	1282817022334383232		1	G2IV	-11.598 $\pm$ 0.124	-11.123 $\pm$ 0.032		(1),(1)
49A	TYC 364-256-1	4430185068482324864	4.426	0.96		-34.756 $\pm$ 0.198	-34.665 $\pm$ 0.032	-0.025 $\pm$ 0.072	(3)
49B	TYC 364-158-1	4430185034123000960		0.99		-34.649 $\pm$ 0.192	-34.640 $\pm$ 0.064		(2)
50A	41 Her	4435689739087756800	7.159	1.12	G8	-6.595 $\pm$ 0.119	-6.124 $\pm$ 0.019	0.637 $\pm$ 0.097	(3)
50B	Ross 643	4435683451255623808		0.71	K3	-7.031 $\pm$ 0.165	-6.761 $\pm$ 0.095		(2)
51A	BD+27 2769	4574764697142222592	14.269	1.19	F5	-32.903 $\pm$ 0.184	-33.382 $\pm$ 0.250	-1.078 $\pm$ 0.266	(1)
51B	BD+27 2768	4574670895056352896		1.07	F8	-32.563 $\pm$ 0.162	-32.304 $\pm$ 0.092		(1)
52A	HD 158226	4599984642025088128	4.731	0.99	G1V	-73.239 $\pm$ 0.132	-72.809 $\pm$ 0.028	0.086 $\pm$ 0.062	(1)
52B	BD+31 3025	4599984504586131456		0.88	G8	-73.024 $\pm$ 0.234	-72.895 $\pm$ 0.055		(1)
53A	HD 352384	1815165535636339072	11.565	1.14	G0	51.028 $\pm$ 0.171	51.307 $\pm$ 0.026	-0.853 $\pm$ 0.047	(1)
53B	HD 352383	1815165883534980992		0.97	G0	51.103 $\pm$ 0.213	52.160 $\pm$ 0.039		(1)
54A	HD 201706	1760471948915107200	4.263	1.02	G0	14.790 $\pm$ 0.139	15.896 $\pm$ 0.027	0.947 $\pm$ 0.047	(1)
54B	BD+14 4553	1760477618271932672		0.81	G5	14.779 $\pm$ 0.160	14.949 $\pm$ 0.038		(1)
55A	BD+41 4134	1967283042361454848	6.695	1.04	G0	-24.763 $\pm$ 0.163	-24.385 $\pm$ 0.038	-0.561 $\pm$ 0.082	(1)
55B	BD+41 4133	1967282939282261120		0.84		-24.249 $\pm$ 0.171	-23.824 $\pm$ 0.073		(1)
56A	HD 207397	6840365718216434816	4.515	0.97	G3V	18.847 $\pm$ 0.195	19.153 $\pm$ 0.180	0.005 $\pm$ 0.185	(1)
56B	BD-14 6130	6840365615137220096		0.81		19.154 $\pm$ 0.264	19.148 $\pm$ 0.044		(1)
57A	HD 209032	6570796871887419648	3.952	0.96	K1(IVp)	18.897 $\pm$ 0.157	19.334 $\pm$ 0.018	0.105 $\pm$ 0.069	(2)
57B	TYC 8001-622-1	6570797524722448896		0.92		19.156 $\pm$ 0.146	19.229 $\pm$ 0.067		(3)
58A	TYC 4264-485-1	2201661297490051968	8.370	1.03		-12.734 $\pm$ 0.251	-12.514 $\pm$ 0.077	0.002 $\pm$ 0.110	(1)
58B	TYC 4264-252-1	2201661091331626752		1.04		-12.387 $\pm$ 0.268	-12.516 $\pm$ 0.079		(1)
59A	HD 220721	1938247517245907456	11.055	1.05	G0	-15.506 $\pm$ 0.125	-15.045 $\pm$ 0.029	-0.055 $\pm$ 0.046	(1)
59B	HD 220748	1938247654684985216		0.97	G5	-15.439 $\pm$ 0.139	-14.990 $\pm$ 0.036		(1)
60A	HD 224478	2739496687336985984	7.122	1.13	F6V	14.919 $\pm$ 0.340	16.068 $\pm$ 0.300	0.716 $\pm$ 0.344	(1)
60B	AG+02 2992	2739498199165473920		1.01	G	15.254 $\pm$ 0.324	15.352 $\pm$ 0.168		(1)

Table 4 continued

**Table 4** (*continued*)

<sup>a</sup> 2D separation: Sky-plane physical separation from K. El-Badry et al. (2021).

<sup>b</sup> Mass: Stellar masses, along with their  $1\sigma$  uncertainties, were retrieved from the Gaia DR3 StarHorse catalog using ADQL queries. *Mass*: The stellar masses estimate corresponds to the median (50th percentile) value from the Gaia EDR3 StarHorse catalog, following the photo-astrometric methodology described by F. Anders et al. (2022).

<sup>c</sup> Spectral Type: Spectral classifications adopted from SIMBAD.

<sup>d</sup> RV DR3: Radial velocity from Gaia DR3.

<sup>e</sup> RV LCO: Radial velocity measured with NRES at LCO.

<sup>f</sup>  $v_r (\equiv RV_A - RV_B)$  LCO: Radial velocity difference between the binary components, as measured with LCO/NRES.

<sup>g</sup> Site: Observational site, listed in chronological order — (1) McDonald Observatory; (2) South African Astronomical Observatory (SAAO); (3) WISE Observatory, Israel.

### A.1. Systems that were observed more than once with LCO

Eighteen of the 60 binary systems were observed more than once. Their respective properties are listed below.

6A (HD 8745) was observed twice at McDonald Observatory. RVs of  $-7.955 \pm 0.040 \text{ km s}^{-1}$  and  $-7.846 \pm 0.037 \text{ km s}^{-1}$  were measured on 2024 December 14 (BJD 2460659.703) and 2025 February 9 (BJD 2460716.58759), respectively. The mean RV is  $-7.901 \pm 0.039 \text{ km s}^{-1}$ . 6B (BD+36 251) was observed twice at McDonald Observatory. RVs of  $-7.545 \pm 0.031 \text{ km s}^{-1}$  and  $-7.411 \pm 0.056 \text{ km s}^{-1}$  were measured on 2024 December 14 (BJD 2460659.764) and 2025 February 9 (BJD 2460716.6159), respectively. The mean RV is  $-7.478 \pm 0.048 \text{ km s}^{-1}$ .

8A (HD 11584) was observed twice at the South African Astronomical Observatory (SAAO). RVs of  $22.761 \pm 0.030 \text{ km s}^{-1}$  and  $22.784 \pm 0.044 \text{ km s}^{-1}$  were measured on 2024 December 14 (BJD 2460659.437) and 2025 February 11 (BJD 2460718.29242), respectively. The mean RV is  $22.773 \pm 0.038 \text{ km s}^{-1}$ . 8B (CD-50 524) was observed twice at the WISE Observatory. RVs of  $22.398 \pm 0.056 \text{ km s}^{-1}$  and  $22.374 \pm 0.060 \text{ km s}^{-1}$  were measured on 2024 December 18 (BJD 2460663.566) and 2025 February 17 (BJD 2460724.5223), respectively. The mean RV is  $22.386 \pm 0.058 \text{ km s}^{-1}$ .

15A (HD 29356) was observed twice at the WISE Observatory. RVs of  $38.938 \pm 0.050 \text{ km s}^{-1}$  and  $39.039 \pm 0.030 \text{ km s}^{-1}$  were measured on 2025 January 8 (BJD 2460684.54458) and 2025 February 9 (BJD 2460716.5881), respectively. The mean RV is  $38.989 \pm 0.042 \text{ km s}^{-1}$ . 15B (HD 29355) was observed twice at the WISE Observatory. RVs of  $39.036 \pm 0.033 \text{ km s}^{-1}$  and  $39.093 \pm 0.043 \text{ km s}^{-1}$  were measured on 2025 January 7 (BJD 2460683.71539) and 2025 February 7 (BJD 2460714.62182), respectively. The mean RV is  $39.065 \pm 0.038 \text{ km s}^{-1}$ .

16A ( $\zeta$  Dor) was observed twice at SAAO. RVs of  $-0.966 \pm 0.103 \text{ km s}^{-1}$  and  $-0.985 \pm 0.100 \text{ km s}^{-1}$  were measured on 2024 December 14 (BJD 2460659.584) and 2025 February 28 (BJD 2460735.37616), respectively. The mean RV is  $-0.976 \pm 0.102 \text{ km s}^{-1}$ . 16B (CD-57 1079) was observed twice at the WISE Observatory. RVs of  $-0.185 \pm 0.074 \text{ km s}^{-1}$  and  $-0.605 \pm 0.061 \text{ km s}^{-1}$  were measured on 2024 December 18 (BJD 2460663.73559) and 2025 March 4 (BJD 2460739.55929), respectively. The mean RV is  $-0.395 \pm 0.068 \text{ km s}^{-1}$ .

24A (HD 53566) was observed twice at SAAO. RVs of  $-14.822 \pm 0.045 \text{ km s}^{-1}$  and  $-14.896 \pm 0.047 \text{ km s}^{-1}$  were measured on 2025 January 10 (BJD 2460686.47896) and 2025 February 12 (BJD 2460719.37888), respectively. The mean RV is  $-14.859 \pm 0.046 \text{ km s}^{-1}$ . 24B (TYC 170-2913-1) was observed twice at SAAO. RVs of  $-14.510 \pm 0.024 \text{ km s}^{-1}$  and  $-14.519 \pm 0.049 \text{ km s}^{-1}$  were measured on 2025 January 7 (BJD 2460683.4967) and 2025 February 14 (BJD 2460721.37678), respectively. The mean RV is  $-14.515 \pm 0.039 \text{ km s}^{-1}$ .

27A (TYC 1364-1623-1) was observed twice, at SAAO and McDonald Observatory, respectively. RVs of  $-27.039 \pm 0.026 \text{ km s}^{-1}$  and  $-26.946 \pm 0.047 \text{ km s}^{-1}$  were measured on 2024 December 19 (BJD 2460664.47497) and 2025 February 16 (BJD 2460723.81325), respectively. The mean RV is  $-26.993 \pm 0.038 \text{ km s}^{-1}$ . 27B (TYC 1364-1760-1) was observed twice at SAAO. RVs of  $-26.961 \pm 0.039 \text{ km s}^{-1}$  and  $-26.916 \pm 0.049 \text{ km s}^{-1}$  were measured on 2024 December 19 (BJD 2460664.47497) and 2025 February 14 (BJD 2460721.35215), respectively. The mean RV

is  $-26.939 \pm 0.044 \text{ km s}^{-1}$ .

29A (HD 72584) was observed twice, at McDonald Observatory and WISE Observatory, respectively. RVs of  $12.749 \pm 0.043 \text{ km s}^{-1}$  and  $12.599 \pm 0.055 \text{ km s}^{-1}$  were measured on 2024 December 14 (BJD 2460659.941) and 2025 March 3 (BJD 2460738.70737), respectively. The mean RV is  $12.674 \pm 0.049 \text{ km s}^{-1}$ . 29B (TYC 4874-1253-1) was observed twice at WISE Observatory. RVs of  $12.854 \pm 0.077 \text{ km s}^{-1}$  and  $12.885 \pm 0.146 \text{ km s}^{-1}$  were measured on 2024 December 15 (BJD 2460660.700) and 2025 March 2 (BJD 2460737.69814), respectively. The mean RV is  $12.870 \pm 0.117 \text{ km s}^{-1}$ .

30A (HD 78796) was observed twice at WISE Observatory and SAAO, respectively. RVs of  $-3.313 \pm 0.047 \text{ km s}^{-1}$  and  $-3.316 \pm 0.037 \text{ km s}^{-1}$  were measured on 2024 December 14 (BJD 2460659.772) and 2025 February 11 (BJD 2460718.34031), respectively. The mean RV is  $-3.315 \pm 0.042 \text{ km s}^{-1}$ . 30B (CD-23 8096) was observed twice at McDonald Observatory and WISE Observatory, respectively. RVs of  $-3.195 \pm 0.057 \text{ km s}^{-1}$  and  $-3.195 \pm 0.079 \text{ km s}^{-1}$  were measured on 2024 December 18 (BJD 2460663.93401) and 2025 February 11 (BJD 2460718.71122), respectively. The mean RV is  $-3.195 \pm 0.069 \text{ km s}^{-1}$ .

31A (HD 81268) was observed twice at McDonald Observatory and WISE Observatory, respectively. RVs of  $14.892 \pm 0.026 \text{ km s}^{-1}$  and  $14.815 \pm 0.021 \text{ km s}^{-1}$  were measured on 2024 December 16 (BJD 2460661.891) and 2025 February 13 (BJD 2460720.64292), respectively. The mean RV is  $14.854 \pm 0.024 \text{ km s}^{-1}$ . 31B (BD-08 2665) was observed twice at McDonald Observatory and SAAO, respectively. RVs of  $15.214 \pm 0.036 \text{ km s}^{-1}$  and  $15.147 \pm 0.031 \text{ km s}^{-1}$  were measured on 2024 December 16 (BJD 2460661.908) and 2025 February 15 (BJD 2460722.53986), respectively. The mean RV is  $15.181 \pm 0.034 \text{ km s}^{-1}$ .

32A (HD 85137) was observed twice at SAAO. RVs of  $3.960 \pm 0.048 \text{ km s}^{-1}$  and  $3.874 \pm 0.048 \text{ km s}^{-1}$  were measured on 2024 December 13 (BJD 2460658.486) and 2025 February 9 (BJD 2460716.33343), respectively. The mean RV is  $3.917 \pm 0.048 \text{ km s}^{-1}$ . 32B (CD-57 2838) was observed twice at WISE Observatory. RVs of  $4.353 \pm 0.081 \text{ km s}^{-1}$  and  $4.155 \pm 0.060 \text{ km s}^{-1}$  were measured on 2024 December 13 (BJD 2460658.715) and 2025 February 9 (BJD 2460716.70867), respectively. The mean RV is  $4.254 \pm 0.071 \text{ km s}^{-1}$ .

33A (HD 88418) was observed twice at SAAO. RVs of  $-42.705 \pm 0.096 \text{ km s}^{-1}$  and  $-42.861 \pm 0.072 \text{ km s}^{-1}$  were measured on 2025 February 15 (BJD 2460722.37206) and 2025 March 4 (BJD 2460739.43796), respectively. The mean RV is  $-42.783 \pm 0.085 \text{ km s}^{-1}$ . 33B (TYC 251-458-1) was observed twice at McDonald Observatory and WISE Observatory, respectively. RVs of  $-42.430 \pm 0.081 \text{ km s}^{-1}$  and  $-42.458 \pm 0.059 \text{ km s}^{-1}$  were measured on 2025 February 15 (BJD 2460722.84552) and 2025 March 3 (BJD 2460738.78113), respectively. The mean RV is  $-42.444 \pm 0.071 \text{ km s}^{-1}$ .

35A (HD 92677) was observed twice at SAAO. RVs of  $1.398 \pm 0.030 \text{ km s}^{-1}$  and  $1.418 \pm 0.056 \text{ km s}^{-1}$  were measured on 2024 December 13 (BJD 2460658.572) and 2025 February 10 (BJD 2460717.46585), respectively. The mean RV is  $1.408 \pm 0.045 \text{ km s}^{-1}$ . 35B (HD 92652) was observed twice at WISE Observatory. RVs of  $1.030 \pm 0.047 \text{ km s}^{-1}$  and  $1.019 \pm 0.066 \text{ km s}^{-1}$  were measured on 2024 December 13 (BJD 2460658.842) and 2025 February 9 (BJD 2460716.72902), respectively. The mean RV is  $1.025 \pm 0.057 \text{ km s}^{-1}$ .

38A (HD 101574) was observed twice at McDonald Observatory and SAAO, respectively. RVs of  $1.665 \pm 0.045 \text{ km s}^{-1}$  and  $-0.013 \pm 0.073 \text{ km s}^{-1}$  were measured on 2024 December 15 (BJD 2460734.79018) and 2025 February 10 (BJD 2460717.43468), respectively. The mean RV is  $0.826 \pm 0.061 \text{ km s}^{-1}$ . 38B (BD-01 2557) was observed twice at WISE Observatory. RVs of  $0.573 \pm 0.047 \text{ km s}^{-1}$  and  $0.559 \pm 0.090 \text{ km s}^{-1}$  were measured on 2024 December 15 (BJD 2460660.840) and 2025 February 10 (BJD 2460717.67514), respectively. The mean RV is  $0.566 \pm 0.072 \text{ km s}^{-1}$ .

41A (HD 105350) was observed twice at WISE Observatory. RVs of  $29.135 \pm 0.074 \text{ km s}^{-1}$  and  $29.000 \pm 0.045 \text{ km s}^{-1}$  were measured on 2024 December 14 (BJD 2460659.794) and 2025 March 3 (BJD 2460738.86556), respectively. The mean RV is  $29.068 \pm 0.061 \text{ km s}^{-1}$ . 41B (TYC 7763-590-1) was observed twice at SAAO. RVs of  $29.453 \pm 0.107 \text{ km s}^{-1}$  and  $29.182 \pm 0.069 \text{ km s}^{-1}$  were measured on 2024 December 24 (BJD 2460669.51094) and 2025 March 4 (BJD 2460739.56682), respectively. The mean RV is  $29.318 \pm 0.090 \text{ km s}^{-1}$ .

42A (HD 107434) was observed twice at SAAO. RVs of  $-9.966 \pm 0.084 \text{ km s}^{-1}$  and  $-10.169 \pm 0.076 \text{ km s}^{-1}$  were measured on 2024 December 13 (BJD 2460658.555) and 2025 February 28 (BJD 2460735.54704), respectively. The mean RV is  $-10.067 \pm 0.080 \text{ km s}^{-1}$ . 42B (CD-37 7822) was observed twice at WISE Observatory. RVs of  $-9.649 \pm 0.068 \text{ km s}^{-1}$  and  $-9.348 \pm 0.077 \text{ km s}^{-1}$  were measured on 2024 December 12 (BJD 2460657.841) and 2025

February 28 (BJD 2460735.65839), respectively. The mean RV is  $-9.499 \pm 0.073 \text{ km s}^{-1}$ .

44A (HD 123033) was observed twice at McDonald Observatory and WISE Observatory. RVs of  $-19.677 \pm 0.069 \text{ km s}^{-1}$  and  $-20.018 \pm 0.064 \text{ km s}^{-1}$  were measured on 2025 February 17 (BJD 2460724.83569) and 2025 March 3 (BJD 2460738.8245), respectively. The mean RV is  $-19.847 \pm 0.066 \text{ km s}^{-1}$ . 44B (BD+26 2522) was observed twice at McDonald Observatory and WISE Observatory. RVs of  $-19.314 \pm 0.042 \text{ km s}^{-1}$  and  $-19.117 \pm 0.054 \text{ km s}^{-1}$  were measured on 2025 February 8 (BJD 2460715.83734) and 2025 March 5 (BJD 2460740.82101), respectively. The mean RV is  $-19.215 \pm 0.048 \text{ km s}^{-1}$ .

47A (BD+08 2889) was observed twice at SAAO and WISE Observatory. RVs of  $-17.980 \pm 0.025 \text{ km s}^{-1}$  and  $-17.948 \pm 0.033 \text{ km s}^{-1}$  were measured on 2025 February 11 (BJD 2460718.58422) and 2025 February 28 (BJD 2460735.77632), respectively. The mean RV is  $-17.964 \pm 0.029 \text{ km s}^{-1}$ . 47B (BD+08 2887) was observed twice at WISE Observatory. RVs of  $-17.954 \pm 0.085 \text{ km s}^{-1}$  and  $-17.921 \pm 0.055 \text{ km s}^{-1}$  were measured on 2025 February 11 (BJD 2460718.83524) and 2025 February 26 (BJD 2460733.78058), respectively. The mean RV is  $-17.937 \pm 0.071 \text{ km s}^{-1}$ .

48A (HD 129171) was observed twice at McDonald Observatory. RVs of  $-11.419 \pm 0.022 \text{ km s}^{-1}$  and  $-11.393 \pm 0.030 \text{ km s}^{-1}$  were measured on 2024 December 23 (BJD 2460668.97809) and 2025 February 5 (BJD 2460712.89457), respectively. The mean RV is  $-11.406 \pm 0.026 \text{ km s}^{-1}$ . 48B (HD 129209) was observed twice at McDonald Observatory. RVs of  $-11.129 \pm 0.032 \text{ km s}^{-1}$  and  $-11.118 \pm 0.032 \text{ km s}^{-1}$  were measured on 2024 December 14 (BJD 2460660.018) and 2025 February 5 (BJD 2460712.99954), respectively. The mean RV is  $-11.123 \pm 0.032 \text{ km s}^{-1}$ .

## B. DESCRIPTION OF MAROON-X OBSERVATIONS AND DATA REDUCTION OF RADIAL VELOCITIES

A sample of 6 wide binaries were selected from the [K. El-Badry et al. \(2021\)](#) catalog mainly with the requirement of Equation (A1) for measurements of RVs with MAROON-X. MAROON-X is a high-resolution fiber-fed optical echelle spectrograph on the Gemini North telescope, designed for detecting Earth-size planets ([A. Seifahrt et al. 2018](#)). It delivers a resolving power of  $R \sim 80,000$  over  $5000 - 9200 \text{ \AA}$ . Our observations were obtained in 2024B semester under the K-GMT Science Program (Program ID: GN-2024B-Q-122). Exposure times ranged from 90 to 1200 seconds, set to achieve a peak SNR of roughly 100. Data were reduced with the MAROON-X team's custom pipeline. We then extracted continuous 1D spectra and applied barycentric corrections. Relative radial velocities between the two components of each wide binary were measured via the CCF using the IRAF task `fxcor`. A summary of the observations is provided in Table 5.

**Table 5. MAROON-X measurements of relative radial velocities in 6 wide binaries**

Name	Gaia DR3 identifier	Sep <sup>a</sup> [kau]	Mass <sup>b</sup> [ $M_{\odot}$ ]	ruwe	Spec Type	RV(DR3) [ $\text{km s}^{-1}$ ]	$v_r$ (MAROON-X) <sup>c</sup> [ $\text{km s}^{-1}$ ]
TYC 4264-485-1	2201661297490051968	8.370	1.02	0.963		$-12.734 \pm 0.251$	$-0.0182 \pm 0.006$
TYC 4264-252-1	2201661091331626752		0.999	0.860		$-12.387 \pm 0.268$	
TYC 2700-274-1	1871558941576158464	7.750	0.791	0.877		$-22.921 \pm 0.291$	$-0.0239 \pm 0.009$
TYC 2700-210-1	1871559697490418816		0.771	0.992		$-23.347 \pm 0.326$	
TYC 2743-1157-1	1902676117063910016	6.271	0.899	1.282		$3.745 \pm 0.365$	$-0.9863 \pm 0.005$
LSPM J2231+3454	1902679033343158528		0.879	1.271		$3.330 \pm 0.390$	
TYC 3640-273-1	1942384773344557184	9.209	0.84	0.956		$-8.452 \pm 0.202$	$0.2663 \pm 0.084$
PM J23201+4819	1942384872124424832		0.565	1.116		$-9.100 \pm 0.238$	
TYC 1101-86-1	1762461893163118464	8.828	0.941	0.931		$-75.799 \pm 0.252$	$0.2199 \pm 0.004$
TYC 1101-87-1	1762461309047562368		0.939	1.156		$-76.334 \pm 0.238$	
BD+00 4500	4230699363889120128	5.247	1.091	1.124	G0	$-38.226 \pm 0.165$	$-0.2781 \pm 0.022$
BD+00 4497	4230699329529382400		0.878	0.949	K8	$-38.244 \pm 0.514$	

<sup>a</sup>2D separation: Sky-plane physical separation from [K. El-Badry et al. \(2021\)](#).

<sup>b</sup>Stellar mass based on the mass-magnitude relation derived by [K.-H. Chae \(2023\)](#).

<sup>c</sup>Relative radial velocity  $v_r$  ( $\equiv \text{RV}_A - \text{RV}_B$ ).

## C. SELECTION OF WIDE BINARIES FROM THE SCARPA ET AL. SAMPLE

Here we describe our selection of wide binary candidates from the [R. Scarpa et al. \(2017\)](#) sample of 58 pairs that have precise RVs measured in January and December 2013 with the fiber-fed FIES Echelle spectrograph at the 2.5m Nordic Optical Telescope, the Roque de Los Muchachos observatory in the Canary islands. Although this sample is far from a well-defined sample of wide binaries and contains many unbound pairs, we consider it because it contains true wide binaries with very precise RVs.

Since we eventually need only uncontaminated pure binaries, we remove obviously unbound, contaminated, or problematic cases by individually examining the pairs. Specifically, we exclude any pair in which (1) Gaia's `ruwe` has unacceptably large value(s) (e.g.,  $> 1.5$ ), (2) RV(s) show(s) unacceptably large variation(s) in time or with respect to Gaia DR3, (3) the scalar relative RV ( $|v_r|$ ) is too large (e.g.,  $|v_r| > 2 \text{ km s}^{-1}$ ) indicating an obviously gravitationally-unbound system, or (4) the sky-plane 2D physical separation is too large  $> 0.22 \text{ pc}$  or  $> 45 \text{ kau}$ , because any systems beyond the limit are more likely to be gravitationally unbound and require much more precise velocities. We are left with only 24 systems, which are listed in Table 6. All 24 systems are included in the raw sample of 306 systems shown in Figure 2.

Although the majority of the [R. Scarpa et al. \(2017\)](#) sample has already been excluded, it turns out that the remaining sample is relatively more contaminated than our other samples such as LCO and MAROON-X described in Appendix A and B, which are selected from previous statistical samples used by one of us (e.g., [K.-H. Chae 2024a](#)). This may be because the above exclusion criterion for  $|v_r|$  is not tight enough, so that boosted velocities due to unseen perturbers may be present. Indeed, as shown in Section 3.3.1, the Hipparcos-Gaia relative PM comparison identified three cases of unacceptably large variation between the two observations, and they all are from the [R. Scarpa et al. \(2017\)](#) sample listed in Table 6.

The relatively high fraction of contaminated cases can be seen by the scalar 3D velocity  $v_{\text{obs}}$  listed in the penultimate column of Table 6. There are 9 systems with  $v_{\text{obs}} > 1 \text{ km s}^{-1}$  including 3 systems with  $v_{\text{obs}} > 1.5 \text{ km s}^{-1}$ . Three of them are the above contaminated cases identified by the Hipparcos-Gaia test: HIP54692/HIP54681 ( $v_{\text{obs}} = 1.690$ ), HIP65602/HIP65574 (1.053), and HIP101916/HIP101932 (1.632). In contrast, the clean statistical sample does not contain any case with  $v_{\text{obs}} > 1 \text{ km s}^{-1}$  (see Table 3 for systems with relatively large values of  $v_{\text{obs}}$  among the clean sample).

The systems in Table 6 can be further tested with the relative velocity threshold of Equation (A1) for  $v_r$  and  $v_p$ . The velocity  $v_p$  is also considered because the relative PMs were not used in selecting the systems. Three systems fail this test, as indicated in the last column of Table 6. These systems are excluded from gravity tests in this work. These systems exactly match the three systems with  $v_{\text{obs}} > 1.5 \text{ km s}^{-1}$ , and two of them are the contaminated cases identified by the Hipparcos-Gaia test. Thus, 4 out of the 9 systems with  $v_{\text{obs}} > 1 \text{ km s}^{-1}$  are excluded by the velocity threshold and the Hipparcos-Gaia test. It is unclear whether the remaining 5 cases with  $1 < v_{\text{obs}} < 1.5 \text{ km s}^{-1}$  from the [R. Scarpa et al. \(2017\)](#) sample are also contaminated. It will be interesting to see what future data will reveal about these systems.

Despite the relatively high fraction of contaminated cases, the [R. Scarpa et al. \(2017\)](#) sample is useful in this study because it provides independent measurements at different epochs for true pure binaries. Indeed, for 7 systems from the clean sample the [R. Scarpa et al. \(2017\)](#) values confirm the stability of  $v_r$  in conjunction with other measurements over more than several years (see Table 1). Also, as demonstrated above, the sample inadvertently provided useful negative examples of contaminated cases through the Hipparcos-Gaia test and the velocity threshold. The [R. Scarpa et al. \(2017\)](#) sample seems to provide a useful testbed for kinematically contaminated cases.

**Table 6. Wide binaries selected from R. Scarpa et al. (2017)**

Name	Gaia DR3 identifier	Sep <sup>a</sup> [kau]	Mass <sup>b</sup> [ $M_{\odot}$ ]	RV(DR3) <sup>c</sup> [ $\text{km s}^{-1}$ ]	RV(Scarpa) <sup>d</sup> [ $\text{km s}^{-1}$ ]	$v_r$ <sup>e</sup> [ $\text{km s}^{-1}$ ]	$v_p$ <sup>f</sup> [ $\text{km s}^{-1}$ ]	$v_{\text{obs}}$ <sup>g</sup> [ $\text{km s}^{-1}$ ]	Test <sup>h</sup>
HIP11137	76300510625993344	2.090	0.998	$27.138 \pm 0.175$	$27.129 \pm 0.014$	$-0.157 \pm 0.021$	$0.535 \pm 0.007$	$0.558 \pm 0.009$	Pass
HIP11134	76300476266255488		0.925	$27.010 \pm 0.139$	$27.286 \pm 0.016$				
HIP15304	10584899657116672	7.340	1.162	$31.392 \pm 0.133$	$31.860 \pm 0.019$	$-0.856 \pm 0.027$	$0.547 \pm 0.009$	$1.016 \pm 0.023$	Pass
HIP15310	10608573516849536		1.092	$32.068 \pm 0.143$	$32.716 \pm 0.019$				
HIP15527	5060104351007433472	9.082	0.960	$39.849 \pm 0.118$	$40.287 \pm 0.019$	$-0.377 \pm 0.024$	$0.225 \pm 0.004$	$0.439 \pm 0.020$	Pass
HIP15526	5060105897197110144		0.880	$40.270 \pm 0.120$	$40.664 \pm 0.014$				
HIP19859	3285218186904332288	1.417	1.070	$-7.277 \pm 0.137$	$-6.858 \pm 0.012$	$0.572 \pm 0.020$	$0.966 \pm 0.005$	$1.122 \pm 0.011$	Pass
HIP19855	3285218255623808640		0.960	$-8.010 \pm 0.130$	$-7.430 \pm 0.016$				
HIP21537	3230677565443833088	4.972	1.160	$38.397 \pm 0.135$	$38.947 \pm 0.016$	$-0.135 \pm 0.022$	$0.265 \pm 0.013$	$0.298 \pm 0.015$	Pass

**Table 6** *continued*

Table 6 (continued)

HIP21534	3230677874682668672	1.150	$38.724 \pm 0.133$	$39.082 \pm 0.015$							
HIP22611	4873223829966552192	5.959	1.503	$45.755 \pm 0.120$	$46.203 \pm 0.015$	$-0.241 \pm 0.022$	$0.661 \pm 0.006$	$0.704 \pm 0.009$	Pass		
HIP22604	4873226853623529856	0.997		$45.859 \pm 0.165$	$46.444 \pm 0.016$						
HIP25278	3400292798990117888	10.311	1.135	$37.701 \pm 0.138$	$38.350 \pm 0.047$	$-0.253 \pm 0.052$	$0.106 \pm 0.006$	$0.274 \pm 0.048$	Pass		
HIP25220	3394298532176344960	0.738		$38.032 \pm 0.124$	$38.603 \pm 0.023$						
HIP33705	5607190344506642432	12.331	1.150	$16.441 \pm 0.125$	$16.700 \pm 0.027$	$-0.441 \pm 0.032$	$0.100 \pm 0.005$	$0.452 \pm 0.031$	Pass		
HIP33691	5607189485513198208	0.880		$16.726 \pm 0.141$	$17.141 \pm 0.017$						
HIP34426	3359808231100381312	8.189	1.106	$-11.840 \pm 0.141$	$-11.544 \pm 0.013$	$0.791 \pm 0.017$	$1.612 \pm 0.007$	$1.796 \pm 0.010$	Fail		
HIP34407	3359820016490648576	1.086		$-12.835 \pm 0.153$	$-12.335 \pm 0.011$						
HIP39457	5595858262287843840	4.421	1.200	$26.293 \pm 0.139$	$26.807 \pm 0.015$	$-0.741 \pm 0.022$	$0.791 \pm 0.008$	$1.084 \pm 0.016$	Pass		
HIP39452	5595858159201264768	1.016		N/A	$27.548 \pm 0.016$						
HIP44858	692119656035933568	2.524	1.014	$29.976 \pm 0.139$	$30.473 \pm 0.010$	$-0.292 \pm 0.015$	$0.565 \pm 0.007$	$0.636 \pm 0.009$	Pass		
HIP44864	692120029700390912	1.013		$30.380 \pm 0.129$	$30.765 \pm 0.011$						
HIP45836	1019361632454363904	6.732	1.206	$-7.895 \pm 0.128$	$-7.761 \pm 0.012$	$-1.337 \pm 0.016$	$0.673 \pm 0.004$	$1.497 \pm 0.014$	Pass		
HIP45859	1019174509319377536	0.919		$-6.780 \pm 0.127$	$-6.424 \pm 0.010$						
HIP52787	3550081879381593728	7.870	0.820	$23.759 \pm 0.148$	$24.212 \pm 0.019$	$-0.410 \pm 0.029$	$0.228 \pm 0.005$	$0.469 \pm 0.026$	Pass		
HIP52776	3550084490721711872	0.700		$24.451 \pm 0.180$	$24.622 \pm 0.022$						
HIP54692	777967084390189696	6.185	1.194	$11.222 \pm 0.132$	$11.696 \pm 0.011$	$1.353 \pm 0.015$	$1.012 \pm 0.008$	$1.690 \pm 0.013$	Fail		
HIP54681	777967702865481344	0.996		$9.949 \pm 0.152$	$10.343 \pm 0.010$						
HIP58067	3975129194660883328	2.893	0.956	$5.965 \pm 0.198$	$6.461 \pm 0.015$	$0.141 \pm 0.021$	$0.202 \pm 0.006$	$0.246 \pm 0.013$	Pass		
HIP58073	3975223065466473216	0.927		$5.801 \pm 0.140$	$6.320 \pm 0.014$						
HIP64057	3945118265299248128	1.458	0.948	$-1.565 \pm 0.130$	$-1.247 \pm 0.014$	$0.017 \pm 0.019$	$0.361 \pm 0.009$	$0.362 \pm 0.009$	Pass		
HIP64059	3945118643256370688	0.896		$-1.673 \pm 0.147$	$-1.264 \pm 0.013$						
HIP65602	6193279279612173952	9.539	0.816	$-13.492 \pm 0.144$	$-12.884 \pm 0.018$	$-1.014 \pm 0.025$	$0.282 \pm 0.004$	$1.053 \pm 0.025$	Pass		
HIP65574	6193280031230266752	0.811		$-12.211 \pm 0.128$	$-11.870 \pm 0.018$						
HIP71726	1282815063829295360	16.772	1.030	$-11.925 \pm 0.121$	$-11.468 \pm 0.015$	$-0.170 \pm 0.021$	$0.142 \pm 0.008$	$0.221 \pm 0.017$	Pass		
HIP71737	1282817022334383232	1.000		$-11.598 \pm 0.124$	$-11.298 \pm 0.015$						
HIP74442	1274568245587206016	2.293	1.152	$-60.315 \pm 0.141$	$-60.207 \pm 0.016$	$-0.962 \pm 0.023$	$0.330 \pm 0.007$	$1.017 \pm 0.022$	Pass		
HIP74439	1274562370068531712	0.975		$-59.383 \pm 0.174$	$-59.245 \pm 0.016$						
HIP85620	1440518669436791296	8.824	1.094	$-34.155 \pm 0.127$	$-33.736 \pm 0.027$	$-0.442 \pm 0.034$	$0.139 \pm 0.006$	$0.463 \pm 0.033$	Pass		
HIP85575	1440425863783337856	0.970		$-33.661 \pm 0.132$	$-33.294 \pm 0.021$						
HIP99729	4249652990144051840	2.736	1.060	$-0.464 \pm 0.129$	$-0.011 \pm 0.018$	$0.061 \pm 0.026$	$0.834 \pm 0.010$	$0.836 \pm 0.010$	Pass		
HIP99727	4249652783985617920	1.050		$-0.388 \pm 0.138$	$-0.072 \pm 0.019$						
HIP101082	2298101352139398144	13.722	1.949	$-14.467 \pm 0.118$	$-14.069 \pm 0.014$	$-0.322 \pm 0.020$	$0.127 \pm 0.010$	$0.346 \pm 0.019$	Pass		
HIP101166	2298101901895214720	1.042		$-14.117 \pm 0.149$	$-13.747 \pm 0.014$						
HIP101916	1754191435419155456	6.401	1.566	$-54.097 \pm 0.124$	$-53.457 \pm 0.015$	$-0.339 \pm 0.022$	$1.596 \pm 0.010$	$1.632 \pm 0.011$	Fail		
HIP101932	1754191229260708736	0.841		$-53.510 \pm 0.136$	$-53.118 \pm 0.016$						
HIP118254	2882262637207289216	4.703	1.041	$29.940 \pm 0.128$	$30.368 \pm 0.016$	$0.747 \pm 0.021$	$0.280 \pm 0.004$	$0.798 \pm 0.020$	Pass		
HIP118251	2882262529831237120	0.973		$29.271 \pm 0.128$	$29.621 \pm 0.014$						

<sup>a</sup> 2D separation: Sky-plane physical separation from K. El-Badry et al. (2021).

<sup>b</sup> Stellar mass based on the mass-magnitude relation derived by K.-H. Chae (2023).

<sup>c</sup> Radial velocity from Gaia DR3.

<sup>d</sup> Radial velocity from R. Scarpa et al. (2017).

<sup>e</sup> Relative radial velocity  $v_r$  ( $\equiv \text{RV}_A - \text{RV}_B$ ) from R. Scarpa et al. (2017).

<sup>f</sup> Scalar sky-plane 2D velocity  $v_p$  ( $\equiv \sqrt{v_{x'}^2 + v_{y'}^2}$ ) from Gaia DR3.

<sup>g</sup> Scalar 3D velocity  $v_{\text{obs}}$  ( $\equiv \sqrt{v_p^2 + v_z^2}$ ).

<sup>h</sup> Test with  $v_r$  and  $v_p$  based on the threshold given by Equation (A1).

#### D. SELECTION OF WIDE BINARIES WITH RADIAL VELOCITIES FROM SDSS4 APOGEE

The SDSS4 APOGEE survey measured RVs for a large number of stars using high-resolution, multi-object, near-infrared spectroscopy. APOGEE RVs are available on the SDSS DR17 website <https://www.sdss4.org/dr17/irspec/use-radial-velocities/>. The precision reported for an individual RV is often better than  $100\text{m s}^{-1}$  and in some cases better than  $50\text{m s}^{-1}$ . Thus, APOGEE RVs potentially provide precise relative RVs for a number of wide binaries. The file `allStar-dr17-synspec-rev1.fits` downloadable from the website provides RVs for 733901 stars, 717925 of which have Gaia DR3 identifications.

We search for wide binaries from the 717925 stars with Gaia DR3 identifications. Wide binary candidates are selected from the [K. El-Badry et al. \(2021\)](#) catalog. Once a candidate binary with APOGEE RVs for both stars is found, we check whether the radial velocity difference between the pair can be consistent with a gravitationally bound system. We use the threshold given by Equation (A1). We have found 208 wide binaries within 300 pc from the Sun, which are listed in Table 7. For 15 of them, RVs for both components were measured multiple times at multiple epochs. For these systems, Table 7 gives only the error-weighted mean and its error, while Table 8 gives all the measured values.

Each measurement of RV for a star is based on NVISITS ( $\geq 1$ ) “visit(s)” of the star. The given value of RV refers to a signal-to-noise ratio (SNR)-weighted average if NVISITS  $> 1$  stored in the APOGEE parameter `VHELIO_AVG`. The given nominal error (Err) refers to the SNR-weighted uncertainty stored in the APOGEE parameter `VERR`. When multiple observations (each of which may have multiple visits) were made at multiple epochs, the given value of RV and its error refer to the error-weighted mean of RVs and its uncertainty. For each value of RV, two additional errors are given in the table: ‘Disp’ and ‘Scatt’. Disp simply refers to the standard deviation of RVs from multiple observations at multiple epochs. It is set to zero when only a single-epoch observation (regardless of NVISITS) was made. Scatt refers to the scatter in multiple visits in an observation stored in the APOGEE parameter `VSCATTER`. When multiple observations were made, the given value of Scatt refers to the maximum value. Scatt is zero when there was only a single observation with a single visit. Disp is provided as a qualitative check of the variability of RV when multiple observations are available while Scatt is used to select reliable RVs. Because Scatt is not available for all RVs, the nominal error ‘Err’ is used in estimating the nominal uncertainty of the relative RV  $v_r$  between the two stars. Note that Err is either smaller or larger than Scatt as can be seen in Table 7. The majority of wide binaries have  $\sigma_{v_r} < 0.1 \text{ km s}^{-1}$  and 195 wide binaries with  $\sigma_{v_r} < 0.35 \text{ km s}^{-1}$  are included in the raw sample of the main part shown in Figure 4.

**Table 7. Summary of wide binaries with radial velocities from the SDSS DR17 APOGEE database**

identifier	$s^a$ [kau]	Mass <sup>b</sup> [ $M_\odot$ ]	RV <sup>c</sup> [ $\text{km s}^{-1}$ ]	Err <sup>d</sup> [ $\text{km s}^{-1}$ ]	Disp <sup>e</sup> [ $\text{km s}^{-1}$ ]	Scatt <sup>f</sup> [ $\text{km s}^{-1}$ ]	$v_r^g$ [ $\text{km s}^{-1}$ ]	$\sigma_{v_r}$ [ $\text{km s}^{-1}$ ]	multi-epoch <sup>h</sup>
Gaia DR3 5961072491289480960	4.449	0.537	-1.252	0.054	0.000	0.000	-0.067	0.081	
Gaia DR3 5961072456929737216		0.524	-1.185	0.060	0.000	0.014			
Gaia DR3 466294295706341760	6.201	1.025	-1.956	0.034	0.000	0.000	-0.660	0.065	
Gaia DR3 466291787445425408		0.392	-1.296	0.055	0.000	0.240			
Gaia DR3 750184379766219648	10.229	0.790	19.668	0.026	0.000	0.053	-0.188	0.125	
Gaia DR3 750184311046743168		0.688	19.856	0.122	0.000	0.089			
Gaia DR3 6619469571588636288	3.274	0.626	-8.789	0.060	0.000	0.077	0.134	0.102	
Gaia DR3 6619469571588635904		0.497	-8.923	0.082	0.000	0.107			
Gaia DR3 2344436971156155904	16.197	1.032	23.537	0.024	0.000	0.037	-0.398	0.069	
Gaia DR3 2344437246034051968		0.507	23.935	0.065	0.000	0.112			
Gaia DR3 2342666791794987264	11.690	0.917	22.908	0.025	0.000	0.036	-0.380	0.112	
Gaia DR3 2342666138959958400		0.387	23.288	0.109	0.000	0.252			
Gaia DR3 607218804112579968	15.567	0.821	27.141	0.031	0.000	0.000	-0.341	0.050	
Gaia DR3 607218765457083904		0.610	27.482	0.039	0.000	0.000			
Gaia DR3 605713022937691136	2.744	1.551	26.605	0.167	0.000	0.000	0.174	0.188	
Gaia DR3 605712812485668352		0.834	26.431	0.086	0.000	0.000			
Gaia DR3 2642922251741817216	4.581	0.548	23.539	0.028	0.059	0.044	-0.156	0.040	Yes
Gaia DR3 2642922286101533952		0.528	23.695	0.029	0.042	0.062			
Gaia DR3 5279010553386994048	13.361	0.486	44.107	0.036	0.000	0.000	-0.021	0.107	
Gaia DR3 5278997561113174016		0.401	44.128	0.101	0.000	0.000			
Gaia DR3 3053911383155592832	12.824	0.528	56.530	0.035	0.000	0.050	-0.225	0.054	
Gaia DR3 3053907221325174144		0.498	56.755	0.041	0.000	0.068			
Gaia DR3 2119132916774654080	2.522	1.242	-21.516	0.023	0.000	0.044	0.536	0.043	

**Table 7** *continued*

Table 7 (continued)

Gaia DR3 2119132916774654208	0.863	-22.052	0.036	0.000	0.030		
Gaia DR3 2119404186908641792	1.828	0.637	-14.241	0.048	0.000	0.089	0.487 0.061
Gaia DR3 2119404186908642048	0.623	-14.728	0.037	0.000	0.000		
Gaia DR3 2029433521248546304	2.849	1.041	-44.770	0.033	0.000	0.000	0.224 0.152
Gaia DR3 2029432043779954432	0.196	-44.994	0.148	0.000	0.154		
Gaia DR3 5183999279727496448	18.627	1.275	-5.200	0.030	0.000	0.078	0.056 0.042
Gaia DR3 5183999309791637504	0.924	-5.256	0.030	0.000	0.018		
Gaia DR3 5174322615330339456	4.858	0.714	18.562	0.028	0.000	0.030	-0.668 0.111
Gaia DR3 5174322855848505728	0.262	19.230	0.107	0.000	0.146		
Gaia DR3 3840226230398314368	48.488	0.523	-4.704	0.056	0.000	0.113	-0.140 0.085
Gaia DR3 3840219358450646656	0.494	-4.564	0.064	0.000	0.414		
Gaia DR3 652232737138721280	23.846	0.590	97.005	0.050	0.114	0.000	-0.288 0.132
Gaia DR3 652239441584849280	0.586	97.293	0.122	0.000	0.000		
Gaia DR3 48167959442012672	1.854	0.853	10.825	0.028	0.000	0.000	-0.848 0.046
Gaia DR3 48167955146062720	0.669	11.673	0.037	0.000	0.000		
Gaia DR3 2501323948860951296	19.938	1.027	-26.327	0.027	0.031	0.066	-0.014 0.040
Gaia DR3 2501325525113734912	0.749	-26.313	0.030	0.064	0.115		Yes
Gaia DR3 2501911740905243392	3.483	0.817	53.014	0.027	0.000	0.000	-0.684 0.042
Gaia DR3 2501911740905243136	0.776	53.698	0.032	0.000	0.044		
Gaia DR3 1356763886586884864	5.370	0.765	-36.526	0.021	0.039	0.029	0.177 0.043
Gaia DR3 1356763852227145344	0.704	-36.703	0.037	0.000	0.003		
Gaia DR3 1352381027080312832	24.561	1.236	-25.485	0.020	0.008	0.010	-0.151 0.039
Gaia DR3 1352427996842670464	0.698	-25.334	0.033	0.000	0.023		
Gaia DR3 1357040379401720448	1.506	0.929	-21.890	0.028	0.000	0.010	-0.137 0.040
Gaia DR3 1357040345041982464	0.701	-21.753	0.028	0.605	0.087		
Gaia DR3 2125816160770555904	2.111	0.800	11.132	0.042	0.000	0.045	0.659 0.379
Gaia DR3 2125816160770558592	0.431	10.473	0.377	0.000	2.102		
Gaia DR3 3861880665230888960	19.322	1.301	13.512	0.043	0.000	0.017	0.386 0.051
Gaia DR3 3858878375716469120	0.922	13.126	0.027	0.000	0.051		
Gaia DR3 3861953095559329536	29.682	0.740	14.441	0.039	0.000	0.010	-0.301 0.058
Gaia DR3 3861952369709297536	0.720	14.742	0.043	0.000	0.007		
Gaia DR3 217107577453306112	3.417	0.835	22.261	0.020	0.013	0.144	0.433 0.030
Gaia DR3 217107607515576704	0.660	21.828	0.022	0.045	0.056		Yes
Gaia DR3 665747663485734016	4.126	0.748	-0.190	0.036	0.000	0.065	-0.491 0.062
Gaia DR3 665747663485733632	0.627	0.301	0.050	0.000	0.145		
Gaia DR3 663509878149021824	33.873	0.854	16.977	0.017	0.040	0.000	0.070 0.043
Gaia DR3 663515861040979584	0.607	16.907	0.039	0.000	0.000		
Gaia DR3 666293742807553024	2.991	0.862	21.017	0.037	0.000	0.013	-0.578 0.279
Gaia DR3 666293777167291008	0.411	21.595	0.277	0.000	0.000		
Gaia DR3 664055515090902144	1.352	0.363	26.148	0.056	0.000	0.000	0.120 0.096
Gaia DR3 664055412011687424	0.354	26.028	0.078	0.000	0.000		
Gaia DR3 664315652670220032	2.429	0.438	-2.690	0.123	0.000	0.848	-0.392 0.193
Gaia DR3 664315652670219776	0.424	-2.298	0.149	0.000	0.525		
Gaia DR3 2099859268216511488	0.337	0.428	-17.723	0.064	0.000	0.063	0.512 0.099
Gaia DR3 2099859268216512000	0.385	-18.235	0.075	0.000	0.000		
Gaia DR3 2100011516217168640	0.810	0.566	-42.882	0.051	0.000	0.118	0.510 0.110
Gaia DR3 2100011516217169920	0.553	-43.392	0.098	0.000	0.000		
Gaia DR3 2100451630105041152	2.030	1.203	-7.960	0.043	0.000	0.049	-0.757 0.055
Gaia DR3 2100451630105040256	0.790	-7.203	0.035	0.000	0.107		
Gaia DR3 2100501760964021504	17.569	1.060	10.209	0.030	0.000	0.000	0.184 0.040
Gaia DR3 2100502001482188032	1.002	10.025	0.027	0.000	0.000		
Gaia DR3 3811688440459523200	2.030	0.946	7.522	0.045	0.000	0.068	-0.907 0.082
Gaia DR3 3811688440459523456	0.593	8.429	0.068	0.000	0.000		
Gaia DR3 638830003928974336	0.365	0.540	14.947	0.131	0.000	5.215	2.290 0.181

Table 7 continued

Table 7 (continued)

Gaia DR3 638829999633204864	0.426	12.657	0.125	0.000	4.541			
Gaia DR3 2532890137420583168	20.057	0.533	-22.431	0.393	0.000	0.000	2.332 1.010	
Gaia DR3 2532890858975088512	0.470	-24.763	0.930	0.000	0.000			
Gaia DR3 2532980366093464832	28.332	0.968	9.318	0.059	11.282	0.000	0.828 0.279	
Gaia DR3 2532980499236841984	0.404	8.490	0.273	0.000	0.000			
Gaia DR3 2534384064484982016	1.217	0.293	6.042	0.155	0.000	0.079	-0.265 0.217	
Gaia DR3 2534384064484982400	0.279	6.307	0.152	0.000	0.152			
Gaia DR3 2534623758019863296	12.474	0.447	0.291	0.057	0.000	0.000	-0.035 0.092	
Gaia DR3 2534624685732797824	0.386	0.326	0.072	0.000	0.025			
Gaia DR3 2507987436001873408	6.302	1.081	-3.735	0.022	0.039	0.087	0.576 0.043	
Gaia DR3 2507987431706333184	0.967	-4.311	0.037	0.000	0.056			
Gaia DR3 2435485982863717120	1.885	0.999	-28.884	0.025	0.000	0.000	0.296 0.044	
Gaia DR3 2435485982863716992	0.640	-29.180	0.036	0.000	0.057			
Gaia DR3 2435551609963991936	27.394	1.537	-3.344	0.021	0.044	0.131	-0.916 0.330	
Gaia DR3 2435554599261229824	0.296	-2.428	0.329	0.000	0.581			
Gaia DR3 2128304183783972992	0.504	0.960	-21.532	0.032	0.000	0.085	-1.257 0.049	
Gaia DR3 2128304179486008704	0.816	-20.275	0.037	0.000	0.072			
Gaia DR3 2126777988630768000	1.792	1.059	-15.875	0.061	0.000	0.082	-0.297 0.080	
Gaia DR3 2126777992924832128	0.912	-15.578	0.051	0.000	0.052			
Gaia DR3 4088301956580684416	13.816	0.562	-11.303	0.082	0.000	0.000	0.524 0.243	
Gaia DR3 4088301823454290176	0.354	-11.827	0.229	0.000	0.000			
Gaia DR3 2783518418493208832	0.165	0.755	-2.501	0.052	0.000	0.433	0.908 0.078	
Gaia DR3 2783518212334778880	0.700	-3.409	0.058	0.000	0.000			
Gaia DR3 315289980082496000	3.346	0.730	12.902	0.026	0.000	0.043	-0.869 0.061	
Gaia DR3 315289980082496256	0.389	13.771	0.055	0.000	0.262			
Gaia DR3 3641315024925921024	2.553	1.003	-15.066	0.025	0.000	0.000	0.192 0.033	
Gaia DR3 3641315024927514880	0.703	-15.258	0.022	0.071	0.094			
Gaia DR3 3975013093104939904	1.935	0.400	28.683	0.074	0.000	0.174	0.005 0.344	
Gaia DR3 3975013093104939648	0.210	28.678	0.336	0.000	1.055			
Gaia DR3 3961746072270936320	27.208	0.964	-45.842	0.013	0.078	0.154	-0.091 0.021	Yes
Gaia DR3 3961745217573223296	0.720	-45.751	0.017	0.071	0.129			
Gaia DR3 3888309828090932608	2.493	0.479	-9.621	0.084	0.000	0.686	0.041 0.113	
Gaia DR3 3888309832385988992	0.432	-9.662	0.075	0.000	0.406			
Gaia DR3 3888520938618115456	1.114	0.386	64.304	0.225	0.000	0.453	0.320 0.536	
Gaia DR3 3888520938618496768	0.285	63.984	0.487	0.000	2.111			
Gaia DR3 2734917221406795648	1.600	1.017	-2.107	0.027	0.000	0.028	-0.691 0.059	
Gaia DR3 2734917221406795520	0.482	-1.416	0.052	0.075	0.480			
Gaia DR3 6823356823090355712	9.032	1.281	-20.233	0.041	0.000	0.066	-0.033 0.063	
Gaia DR3 6823356715715859840	1.253	-20.200	0.048	0.000	0.072			
Gaia DR3 6827446284791133184	3.608	0.875	-46.987	0.025	0.000	0.021	0.776 0.069	
Gaia DR3 6827446280496122112	0.601	-47.763	0.064	0.000	0.000			
Gaia DR3 2778254433563650048	1.213	0.794	2.065	0.026	0.000	0.006	-0.196 0.049	
Gaia DR3 2778254437855626240	0.566	2.261	0.041	0.000	0.004			
Gaia DR3 3016902642094840704	0.697	0.844	19.935	0.040	0.145	0.538	0.553 0.057	
Gaia DR3 3016902646391459328	0.755	19.382	0.041	0.000	0.000			
Gaia DR3 1261431280655790208	17.706	0.699	-31.270	0.102	0.000	0.674	-0.021 0.236	
Gaia DR3 1261431589893436288	0.556	-31.249	0.213	0.000	1.113			
Gaia DR3 1262819482805829760	2.507	0.341	-50.351	0.429	0.000	0.000	0.427 0.451	
Gaia DR3 1262819551525306624	0.258	-50.778	0.139	0.000	0.235			
Gaia DR3 2687603311918406528	11.324	0.985	12.188	0.034	0.000	0.021	0.090 0.053	
Gaia DR3 2687603208839189376	0.626	12.098	0.041	0.023	0.111			
Gaia DR3 2242465891977167872	1.233	1.330	-2.749	0.189	0.000	0.194	0.239 0.192	
Gaia DR3 2242465891977204992	0.916	-2.988	0.031	0.000	0.019			
Gaia DR3 1291638988239949056	7.655	0.681	-41.205	0.039	0.000	0.007	-0.025 0.146	

Table 7 continued

Table 7 (continued)

Gaia DR3 1291638988239948800	0.353	-41.180	0.141	0.000	0.217				
Gaia DR3 1292334704222207104	1.923	0.578	-5.693	0.040	0.000	0.118	-0.343	0.237	
Gaia DR3 1292334704222207232	0.248	-5.350	0.234	0.000	1.037				
Gaia DR3 2603390513756129152	22.756	1.150	-10.734	0.038	0.000	0.000	-0.208	0.073	
Gaia DR3 2603390410676914816	0.729	-10.526	0.062	0.000	0.000				
Gaia DR3 2615313579192094080	0.983	0.928	-16.558	0.028	0.000	0.018	0.703	0.360	
Gaia DR3 2615313579193124992	0.222	-17.261	0.359	0.000	0.276				
Gaia DR3 2601074839188320384	3.130	0.925	-1.307	0.033	0.000	0.053	-0.356	0.046	
Gaia DR3 2601074903612842880	0.908	-0.951	0.032	0.000	0.013				
Gaia DR3 2615509842018541184	1.940	0.919	-25.133	0.032	0.000	0.182	-0.512	0.085	
Gaia DR3 2615509842020990336	0.906	-24.621	0.079	0.000	0.000				
Gaia DR3 2597900304305485952	22.582	0.938	6.717	0.045	0.000	0.299	-0.066	0.068	
Gaia DR3 2597899930643579520	0.768	6.783	0.051	0.000	0.187				
Gaia DR3 2613542407694482816	1.031	0.995	15.920	0.023	0.000	0.067	-1.237	0.045	
Gaia DR3 2613542403398991360	0.952	17.157	0.039	0.000	0.000				
Gaia DR3 2627346157705716352	2.975	0.873	22.895	0.035	0.000	0.092	0.145	0.057	
Gaia DR3 2627346535662838272	0.654	22.750	0.045	0.000	0.041				
Gaia DR3 2623865584928390784	21.862	1.219	-31.354	0.028	0.000	0.000	-0.052	0.040	
Gaia DR3 2624616237837226368	1.051	-31.302	0.028	0.000	0.000				
Gaia DR3 2543548528262965248	5.541	1.294	-21.561	0.033	0.000	0.025	-0.702	0.049	
Gaia DR3 2543548528262965504	0.749	-20.859	0.036	0.000	0.048				
Gaia DR3 2565313665876247168	6.931	0.963	-13.701	0.025	0.000	0.000	-0.308	0.044	
Gaia DR3 2565313567092405888	0.784	-13.393	0.036	0.000	0.000				
Gaia DR3 2581807955200716800	19.842	0.764	-2.898	0.029	0.000	0.000	-0.011	0.072	
Gaia DR3 2581806619466249728	0.450	-2.887	0.066	0.000	0.000				
Gaia DR3 2581883413481515008	17.044	1.241	-14.699	0.023	0.055	0.000	-0.310	0.039	Yes
Gaia DR3 2581859911420471808	0.741	-14.389	0.032	0.104	0.000				
Gaia DR3 2582614416915244416	7.599	0.699	6.468	0.036	0.313	0.000	0.597	0.074	
Gaia DR3 2582614412620059520	0.467	5.871	0.065	0.000	0.000				
Gaia DR3 2588048478257634304	2.242	0.847	-5.600	0.039	0.000	0.077	0.347	0.049	
Gaia DR3 2588048473962161280	0.738	-5.947	0.029	0.027	0.091				
Gaia DR3 2588052051670468224	2.136	1.259	14.045	0.025	0.000	0.068	0.604	0.030	
Gaia DR3 2588051948591253376	0.808	13.441	0.017	0.007	0.079				
Gaia DR3 2594556109625136128	12.607	0.451	-8.800	0.050	0.000	0.000	0.128	0.092	
Gaia DR3 2594555491149842432	0.373	-8.928	0.077	0.000	0.000				
Gaia DR3 369668220425453920	34.216	0.950	10.107	0.046	0.000	0.102	-0.224	0.064	
Gaia DR3 3696681860656968064	0.899	10.331	0.044	0.000	0.017				
Gaia DR3 3698627961878292864	7.590	1.007	2.092	0.025	0.000	0.075	0.087	0.036	
Gaia DR3 3698627927518342144	0.861	2.005	0.026	0.245	0.108				
Gaia DR3 2157622725756418816	12.259	0.992	-37.939	0.023	0.000	0.000	0.472	0.035	
Gaia DR3 2157623451608162688	0.706	-38.411	0.027	0.000	0.000				
Gaia DR3 765428249492127104	13.781	0.485	5.792	0.069	0.000	0.367	0.201	0.104	
Gaia DR3 765417666692750080	0.332	5.591	0.078	0.000	0.155				
Gaia DR3 785716030026546688	18.845	0.810	-15.570	0.030	0.026	0.086	-0.089	0.051	Yes
Gaia DR3 785716682861545344	0.655	-15.481	0.041	0.059	0.166				
Gaia DR3 792284031455893376	5.031	0.973	-10.027	0.028	0.000	0.023	-0.274	0.046	
Gaia DR3 792284031455893504	0.779	-9.753	0.037	0.000	0.006				
Gaia DR3 782803458087840000	2.502	0.814	-27.082	0.022	0.000	0.000	0.641	0.040	
Gaia DR3 782803389372882944	0.586	-27.723	0.033	0.000	0.097				
Gaia DR3 783007245705158400	13.815	0.649	-15.864	0.026	0.198	0.039	-0.437	0.051	
Gaia DR3 783007280064896128	0.591	-15.427	0.044	0.000	0.119				
Gaia DR3 822171987312735232	9.197	0.594	11.361	0.025	0.017	0.035	-0.189	0.253	
Gaia DR3 822172227830881408	0.311	11.550	0.252	0.000	0.908				
Gaia DR3 4418851263967008000	4.959	0.900	-6.898	0.022	0.000	0.051	-0.056	0.298	

Table 7 continued

Table 7 (continued)

Gaia DR3 4418850890305439872	0.225	-6.842	0.297	0.000	1.656		
Gaia DR3 1500748301498613248	3.249	1.626	-15.431	0.104	0.000	2.872	1.014
Gaia DR3 1500748198419397760	0.519	-16.445	0.101	0.000	0.000		0.145
Gaia DR3 1500827225817637504	3.446	0.177	-9.750	0.211	0.000	0.866	-0.447
Gaia DR3 1500826882220275712	0.139	-9.303	0.283	0.000	0.412		
Gaia DR3 1508340498008710784	8.226	1.277	-36.941	0.019	0.055	0.000	-0.502
Gaia DR3 1508340532367957376	0.528	-36.439	0.100	0.000	0.049		0.102
Gaia DR3 1466043419558823296	15.233	0.639	-2.255	0.037	0.000	0.131	-0.204
Gaia DR3 1466040395901846528	0.446	-2.051	0.070	0.000	0.183		
Gaia DR3 1460823041429644160	1.987	0.939	-8.137	0.010	0.069	0.078	0.414
Gaia DR3 1460823041429644032	0.620	-8.551	0.055	0.000	0.132		
Gaia DR3 1460984429120711808	1.519	0.858	-54.308	0.028	0.080	0.077	0.082
Gaia DR3 1460984429120711552	0.717	-54.390	0.074	0.000	0.159		
Gaia DR3 1461182444292609536	3.719	1.105	-13.677	0.024	0.007	0.073	-0.489
Gaia DR3 1461182684811100288	1.084	-13.188	0.018	0.038	0.048		
Gaia DR3 1469596938060496768	3.735	0.617	-48.401	0.156	0.000	0.043	-0.352
Gaia DR3 1469596938060497024	0.508	-48.049	0.036	0.089	0.349		
Gaia DR3 1469606455707961088	19.502	0.997	-12.462	0.019	0.010	0.058	-0.185
Gaia DR3 1469606283909297152	0.905	-12.277	0.018	0.080	0.045		
Gaia DR3 1475867727751525632	5.102	0.483	2.719	0.063	0.000	0.559	-0.236
Gaia DR3 1475867727751525504	0.279	2.955	0.240	0.000	1.262		
Gaia DR3 1459718891236328192	21.967	0.664	-20.889	0.012	0.076	0.145	-0.019
Gaia DR3 1459715764500136192	0.449	-20.870	0.064	0.000	0.186		
Gaia DR3 1476646250703083264	4.150	0.545	-10.535	0.056	0.000	0.000	-0.172
Gaia DR3 1476646285062821888	0.445	-10.363	0.073	0.000	0.337		
Gaia DR3 1476762627137479552	15.898	0.540	-1.850	0.058	0.000	0.000	-0.512
Gaia DR3 1476768433933264128	0.320	-1.338	0.141	0.000	0.211		
Gaia DR3 1593535881608710784	8.875	0.366	-0.661	0.065	0.000	0.000	0.027
Gaia DR3 1593537084199554560	0.357	-0.688	0.082	0.226	0.820		
Gaia DR3 1604175580752706432	2.686	1.015	-14.773	0.028	0.000	0.027	1.616
Gaia DR3 1604175477673086592	0.224	-16.389	0.460	0.000	0.395		
Gaia DR3 1590641417247939584	9.153	0.882	-6.554	0.042	0.000	0.050	0.252
Gaia DR3 1590641417247939328	0.766	-6.806	0.050	0.000	0.049		
Gaia DR3 4008273560363584768	10.198	0.371	5.286	0.105	0.000	0.558	1.848
Gaia DR3 4008273903960972416	0.160	3.438	0.749	0.000	1.791		
Gaia DR3 4008339427981993088	3.022	1.360	-12.339	0.036	0.000	0.087	0.238
Gaia DR3 4008339359262516224	0.679	-12.577	0.072	0.000	0.106		
Gaia DR3 4008743086188165248	11.678	0.606	-9.820	0.061	0.000	0.033	0.804
Gaia DR3 4008743154907642496	0.272	-10.624	0.338	0.000	0.596		
Gaia DR3 63739517993652864	4.950	0.684	-5.527	0.043	0.000	0.149	0.173
Gaia DR3 63739311835222784	0.676	-5.700	0.043	0.000	0.062		
Gaia DR3 6246952489482132736	13.867	0.962	9.765	0.027	0.000	0.028	-0.017
Gaia DR3 6246952592561351040	0.755	9.782	0.027	0.020	0.013		
Gaia DR3 1534089651581519488	18.119	0.903	3.515	0.026	0.000	0.016	-0.433
Gaia DR3 1534086421765263360	0.450	3.948	0.077	0.000	0.126		
Gaia DR3 1535360373488627200	17.981	1.314	-11.257	0.019	0.055	0.053	-0.270
Gaia DR3 1535360343424477440	1.092	-10.987	0.024	0.026	0.038		
Gaia DR3 1538594140265624064	1.287	0.977	-33.814	0.027	0.000	0.003	-0.886
Gaia DR3 1538594144560846848	0.639	-32.928	0.047	0.000	0.008		
Gaia DR3 1533327415144066432	5.666	0.872	-2.323	0.043	0.000	0.022	-0.172
Gaia DR3 1533327483863543296	0.700	-2.151	0.053	0.000	0.054		
Gaia DR3 1549029953017127808	1.932	0.929	9.866	0.037	0.000	0.023	1.070
Gaia DR3 1549030056098162176	0.860	8.796	0.040	0.000	0.075		
Gaia DR3 5477438450481258240	2.497	0.878	8.484	0.030	0.000	0.000	-0.185
							0.049

Table 7 continued

Table 7 (continued)

Gaia DR3 5477438454778666624	0.759	8.669	0.039	0.000	0.113		
Gaia DR3 1305035575352515840	3.031	0.484	7.595	0.031	0.000	0.011	-0.049 0.084
Gaia DR3 1305036228187622912	0.277	7.644	0.078	0.000	0.099		
Gaia DR3 1302543326089734144	14.656	0.998	-63.058	0.036	0.000	0.025	-0.049 0.052
Gaia DR3 1302449489644570496	0.848	-63.009	0.038	0.000	0.006		
Gaia DR3 1320379809873587968	1.716	1.007	-129.817	0.039	0.000	0.004	0.040 0.053
Gaia DR3 1320379741154111104	0.807	-129.857	0.036	0.000	0.005		
Gaia DR3 1321929846390816640	36.773	0.793	-9.730	0.022	0.016	0.033	0.250 0.053
Gaia DR3 1321930842823231616	0.603	-9.980	0.048	0.000	0.014		
Gaia DR3 1555391177542038400	8.101	1.089	-4.412	0.017	0.045	0.029	-0.119 0.079
Gaia DR3 1555388222603962752	0.398	-4.293	0.077	0.000	0.199		
Gaia DR3 1580778076392231424	10.792	0.641	-26.414	0.056	0.000	0.145	-0.142 0.085
Gaia DR3 1580778213830765824	0.527	-26.272	0.064	0.000	0.154		
Gaia DR3 76974648692629376	1.397	0.483	45.236	0.032	0.025	0.019	-0.100 0.064
Gaia DR3 76974751771844096	0.422	45.336	0.055	0.000	0.011		
Gaia DR3 1381408782592655616	2.363	0.812	-4.565	0.040	0.000	0.091	0.442 0.066
Gaia DR3 1381455722290898176	0.635	-5.007	0.053	0.000	0.045		
Gaia DR3 1391176092275606656	1.832	1.079	-16.754	0.027	0.000	0.000	-0.566 0.092
Gaia DR3 1391176092275606528	0.663	-16.188	0.088	0.000	0.137		
Gaia DR3 1331462302965590400	3.889	1.283	-23.271	0.052	0.528	0.434	0.986 0.082
Gaia DR3 1331462302965590144	0.472	-24.257	0.064	0.000	0.120		
Gaia DR3 1332438183958298496	5.681	0.968	-22.793	0.040	0.000	0.317	-0.688 0.045
Gaia DR3 1332438188254551808	0.933	-22.105	0.021	0.014	0.075		
Gaia DR3 1332473922382951424	0.653	0.634	-12.902	0.039	0.165	0.593	-0.310 0.409
Gaia DR3 1332473922382506624	0.529	-12.592	0.407	0.000	0.667		
Gaia DR3 4572807566444752128	0.782	0.804	27.156	0.022	0.000	0.000	0.108 0.093
Gaia DR3 4572807566444751616	0.317	27.048	0.090	0.000	0.119		
Gaia DR3 1397692244857993728	2.797	0.713	-34.692	0.033	0.000	0.000	0.838 0.042
Gaia DR3 1397692279217731456	0.693	-35.530	0.026	0.994	0.327		
Gaia DR3 1403853152105526272	4.334	0.375	10.955	0.056	0.000	0.000	0.015 0.087
Gaia DR3 1403852430551017984	0.297	10.940	0.066	0.797	6.370		
Gaia DR3 1407596954838724864	1.159	0.726	-9.612	0.042	0.000	0.043	-0.019 0.086
Gaia DR3 1407596954838646912	0.701	-9.593	0.075	0.000	0.044		
Gaia DR3 1407786689313958784	1.351	0.636	-54.605	0.105	0.000	0.000	-0.749 0.149
Gaia DR3 1407786654954220160	0.472	-53.856	0.106	0.000	0.125		
Gaia DR3 2076871091425586944	3.106	0.849	-25.476	0.026	0.000	0.000	0.198 0.033
Gaia DR3 2076871091425583232	0.785	-25.674	0.021	0.004	0.083		
Gaia DR3 576837717289109248	1.839	1.060	40.557	0.027	0.000	0.036	-0.290 0.038
Gaia DR3 576837717289109504	0.886	40.847	0.027	0.000	0.031		
Gaia DR3 4819204205221996160	2.454	0.692	44.578	0.062	0.000	0.079	-0.347 0.098
Gaia DR3 4819204200922632064	0.626	44.925	0.076	0.000	0.105		
Gaia DR3 3221172596658836736	36.462	0.699	75.807	0.034	0.000	0.047	-0.059 0.059
Gaia DR3 3221172729803195904	0.552	75.866	0.048	0.000	0.044		
Gaia DR3 1247610934890765312	0.720	0.791	6.407	0.048	0.000	0.099	-0.794 0.059
Gaia DR3 1247610934890765184	0.721	7.201	0.034	0.000	0.100		
Gaia DR3 1240752559313435520	3.125	0.777	-18.826	0.026	0.000	0.019	0.004 0.072
Gaia DR3 1240752559313476224	0.379	-18.830	0.067	0.000	0.072		
Gaia DR3 2116748247853607168	1.402	1.145	-8.060	0.070	0.000	0.000	-0.562 0.075
Gaia DR3 2116748243555689728	0.889	-7.498	0.028	0.000	0.000		
Gaia DR3 2116892318236994816	1.981	1.119	7.002	0.038	0.000	0.000	0.056 0.050
Gaia DR3 2116892313938771584	0.738	6.946	0.033	0.000	0.000		
Gaia DR3 2078886290079138560	1.333	1.004	-10.477	0.037	0.000	0.071	-0.246 0.069
Gaia DR3 2078886285778453632	0.917	-10.231	0.058	0.000	0.000		
Gaia DR3 1022456139210632064	0.108	0.590	11.460	0.026	0.589	0.000	0.559 0.043

Table 7 continued

Table 7 (continued)

Gaia DR3 1022456104850892928	0.580	10.901	0.034	0.000	0.000		
Gaia DR3 1029034448560364928	1.641	0.735	-24.567	0.118	0.000	0.000	-0.243 0.123
Gaia DR3 1029034448560364800	0.605	-24.324	0.035	0.000	0.000		
Gaia DR3 145203159127518336	43.714	0.808	17.197	0.058	0.052	0.075	0.081 0.081
Gaia DR3 145203811962545152	0.608	17.116	0.056	0.000	0.219		
Gaia DR3 152109054223716480	7.241	0.561	16.995	0.067	0.000	0.535	0.570 0.258
Gaia DR3 152108882425024128	0.258	16.425	0.249	0.000	0.413		
Gaia DR3 157039397504919168	0.623	1.555	30.297	0.064	0.000	0.305	-0.160 0.068
Gaia DR3 157039401801742976	0.988	30.457	0.024	0.000	0.000		
Gaia DR3 880933187236449792	45.245	0.990	-11.592	0.030	0.000	0.023	0.233 0.051
Gaia DR3 880933702632515840	0.669	-11.825	0.041	0.000	0.076		
Gaia DR3 5262754514488149632	15.417	1.406	1.239	0.027	0.063	0.081	-0.049 0.048
Gaia DR3 5262754273969986688	1.371	1.288	0.040	0.053	0.106		Yes
Gaia DR3 5268812686118172928	10.585	1.149	29.892	0.099	0.000	0.000	-0.180 0.107
Gaia DR3 5268812853620242048	1.112	30.072	0.041	0.000	0.000		
Gaia DR3 3605478986040028544	14.727	1.776	-31.166	0.029	0.049	0.163	-1.201 0.467
Gaia DR3 3605479020399765888	0.210	-29.965	0.466	0.000	2.162		
Gaia DR3 425040000962559616	0.079	1.054	9.130	0.042	0.000	0.301	0.244 0.059
Gaia DR3 425040000962497792	0.598	8.886	0.041	0.121	0.184		
Gaia DR3 4676751272565519872	1.718	0.443	-19.618	0.118	0.000	0.000	0.999 0.578
Gaia DR3 4676751341284996480	0.390	-20.617	0.566	0.000	0.522		
Gaia DR3 4669281259285732480	21.759	1.119	35.245	0.031	0.000	0.000	-0.113 0.045
Gaia DR3 4669281121846284160	1.018	35.358	0.033	0.000	0.000		
Gaia DR3 3265508650701713664	2.612	1.030	29.067	0.050	0.000	0.107	-0.211 0.058
Gaia DR3 3265508685061451648	1.018	29.278	0.029	0.000	0.019		
Gaia DR3 3266980170921153920	6.036	0.879	88.594	0.234	0.000	0.000	-0.287 0.240
Gaia DR3 3266980243936341248	0.417	88.881	0.055	0.000	0.054		
Gaia DR3 4757024829820200704	5.504	0.974	-6.794	0.056	0.000	0.000	0.633 0.084
Gaia DR3 4757026135488693760	0.676	-7.427	0.062	0.000	0.000		
Gaia DR3 3609320267350909696	10.223	0.787	-56.802	0.045	0.000	0.002	0.353 0.055
Gaia DR3 3609320503573212416	0.743	-57.155	0.032	0.000	0.086		
Gaia DR3 1652245748082610304	1.342	0.961	54.463	0.032	0.000	0.041	0.348 0.059
Gaia DR3 1652245748082125440	0.557	54.115	0.049	0.000	0.000		
Gaia DR3 2104999343337767424	19.187	0.953	-18.034	0.025	0.000	0.000	0.164 0.048
Gaia DR3 2104998900960077056	0.738	-18.198	0.041	0.000	0.134		
Gaia DR3 3922083599776523392	1.955	0.772	-11.732	0.038	0.000	0.035	-0.581 0.215
Gaia DR3 3922083599776523520	0.429	-11.151	0.212	0.000	0.632		
Gaia DR3 3928893253244519168	6.337	1.197	-2.068	0.026	0.076	0.092	-0.109 0.182
Gaia DR3 3928893253244519552	0.408	-1.959	0.180	0.000	0.578		
Gaia DR3 3929154078017979264	2.895	1.166	-36.255	0.036	0.000	0.093	-0.365 0.100
Gaia DR3 3929154078017979008	0.642	-35.890	0.093	0.000	0.313		
Gaia DR3 3936935283153115008	38.482	1.309	2.580	0.043	0.000	0.131	-0.120 0.078
Gaia DR3 3936947278997113216	0.580	2.700	0.065	0.000	0.365		
Gaia DR3 3958567766407880576	0.909	0.573	-14.002	0.014	0.110	0.048	0.682 0.024
Gaia DR3 3958567766407880704	0.444	-14.684	0.019	0.110	0.044		Yes
Gaia DR3 690460424271103360	22.780	0.920	-32.999	0.031	0.000	0.054	-0.126 0.062
Gaia DR3 690272545221668096	0.606	-32.873	0.054	13.924	0.925		
Gaia DR3 694284491350980864	3.288	0.636	-2.491	0.031	0.000	0.062	-0.276 0.100
Gaia DR3 694284628789933568	0.318	-2.215	0.095	0.000	0.092		
Gaia DR3 2164378370045365376	1.115	0.413	6.758	0.053	0.000	0.147	0.098 0.070
Gaia DR3 2164331434639561088	0.377	6.660	0.046	0.028	0.200		
Gaia DR3 678053947384823936	1.619	0.876	-2.451	0.019	0.014	0.019	-1.144 0.144
Gaia DR3 678053878665346816	0.421	-1.307	0.143	0.000	1.342		
Gaia DR3 678095763181573632	1.901	0.876	-8.700	0.019	0.018	0.203	-0.298 0.029
							Yes

Table 7 continued

Table 7 (continued)

Gaia DR3 678095763182104704	0.749	-8.402	0.022	0.051	0.027		
Gaia DR3 676003255114571008	1.101	0.730	46.643	0.027	0.000	0.000	-0.324 0.038
Gaia DR3 676003255114571264	0.594	46.967	0.027	0.006	0.085		
Gaia DR3 712074211531234816	23.757	0.397	23.960	0.061	0.000	0.023	-0.278 0.101
Gaia DR3 712024802229009920	0.326	24.238	0.081	0.000	0.059		
Gaia DR3 705170274943504000	3.125	1.424	7.595	0.028	0.000	0.073	0.040 0.036
Gaia DR3 705170309303241984	1.103	7.555	0.023	0.000	0.016		
Gaia DR3 705997794881180544	2.148	1.024	10.026	0.030	0.000	0.042	0.905 0.057
Gaia DR3 705997794881180672	0.892	9.121	0.049	0.000	0.016		
Gaia DR3 2462426800883134336	0.996	1.233	-8.747	0.026	0.000	0.000	0.072 0.035
Gaia DR3 2462426800883156480	0.599	-8.819	0.024	0.000	0.000		
Gaia DR3 2475292457022466048	4.118	0.946	18.337	0.111	0.000	0.319	0.389 0.402
Gaia DR3 2475292530037116288	0.652	17.948	0.386	0.000	0.335		
Gaia DR3 923398868922049792	1.639	0.783	16.981	0.038	0.000	0.026	-0.402 0.066
Gaia DR3 923398864626108416	0.644	17.383	0.054	0.000	0.000		
Gaia DR3 926109886638467840	0.697	0.558	93.745	0.047	0.000	0.135	0.436 0.083
Gaia DR3 926109886638467968	0.483	93.309	0.069	0.000	0.173		
Gaia DR3 3686261307923490688	4.502	0.469	41.577	0.038	0.000	0.060	-0.177 0.084
Gaia DR3 3686259727375524864	0.301	41.754	0.075	0.000	0.045		
Gaia DR3 1434064639260540288	1.857	1.299	-2.610	0.070	0.000	0.000	0.187 0.076
Gaia DR3 1434064669325509760	0.862	-2.797	0.030	0.000	0.000		
Gaia DR3 1427740214018187392	2.646	0.618	-31.220	0.058	0.000	0.125	-0.691 0.172
Gaia DR3 1427740214018187648	0.372	-30.529	0.162	0.000	0.230		
Gaia DR3 4763619318293079168	6.382	0.937	31.561	0.021	0.000	0.000	-0.180 0.075
Gaia DR3 4763618910272182400	0.348	31.741	0.072	0.000	0.000		
Gaia DR3 2086713404118555648	0.442	0.974	-29.198	0.032	0.000	0.000	0.382 0.043
Gaia DR3 2086713404118555520	0.863	-29.580	0.029	0.000	0.000		
Gaia DR3 5496774878580968832	21.476	0.563	23.446	0.047	0.000	0.000	-0.046 0.097
Gaia DR3 5496779998182670976	0.405	23.492	0.085	0.000	0.000		
Gaia DR3 162758236656524416	13.291	0.696	17.969	0.047	0.309	1.291	-0.456 0.078
Gaia DR3 162757545164429696	0.683	18.425	0.062	1.186	1.353		Yes
Gaia DR3 1444305829863259648	6.749	0.791	-5.889	0.019	0.043	0.106	0.349 0.038
Gaia DR3 1444305937237949184	0.612	-6.238	0.033	0.000	0.000		
Gaia DR3 1448490437975655552	35.425	1.323	-36.479	0.028	0.031	0.163	0.194 0.046
Gaia DR3 1448490369254832896	1.099	-36.673	0.036	0.000	0.070		
Gaia DR3 1456403004684961536	0.600	0.398	-16.261	0.065	0.000	0.012	0.436 0.089
Gaia DR3 1456403004684961408	0.394	-16.697	0.061	0.000	0.062		
Gaia DR3 2129540099271049216	0.786	0.919	-6.230	0.038	0.000	0.070	1.331 0.050
Gaia DR3 2129540103571086592	0.864	-7.561	0.032	0.000	0.362		
Gaia DR3 2130903223113004032	4.305	1.185	-5.509	0.035	0.000	0.000	0.210 0.056
Gaia DR3 2130903047014230528	0.957	-5.719	0.044	0.000	0.031		
Gaia DR3 832823020875083776	2.767	0.601	-2.311	0.029	0.095	0.102	0.320 0.101
Gaia DR3 832823025170612736	0.361	-2.631	0.097	0.000	0.272		
Gaia DR3 839281109796627968	17.651	0.766	3.133	0.020	0.043	0.035	0.043 0.030
Gaia DR3 839281796991751168	0.737	3.090	0.022	0.065	0.064		Yes
Gaia DR3 839567326416583552	2.362	0.733	-20.752	0.041	0.000	0.073	0.347 0.070
Gaia DR3 839567326416583808	0.336	-21.099	0.057	0.085	0.118		
Gaia DR3 6236104295448198272	3.850	0.561	-2.831	0.060	0.000	0.000	-0.679 0.195
Gaia DR3 6236103917491077120	0.418	-2.152	0.186	0.000	0.842		
Gaia DR3 6041787193156436992	0.739	0.390	-38.218	0.086	0.000	0.000	0.157 0.585
Gaia DR3 6041787193156437248	0.305	-38.375	0.579	0.000	0.000		
Gaia DR3 6044225119671978752	11.803	0.596	-2.069	0.061	0.000	0.000	-0.104 0.085
Gaia DR3 6044230960827500032	0.526	-1.965	0.059	0.000	0.000		
Gaia DR3 972821779152541824	19.865	0.601	64.726	0.031	0.000	0.050	-0.160 0.048

Table 7 continued

Table 7 (continued)

Gaia DR3 972815560039899264	0.546	64.886	0.037	0.000	0.037		
Gaia DR3 988478859091454976	4.261	0.698	41.484	0.044	0.000	0.059	-0.661 0.141
Gaia DR3 988478957873964544	0.417	42.145	0.134	0.000	0.118		
Gaia DR3 134816244579883008	3.828	0.752	-3.744	0.041	0.000	0.074	0.050 0.062
Gaia DR3 134816244579883776	0.674	-3.794	0.046	0.000	0.072		
Gaia DR3 1159502498311670144	3.022	0.821	23.549	0.022	0.000	0.027	0.126 0.042
Gaia DR3 1159502154714284544	0.489	23.423	0.036	0.000	0.032		
Gaia DR3 4665709113509264768	5.923	0.783	22.638	0.018	0.058	0.000	0.173 0.046
Gaia DR3 4665710629633988736	0.560	22.465	0.042	0.000	0.000		
Gaia DR3 1172915990414659328	24.684	0.885	-17.931	0.023	0.000	0.044	0.043 0.033
Gaia DR3 1172920487244742912	0.852	-17.974	0.023	0.000	0.051		
Gaia DR3 935566717429616000	8.615	0.980	38.446	0.016	0.128	0.049	-0.617 0.054 Yes
Gaia DR3 935566511271187072	0.452	39.063	0.052	0.935	52.862		
Gaia DR3 933708229245319552	2.249	0.321	4.559	0.074	0.000	0.037	0.106 0.113
Gaia DR3 933708164821511424	0.270	4.453	0.086	0.000	0.012		

<sup>a</sup> Sky-plane physical separation from K. El-Badry et al. (2021).

<sup>b</sup> Stellar mass based on the mass-magnitude relation derived by K.-H. Chae (2023).

<sup>c</sup> Radial velocity stored in the APOGEE parameter `VHELIO_AVG` (the barycentric velocity) which represents a signal-to-noise weighted average if multiple visits took place (i.e., the APOGEE parameter `NVISITS` > 1): When multiple values from multiple observations (note here that each observation may have multiple visits) are reported, the given value refers to the error-weighted mean  $\mu$  calculated by  $\mu = \sum(\text{RV}_i / \sigma_i^2) / \sum(1 / \sigma_i^2)$ .

<sup>d</sup> Reported error: When multiple values from multiple observations are reported, the given value refers to the error of  $\mu$  calculated by  $\sigma_\mu = 1 / \sqrt{\sum(1 / \sigma_i^2)}$ .

<sup>e</sup> This value refers to the standard deviation of multiple values from multiple observations. It is set to zero when a single observation was made.

<sup>f</sup> The APOGEE parameter `VSCATTER` which represents the scatter from multiple visits of an observation. It is set to zero when an observation consists of a single visit. When multiple values of `VSCATTER` from observations are available, the maximum value is given.

<sup>g</sup> Relative radial velocity  $v_r$  ( $\equiv \text{RV}_A - \text{RV}_B$ ) where  $\text{RV}_A$  and  $\text{RV}_B$  refer respectively to the first and second values.

<sup>h</sup> Whether multiple observations were made at multiple epochs.

Table 8. Summary of wide binaries with multiple radial velocities of both components from multi-epoch APOGEE observations

Star A	RV <sup>a</sup> [km s <sup>-1</sup> ]	Err <sup>b</sup>	Scatt <sup>c</sup>	Star B	RV <sup>a</sup> [km s <sup>-1</sup> ]	Err <sup>b</sup>	Scatt <sup>c</sup>
Gaia DR3 2642922251741817216	23.611124	0.04403066	0.04110121	2642922286101533952	23.745401	0.04636222	0.06235123
	23.493046	0.03530691	0.04366402		23.661783	0.03730566	0.02735676
Gaia DR3 2501323948860951296	-26.34998	0.03360082	0.00961134	2501325525113734912	-26.389238	0.04771343	0.11454166
	-26.28739	0.04346129	0.06616001		-26.260921	0.03940159	0.04780705
Gaia DR3 217107577453306112	22.248499	0.02819021	0.07399079	217107607515576704	21.878296	0.03318193	0.05599995
	22.275375	0.02912341	0.144448		21.788877	0.02936134	0.
Gaia DR3 3961746072270936320	-45.91673	0.03888413	0.	3961745217573223296	-45.767345	0.05168254	0.
	-45.911835	0.05633869	0.		-45.684467	0.05476467	0.03869113
	-45.86499	0.04045845	0.06876723		-45.90399	0.04622763	0.01500438
	-45.8177	0.03833721	0.05585103		-45.69478	0.08768474	0.12935062
	-45.823917	0.06022181	0.15365449		-45.790802	0.06783935	0.05524765
	-45.71305	0.05185273	0.06499686		-45.664474	0.04946134	0.
	-45.744324	0.0405033	0.		-45.800285	0.05546138	0.01956754
	-45.77147	0.04337924	0.01045496		-45.666336	0.05314275	0.02631607
	-45.743183	0.04535097	0.06701745		-45.732433	0.03973199	0.
	-45.965115	0.03278913	0.		-45.759113	0.05460643	0.06531424

Table 8 continued

**Table 8** (*continued*)

	-45.867214	0.04078658	0.00449147				
Gaia DR3 2581883413481515008	-14.654112	0.02970796	0.	2581859911420471808	-14.30785	0.04154328	0.
	-14.7650795	0.03625005	0.		-14.515479	0.05171923	0.
Gaia DR3 785716030026546688	-15.540678	0.04524035	0.03031975	785716682861545344	-15.415195	0.06123991	0.1664266
	-15.592761	0.04024156	0.08631156		-15.533735	0.05448572	0.01872353
Gaia DR3 1461182444292609536	-13.681904	0.03039815	0.01888097	1461182684811100288	-13.209225	0.02909379	0.04755092
	-13.66857	0.04013753	0.07308564		-13.213476	0.02948592	0.01699376
					-13.130007	0.03311201	0.02252192
Gaia DR3 1469606455707961088	-12.468412	0.03486331	0.0247436	1469606283909297152	-12.182982	0.02783493	0.0102103
	-12.4709635	0.03095368	0.05807732		-12.376394	0.03245912	0.04527421
	-12.447786	0.03108544	0.00479869		-12.307321	0.03310763	0.00351568
Gaia DR3 1535360373488627200	-11.203867	0.02588832	0.01143761	1535360343424477440	-10.9632845	0.03258488	0.01365597
	-11.3142395	0.02703807	0.0534603		-11.014411	0.03550287	0.03829292
Gaia DR3 5262754514488149632	1.2070447	0.03156854	0.	5262754273969986688	1.3154067	0.04626257	0.
	1.3321234	0.05412297	0.08124872		1.2100439	0.07827925	0.10565944
Gaia DR3 3958567766407880576	-14.007257	0.03145121	0.0253697	3958567766407880704	-14.654441	0.05386632	0.
	-13.967669	0.03088553	0.0154797		-14.469742	0.05273892	0.0115321
	-13.915713	0.0328168	0.034364		-14.670951	0.05127405	0.02754166
	-13.89397	0.03500261	0.04774026		-14.732671	0.05338896	0.03030096
	-14.2029	0.03196205	0.		-14.631961	0.05492502	0.03866151
					-14.683698	0.0498655	0.
					-14.773074	0.05134532	0.00627914
					-14.874403	0.05639074	0.04404995
Gaia DR3 678095763181573632	-8.719339	0.02869016	0.20294154	678095763182104704	-8.34763	0.03163528	0.01059777
	-8.683017	0.02654715	0.		-8.449814	0.02956442	0.02662994
Gaia DR3 162758236656524416	18.270649	0.06570818	1.2907226	162757545164429696	19.58776	0.08644723	1.3527985
	17.651651	0.06742151	0.29228374		17.215908	0.08812028	1.2935578
Gaia DR3 839281109796627968	3.1859643	0.03458128	0.0264379	839281796991751168	3.1243968	0.03509628	0.0466863
	3.0797095	0.03401986	0.00547901		3.007658	0.03551762	0.06423731
	3.1357276	0.0380827	0.03508588		3.1594172	0.04301288	0.01149944
Gaia DR3 935566717429616000	38.319893	0.02177464	0.02721165	935566511271187072	38.15186	0.07279947	52.861546
	38.576614	0.0222188	0.04888935		40.022377	0.07470552	40.95351

<sup>a</sup> Reported radial velocity.<sup>a</sup> Reported error.<sup>c</sup> Reported value of VSCATTER.

## E. DESCRIPTION OF SPECKLE OAN-SPM OBSERVATIONS AND DATA REDUCTION

### E.1. Speckle observations at 2.1m telescope of the Observatorio Astronómico Nacional at Sierra de San Pedro Mártir (SPM), México.

Our main objective was a search of anomalies in either component of a given wide binary system, we aim to identify any component that exhibits a different structure from that of a normal star, meaning elongation, a comma like pattern or having another component. Speckle interferometry is a technique used in astronomy to overcome the limitations of atmospheric turbulence and obtain high-resolution images of astronomical objects. Using this technique at the 2.1m telescope, one can resolve binary stars with small separations up to  $0.05''$ . Speckle imaging with the 2.1 m telescope at OAN-SPM routinely covers targets from very bright stars down to  $R \approx 11$  mag, delivering contrast sensitivities of about  $\Delta m \approx 3$  mag at  $0.09''$  and up to  $\Delta m \approx 8$  mag at  $1.0''$ . For stars fainter than  $R \approx 11$  mag these contrast limits become difficult to achieve, whereas for brighter targets observed under excellent conditions, even higher contrasts can be obtained.

Observations were carried out with the 2.1 m telescope at the Observatorio Astronómico Nacional, San Pedro Mártir, Mexico, using the Berkut speckle interferometer. The instrument is equipped with an Andor iXon Ultra 888 EMCCD, delivering a plate scale of  $0.037''$  pixel $^{-1}$  and a maximum field of view of  $38''$ . Due to the small isoplanatic angle, systems with projected separations greater than  $8''$  were observed as separate pointings. Five observation runs were conducted between February 2024 and June 2025. The nights were characterized by predominantly variable

**Table 9.**

Run	Cubes $256 \times 256$	Cubes $512 \times 512$	Cubes $1024 \times 1024$
Feb-24	35		8
Sep-24	131	156	
Nov-24	70	139	1
Mar-25	149		
Jun-25	267	63	
Total	652	358	9

sky conditions, with seeing values typically ranging from  $0.5''$  to  $2''$ . Observations were performed through standard Johnson R and I filters. Individual speckle exposures had integration times between 10 and 30 ms, depending on target brightness. For each target, a sequence of 2000 frames was acquired to ensure sufficient statistical averaging. In total, we obtained 1019 data cubes for 391 wide binaries systems.

### E.2. Data Processing

We employed the same strategy for data acquisition as in [V. G. Orlov \(2021\)](#) and [A. Luna & V. G. Orlov \(2020\)](#). The necessary software and expertise are fully in place. Acquiring and processing speckle images requires thousands of short exposures (1–50 ms), with the exact exposure time determined by wavelength, telescope aperture, and atmospheric seeing. Typically, about 2000 short-exposure frames are needed to reconstruct a high-resolution image of an 11th-magnitude star in the I filter. The limiting observable magnitude is strongly constrained by atmospheric turbulence; thus, targets fainter than 11 mag can only be observed under good conditions, with seeing better than  $1.5''$ . A large number of frames is essential to achieve sufficient S/N, particularly at the smallest angular separations.

The first step of the data processing is the dark field correction of detected images  $i'_n(\vec{x})$ :

$$i_n(\vec{x}) = i'_n(\vec{x}) - \text{Dark}(\vec{x}), \quad (\text{E2})$$

where  $i_n(\vec{x})$  is the intensity at point  $(\vec{x})$  in the corrected image,  $\text{Dark}(\vec{x})$  is the average dark image captured with closed shutter. Then for each specklegram we calculate the following criteria:

$$Sh1_n = \left[ \sum i_n(\vec{x}) \right]^2 / \sum i_n^2(\vec{x}), \quad (\text{E3})$$

where the summations extend over the complete n-th specklegram ([D. W. McCarthy & M. L. Cobb 1986](#)). Speckle images are then ranked by their Sh1, where the "best" frames are those with the lowest Sh1. Two images in Figure 22 show the best (a) and worst (b) speckle images in a series of 2000 specklegrams.

### E.3. High-Resolution

The intensity distribution  $i_n(\vec{x})$  of the  $n$ 'th short exposure image (specklegram) can be described by:

$$i_n(\vec{x}) = o(\vec{x}) \otimes PSF_n(\vec{x}), \quad (\text{E4})$$

where  $\vec{x}$  is a 2D spatial coordinate,  $o(\vec{x})$  is the object intensity distribution,  $PSF_n(\vec{x})$  is the Point Spread Function for the  $n$ 'th specklegram and  $\otimes$  denotes convolution.

Then, applying the Fourier transform to equation E4

$$I_n(\vec{\omega}) = O(\vec{\omega}) \times OTF_n(\vec{\omega}), \quad (\text{E5})$$

where  $I_n(\vec{\omega})$  and  $O(\vec{\omega})$  are the Fourier transform of the image and object intensity distributions respectively, and  $OTF_n(\vec{\omega})$  is the Optical Transfer Function (OTF), which is the equivalent of the  $PSF$  in Fourier space. The  $OTF_n(\vec{\omega})$  is the same for all objects within the isoplanatic region. Equation E5 is the base for all high-resolution techniques. We applied various image processing techniques to reconstruct the power spectrum and obtain a high-resolution image of the star. This involves analyzing the speckle patterns in each short-exposure frame and combining them.

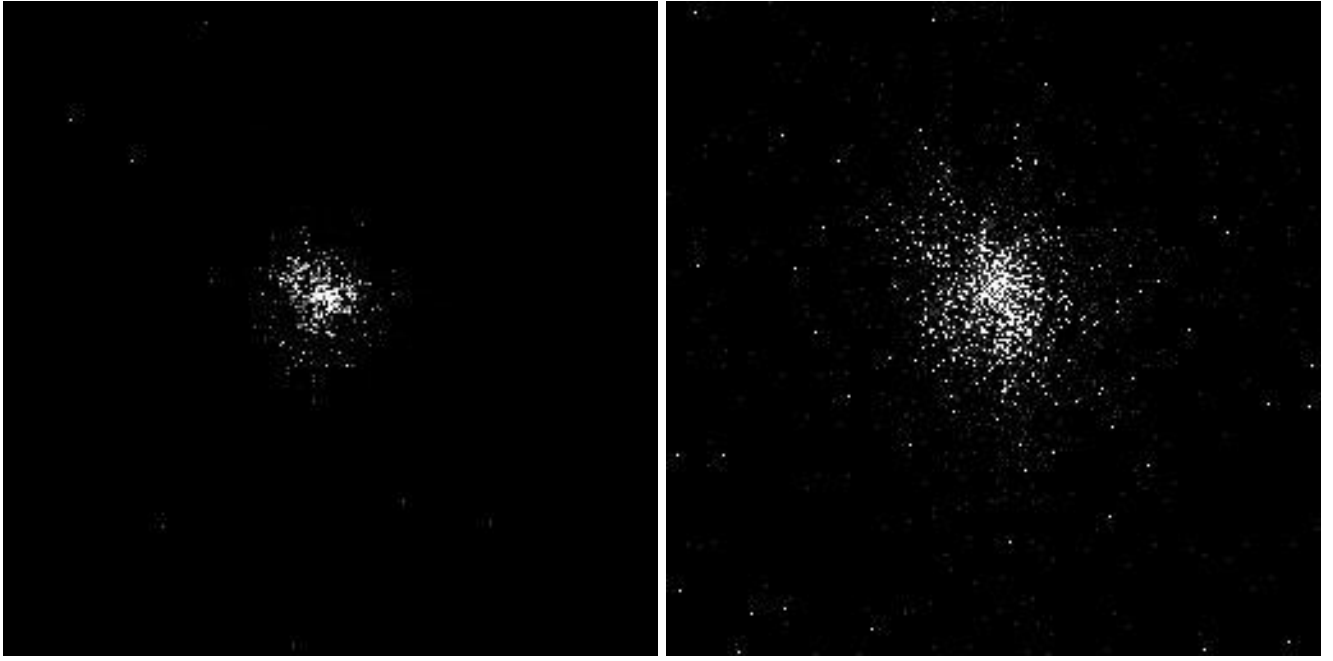


**Figure 22.** Data processing. Left to right: Best frame, worst speckle images in a series of 2000 specklegrams

#### E.4. Power Spectrum

The next step is to calculate the averaged power spectrum (PS) for each star:

$$PS(\vec{\omega}) = \langle |I_n(\vec{\omega})|^2 \rangle, \quad (\text{E6})$$

where  $\vec{\omega}$  is a spatial frequency and  $\langle \dots \rangle$  denotes averaging over all images.

In case of low light images, the averaged power spectrum can be expressed as (J. Kerp et al. 1992):

$$PS(\vec{\omega}) = P(\vec{\omega}) \cdot |G(\vec{\omega})|^2 + q |G(\vec{\omega})|^2, \quad (\text{E7})$$

where  $P(\vec{\omega})$  is the unshifted estimation of the power spectrum,  $q$  is some constant,  $|G(\vec{\omega})|^2$  is the power spectrum of the photon event shape function also known as photon bias. The photon bias  $|G(\vec{\omega})|^2$  can be determined as the normalized power spectrum of the night sky. The  $|G(\vec{\omega})|^2$  is constant in Y direction for this camera. Thus, it can be determined directly from  $PS(\vec{\omega})$  (Figure 23, (a)) by analysis of its part beyond the cut-off frequency of telescope. The unshifted power spectrum of specklegrams  $P(\mathbf{f})$  shown in Figure 23 (b). Therefore, it can be presented as:

$$P(\vec{\omega}) = |O(\vec{\omega})|^2 \langle |S_n(\vec{\omega})|^2 \rangle, \quad (\text{E8})$$

where  $|O(\vec{\omega})|^2$  power spectrum of the object,  $\langle |S_n(\vec{\omega})|^2 \rangle$  is the speckle interferometric transfer function. The speckle interferometric transfer function can be obtained by observing of a reference star or one can construct universal synthetic speckle interferometric transfer function (A. Tokovinin et al. 2010). Since we are concerned only with the presence or absence of a close stellar component, this information can be obtained directly from  $P(\vec{\omega})$  without requiring the speckle interferometric transfer function. In particular, we calculated the high resolution autocorrelation function in polar coordinates  $ACF_p$ :

$$ACF_p(\rho, \theta) = \text{const} \int_0^\infty \int_0^{2\pi} \cos(2\pi r \rho \cos(\theta - \phi)) P(r, \phi) W(r, \phi) r dr d\phi, \quad (\text{E9})$$

where  $W(r, \phi)$  is the window which excludes part of  $P(r, \phi)$  beyond the cut-off frequency of telescope  $f_T$  and for frequencies lower atmospheric cutoff  $f_A$ . Also taking in to account central symmetry of  $P(r, \phi)$  equation E9 can be rewritten as:

$$ACF_p(\rho, \theta) = \text{const} \int_{f_A}^{f_T} \int_0^\pi \cos(2\pi r \rho \cos(\theta - \phi)) P(r, \phi) r dr d\phi. \quad (\text{E10})$$

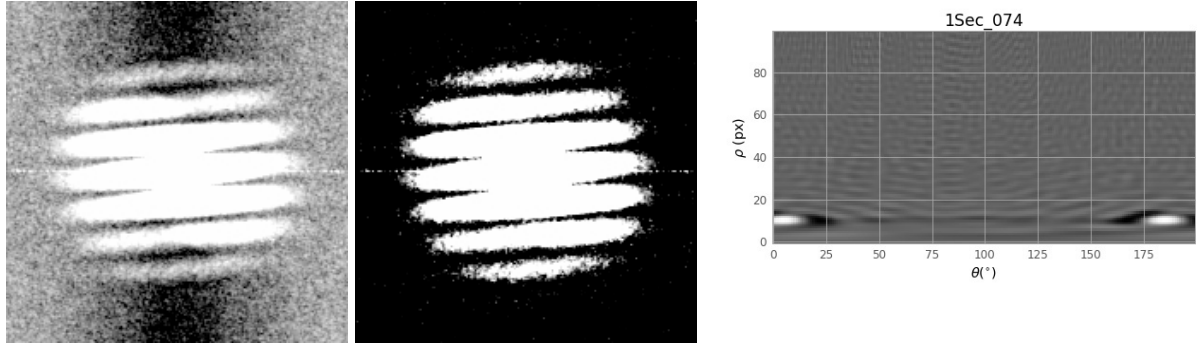


**Figure 23.** Power Spectrum of a close binary star before photon bias correction (a) and after correction (b). The High resolution ACF in polar coordinates (c). Separation  $0.3''$ .

A star has a component if the high-resolution  $ACF_p$  has a pronounced maximum.  $ACF_p$  allows finding the component even when the power spectrum is distorted by vibrations and strong aberrations of the telescope (V. G. Orlov 2021). One example of  $ACF_p$  is shown in figure 23 (c).

#### E.5. Speckle Holography

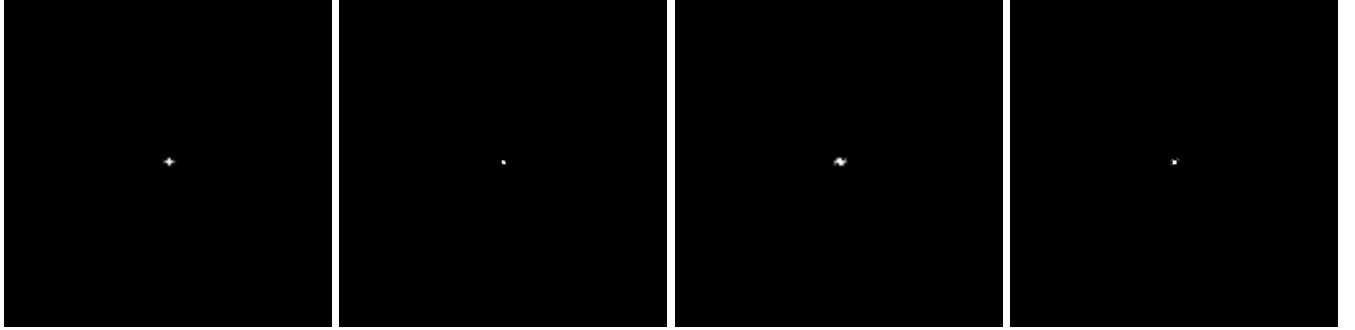


**Figure 24.** The typical wide binary system, composed of Gaia DR3 1172915990414659328 ( $G = 9.2$ ) and Gaia DR3 1172920487244742912 ( $G = 9.4$ ). (a) High-resolution autocorrelation of Gaia DR3 1172915990414659328. (b) High-resolution speckle holography image of Gaia DR3 1172915990414659328. (c) High-resolution autocorrelation of Gaia DR3 1172920487244742912. (d) High-resolution speckle holography image of Gaia DR3 1172920487244742912.

For most wide binaries we found no hidden stellar components (Figure 24). However, during data processing we identified several interesting systems — for example, Gaia DR3 4493544185516358656, which turned out to be a triple star system (Fig. 25). To investigate such cases in more detail, we applied speckle holography to the entire dataset. The method can be summarized as follows:

If one has a point source  $O^r(\vec{x}) = \delta(\vec{x} = \vec{x}^r)$  inside this area, the equation E5 for this star becomes:

$$I_n^r(\vec{\omega}) = OTF_n(\vec{\omega}). \quad (\text{E11})$$

Substitution of equation E11 into equation E5 gives:

$$I_n(\vec{\omega}) = O(\vec{\omega}) \times I_n^r(\vec{\omega}). \quad (\text{E12})$$

The Fourier transform of the object intensity distributions can be estimated by :

$$O(\vec{\omega}) = \frac{\langle I_n(\vec{\omega}) I_n^*(\vec{\omega}) \rangle}{\langle |I_n^r(\vec{\omega})|^2 \rangle}, \quad (\text{E13})$$

where  $\langle \dots \rangle$  means averaging over all images and  $*$  is the complex conjugation. Finally, the object intensity distributions can be obtained by the inverse Fourier transform.

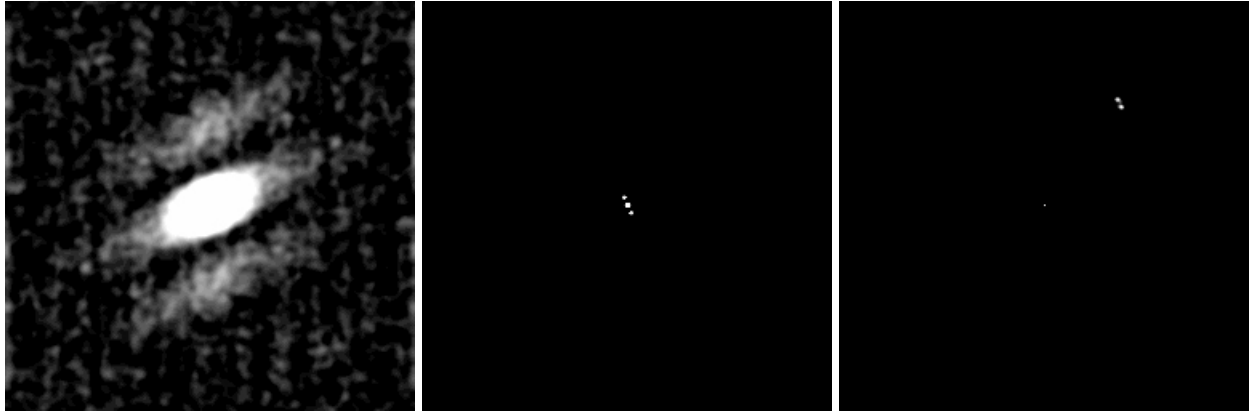


**Figure 25.** The triple system ABC, composed of Gaia DR3 4493544185516358656 ( $G = 12.86$ ), Gaia DR3 4493544082437142400 ( $G = 13.26$ ), and Gaia DR3 4493544082437142784 ( $G = 14.13$ ). (a) Power spectrum of subsystem BC. (b) High-resolution autocorrelation of subsystem BC. (c) High-resolution speckle holography image. It was derived from Speckle Interferometry (A. Labeyrie 1970), being the main difference that speckle holography works to remove atmospheric aberrations from each short exposure image and the phase information is kept. The separation between components B and C is  $0.1''$  (8 pc).

#### E.6. detection limit

The detection limit describes how faint a companion star could be and still be identifiable in the data. It is defined by the minimum signal-to-noise ratio needed to separate a real signal from random noise. In practice, astronomers usually adopt a threshold of  $5\sigma$ , which makes the chance of mistaking noise for a real star well below one percent. Sometimes a lower threshold of  $3\sigma$  is used, but this is risky. At this level, it is rare, but possible, to detect spurious companions caused by noise (A. Tokovinin et al. 2010).

At large separations from the primary star (more than about three times the seeing disk) the noise reaches a steady level, and the detection limit becomes roughly constant. At smaller separations, however, it strongly depends on angular distance from the primary star. This behavior is summarized with a contrast curve (Figure 26). The contrast curve plots the faintest detectable companion (in terms of brightness difference,  $\Delta m$ ) as a function of separation from the primary star. In other words, it tells you: If there had been a companion this bright at this distance, we would have seen it.

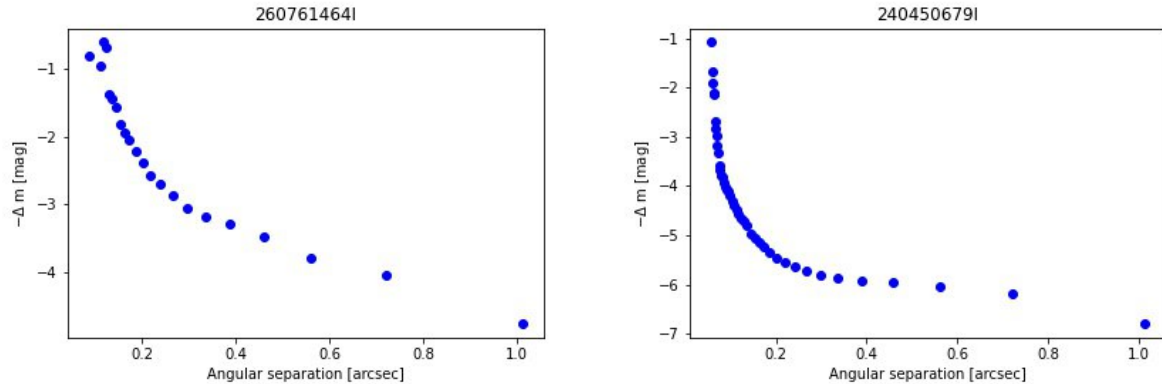


**Figure 26.** The  $5\sigma$  Contrast curves. (a) The curve is for a star with a magnitude of 12, while (b) is the curve for a star with a magnitude of 10.

Since no companions were detected in the vast majority of cases, we present for each star only two representative points of the contrast curve, corresponding  $\Delta m = 3$  and  $\Delta m = 4$ .

In total, we obtained 1019 measurements for 391 selected wide binaries. Many targets were observed two or more times, allowing us to retain only the highest-quality measurements for each system. The table 10 lists the results for 782 stars.

**Table 10. Summary of Speckle Observations**

Comment	Identifier	Julian Year	Dm 4	Dm 3
	Gaia DR3 1003223584897948160	2024.8650	0.28	0.20
	Gaia DR3 1003223614961194752	2024.8650	0.38	0.27
	Gaia DR3 1020666649676726784	2025.2123	0.26	0.20
	Gaia DR3 1020667714828594304	2025.2123	0.37	0.26
	Gaia DR3 1023887978228642176	2025.2176	0.31	0.22
	Gaia DR3 1023888012588380032	2024.8680	0.25	0.18
	Gaia DR3 1028432805245868544	2024.8680	0.24	0.17
	Gaia DR3 1028432805250731264	2024.8680	0.26	0.19
	Gaia DR3 104998928046427264	2024.6869	0.32	0.22
	Gaia DR3 105004842216905344	2024.6869	0.32	0.22
	Gaia DR3 1159502154714284544	2025.4422	1.00	0.61
	Gaia DR3 1159502498311670144	2025.4422	0.19	0.14
	Gaia DR3 1172915990414659328	2025.4393	0.18	0.12
	Gaia DR3 1172920487244742912	2025.4393	0.19	0.13
	Gaia DR3 1174143182830505856	2025.4448	0.17	0.12
	Gaia DR3 1174143182830505984	2025.4448	0.11	0.10
	Gaia DR3 1178121422057906688	2025.4393	0.19	0.13
	Gaia DR3 1178121422057907200	2025.4393	0.27	0.19
	Gaia DR3 1182257922240686720	2025.4339	1.33	1.01
	Gaia DR3 1182257922240687232	2025.4339	1.27	0.90
	Gaia DR3 1214182826468995584	2025.4367	0.45	0.30
	Gaia DR3 1214182826468995840	2025.4367	0.55	0.34
	Gaia DR3 121690893241571968	2024.8618	0.92	0.49
	Gaia DR3 121691266902954240	2024.8618	0.64	0.37
	Gaia DR3 1224242120913963776	2025.4340	0.40	0.27
	Gaia DR3 1224242120913963904	2025.4340	0.39	0.25
	Gaia DR3 1227416514060783232	2025.4448	0.45	0.31
	Gaia DR3 1227417304334766208	2025.4366	0.27	0.21
	Gaia DR3 1247610934890765184	2025.4420	0.53	0.36
	Gaia DR3 1247610934890765312	2025.4420	0.39	0.26
	Gaia DR3 1258410612976538368	2025.4393	0.10	0.09
	Gaia DR3 1258410750415492864	2025.4393	0.13	0.11
	Gaia DR3 1271824002003198464	2025.4367	0.98	0.59
	Gaia DR3 1271824002003198976	2025.4367	0.98	0.58
	Gaia DR3 1274562370068531712	2025.4367	0.19	0.13
	Gaia DR3 1274568245587206144	2025.4367	0.13	0.11
	Gaia DR3 1282815063829295360	2025.4393	0.10	0.09
	Gaia DR3 1282817022334383104	2025.4394	0.11	0.10
	Gaia DR3 1282817022334383232	2025.2182	0.18	0.13
	Gaia DR3 1297419700686304896	2025.4341	0.84	0.45
	Gaia DR3 1297419808063095936	2025.4342	0.71	0.40
	Gaia DR3 1299746168507031424	2025.4450	0.17	0.12
	Gaia DR3 1299746168508720384	2025.4450	0.17	0.12
	Gaia DR3 1302449489644570496	2025.4395	0.00	0.00
	Gaia DR3 1302543326089734144	2025.4395	1.07	0.65
	Gaia DR3 1305035575352515840	2025.4396	0.50	0.32
	Gaia DR3 1305036228187622912	2025.4396	0.00	0.00
	Gaia DR3 1306220264772422016	2025.4450	0.29	0.21
	Gaia DR3 1306220642729543936	2025.4450	0.28	0.20

**Table 10** *continued*

**Table 10** (*continued*)

Gaia DR3 1308215328620272256	2025.4450	0.28	0.20
Gaia DR3 1308215328620272384	2025.4450	0.26	0.19
Gaia DR3 1320009686772023296	2025.4367	0.34	0.23
Gaia DR3 1320009721131760640	2025.4367	0.27	0.19
Gaia DR3 1320379809873587968	2025.4396	0.38	0.27
Gaia DR3 1321677920789034752	2025.4341	0.45	0.30
Gaia DR3 1321677920789214080	2025.4341	0.69	0.42
Gaia DR3 1327463825851820800	2025.4450	0.28	0.19
Gaia DR3 1327463825851820928	2025.4450	0.26	0.18
Gaia DR3 1331462302965590144	2025.4396	0.00	0.00
Gaia DR3 1331462302965590400	2025.4396	0.19	0.13
Gaia DR3 1332438183958298496	2025.4423	0.40	0.28
Gaia DR3 1332438188254551808	2025.4423	0.49	0.33
Gaia DR3 1332473922382506624	2025.4341	1.32	1.01
Gaia DR3 1332473922382951424	2025.4341	1.02	0.57
Gaia DR3 1346694112423491712	2025.4370	0.91	0.53
Gaia DR3 1346694146783637504	2025.4370	0.30	0.22
Gaia DR3 1348285896022947584	2025.4370	0.13	0.11
Gaia DR3 1348286651937191040	2025.4370	0.23	0.16
Gaia DR3 1352381027080312832	2025.4423	0.19	0.14
Gaia DR3 1352427996842670464	2025.4423	0.58	0.38
Gaia DR3 1356763852227145344	2025.4424	1.03	0.73
Gaia DR3 1356763886586884864	2025.4424	0.92	0.59
Gaia DR3 1357040345041982464	2025.4424	0.90	0.58
Gaia DR3 1357040379401720448	2025.4424	0.44	0.31
Gaia DR3 1371903199628510464	2025.4394	0.15	0.12
Gaia DR3 1371903199628531200	2025.4394	0.21	0.13
Gaia DR3 1379737421839743104	2025.4341	0.30	0.21
Gaia DR3 1379737426135359360	2025.4341	0.29	0.20
Gaia DR3 1381408782592655616	2025.4424	0.45	0.31
Gaia DR3 1381455722290898176	2025.4424	1.13	0.80
Gaia DR3 1391176092275606528	2025.4394	0.00	0.00
Gaia DR3 1391176092275606656	2025.4394	0.29	0.20
Gaia DR3 1396388773823564416	2025.4340	0.34	0.24
Gaia DR3 1396388773823907584	2025.4340	0.31	0.22
Gaia DR3 1410982832177435008	2025.4341	1.13	0.72
Gaia DR3 1410982862240353664	2025.4341	0.40	0.27
Gaia DR3 1419999819661235840	2025.4344	0.19	0.13
Gaia DR3 1420000579871414528	2025.4344	0.17	0.12
Gaia DR3 1434064639260540288	2025.4397	0.37	0.27
Gaia DR3 1434064669325509760	2025.4397	1.15	0.78
Gaia DR3 1444305829863259648	2025.4420	0.54	0.36
Gaia DR3 1444305937237949184	2025.4420	0.92	0.60
Gaia DR3 1467776078085413888	2025.4392	0.31	0.22
Gaia DR3 1467776078085414400	2025.4393	0.32	0.23
Gaia DR3 1478999686625786368	2025.4366	0.28	0.21
Gaia DR3 1478999755345263744	2025.4366	0.39	0.28
Gaia DR3 1479430076707007488	2025.4394	0.25	0.17
Gaia DR3 1482432155767129728	2025.4394	0.13	0.11
Gaia DR3 1508470171660833536	2025.4366	0.53	0.33

**Table 10** *continued*

**Table 10** (*continued*)

Gaia DR3 1508470206020209664	2025.4366	0.53	0.34
Gaia DR3 1509241238549271808	2025.4365	0.34	0.25
Gaia DR3 1509241238549292800	2025.4365	0.62	0.39
Gaia DR3 1509783778818258176	2025.4365	0.23	0.18
Gaia DR3 1509783778818258304	2025.4365	0.33	0.25
Gaia DR3 1527328376624427776	2025.4393	0.33	0.24
Gaia DR3 1527328376624971520	2025.4393	0.35	0.26
Gaia DR3 153741691551129216	2024.1277	0.40	0.28
Gaia DR3 153741760270606464	2024.1277	0.40	0.28
Gaia DR3 1543083553620064768	2024.1286	0.00	0.00
Gaia DR3 1543083691059006592	2024.1286	0.38	0.28
Gaia DR3 1549520949383005568	2025.4365	0.28	0.21
Gaia DR3 1549521125478552064	2025.4365	0.18	0.13
Gaia DR3 1585800782946765312	2025.4448	0.46	0.32
Gaia DR3 1585800851666242688	2025.4448	0.25	0.19
Gaia DR3 1586977737129182848	2025.4448	0.20	0.14
Gaia DR3 1586977844504488576	2025.4448	0.13	0.11
Gaia DR3 1590641417247939328	2025.4394	0.00	0.00
Gaia DR3 1590641417247939584	2025.4394	0.82	0.52
Gaia DR3 1592707502675396992	2025.4339	0.38	0.26
Gaia DR3 1592707502675731456	2025.4339	0.37	0.26
Gaia DR3 1595968929041676544	2025.4340	0.48	0.32
Gaia DR3 1595968929041676672	2025.4340	0.44	0.30
Gaia DR3 1605833880509338752	2025.4448	0.29	0.21
Gaia DR3 1605833884804824704	2025.4448	0.40	0.28
Gaia DR3 1610186095424889088	2025.4448	0.21	0.16
Gaia DR3 1610191970940150272	2025.4448	0.27	0.20
Gaia DR3 1610236260642857344	2025.4448	0.32	0.24
Gaia DR3 1610236260642871552	2025.4448	0.32	0.24
Gaia DR3 162781051522771072	2024.8621	0.38	0.26
Gaia DR3 162781051522771200	2024.8621	0.41	0.29
Gaia DR3 167549908330274176	2024.8618	0.64	0.36
Gaia DR3 167549942690010368	2024.8618	0.94	0.54
Gaia DR3 1730273101846974080	2024.6838	0.54	0.34
Gaia DR3 1730273106143055488	2024.6838	0.44	0.31
Gaia DR3 1738269854212128512	2024.6810	0.35	0.24
Gaia DR3 1738269854213155712	2024.6810	0.37	0.26
Gaia DR3 1749987585851186816	2024.6783	0.57	0.34
Gaia DR3 1749987585854235776	2024.6783	1.84	1.33
Gaia DR3 1760471948915107200	2025.4455	0.18	0.13
Gaia DR3 1760477618271932672	2025.4455	0.26	0.18
Gaia DR3 1762461309047562240	2024.6782	0.45	0.30
Gaia DR3 1762461309047562368	2025.4400	0.35	0.24
Gaia DR3 1762461893163118464	2025.4455	0.33	0.23
Gaia DR3 1762461893163118592	2024.6782	0.67	0.37
Gaia DR3 1778929480673414784	2024.6838	0.23	0.16
Gaia DR3 1778930240883745536	2024.6839	0.00	0.00
Gaia DR3 1781495706454162944	2024.6866	0.27	0.18
Gaia DR3 1781495710748864256	2024.6866	0.23	0.16
Gaia DR3 1789024749766697088	2024.6810	1.16	0.85

**Table 10** *continued*

**Table 10** (*continued*)

The third component is DR3 181318611409243136, no parallax data available.	Gaia DR3 1789024857138962048	2024.6810	0.20	0.14
	Gaia DR3 181312735893067008	2024.8650	0.20	0.15
The third component is DR3 181318611409243136, no parallax data available.	Gaia DR3 181318611408327552	2024.8650	0.17	0.12
The third component, DR3 1815165879238575232, is too far away, DM=4.3	Gaia DR3 1815165535636339072	2025.4400	0.16	0.12
	Gaia DR3 1861752775327557504	2024.6781	0.37	0.25
	Gaia DR3 1861752775327558656	2024.6781	0.45	0.30
	Gaia DR3 1868257722327168768	2024.6811	0.72	0.38
	Gaia DR3 1868257726634854784	2024.6811	0.67	0.36
	Gaia DR3 1868985324150840192	2024.6864	0.22	0.14
	Gaia DR3 1868985328454953856	2024.6864	0.24	0.15
	Gaia DR3 1871558941576158464	2024.6810	0.38	0.25
	Gaia DR3 1871559697490418816	2025.4455	0.46	0.30
	Gaia DR3 1894003238061739648	2024.6864	1.01	0.61
	Gaia DR3 1894003238061739776	2024.6864	1.19	0.74
	Gaia DR3 1895940302674258304	2024.6865	1.26	0.82
	Gaia DR3 1895940302674258688	2024.6865	0.28	0.19
	Gaia DR3 1899383114098895616	2024.6864	0.28	0.19
	Gaia DR3 1899383114098895872	2024.6864	0.33	0.22
	Gaia DR3 1902676117063909888	2024.6865	0.43	0.29
	Gaia DR3 1902679033343158528	2024.6865	0.43	0.28
	Gaia DR3 1904247284819944448	2024.6865	0.35	0.25
	Gaia DR3 1904247284820463104	2024.6865	0.25	0.17
	Gaia DR3 1909810023381344768	2024.6866	0.40	0.27
	Gaia DR3 1909810126460559616	2024.6866	0.43	0.29
	Gaia DR3 1910071432270904832	2024.6866	0.37	0.25
	Gaia DR3 1910071535350120192	2024.6866	0.42	0.28
	Gaia DR3 1921150828692050304	2024.6866	0.51	0.34
	Gaia DR3 1921150832986231680	2024.6866	1.19	0.79
	Gaia DR3 1923116072583279232	2024.6865	0.24	0.16
	Gaia DR3 1923116072583279488	2024.6759	0.60	0.39
	Gaia DR3 1931673464205703936	2024.6865	0.55	0.34
	Gaia DR3 1931673532926948864	2024.6865	0.96	0.52
	Gaia DR3 1932297578791924992	2024.6865	0.22	0.14
	Gaia DR3 1932297578791925760	2024.6865	0.22	0.14
	Gaia DR3 1938247517245907456	2024.6866	0.17	0.12
	Gaia DR3 1938247654684985344	2024.6866	0.15	0.12
	Gaia DR3 1942018494236897792	2024.6866	0.62	0.36
	Gaia DR3 1942018498533031808	2024.6866	0.56	0.34
	Gaia DR3 1942384773344557056	2024.6865	0.20	0.13
	Gaia DR3 1942384872124424704	2024.6865	0.32	0.22
	Gaia DR3 1960631100090155008	2024.6838	0.11	0.10
	Gaia DR3 1960631100090155264	2024.6838	0.27	0.20
	Gaia DR3 1967282939282261120	2025.4455	0.22	0.15
	Gaia DR3 1967283042361454848	2025.4455	0.13	0.11
	Gaia DR3 1971147791380289536	2024.6837	0.23	0.16
	Gaia DR3 1971148100617936128	2024.6837	0.00	0.00
	Gaia DR3 1985752226366174720	2024.6865	0.49	0.33

**Table 10** *continued*

**Table 10** (*continued*)

The third component, DR3 1815165879238575232, is too far away, DM=4.3	Gaia DR3 1985752226366174848	2024.6865	0.25	0.17
The third component, DR3 2005665584530878848, is too far away, DM=4.4	Gaia DR3 1994221730075916800	2024.6759	0.88	0.58
The third component, DR3 2005665584530878848, is too far away, DM=4.4	Gaia DR3 1994221936234345344	2024.6759	1.35	1.07
	Gaia DR3 200266181758708736	2024.8649	1.06	0.65
	Gaia DR3 200266250476976768	2024.8649	0.36	0.25
	Gaia DR3 2005665584549011328	2025.4400	0.21	0.15
	Gaia DR3 2005665584549011328	2024.6867	0.33	0.23
	Gaia DR3 2005665962510573824	2024.6867	0.40	0.28
	Gaia DR3 2021978621937192832	2025.4371	1.04	0.60
	Gaia DR3 2021979584009866368	2025.4371	0.42	0.28
	Gaia DR3 2021979588354850176	2025.4371	2.05	1.73
	Gaia DR3 2029432043779954432	2025.4400	0.83	0.45
	Gaia DR3 2029433521248546304	2025.4400	0.10	0.09
	Gaia DR3 2032121960300897280	2025.4398	1.10	0.61
	Gaia DR3 2047012822409354752	2025.4399	0.52	0.32
	Gaia DR3 2047014368597597696	2025.4399	0.45	0.29
	Gaia DR3 2051915235490493952	2025.4399	0.30	0.22
	Gaia DR3 2051915304209972992	2025.4399	0.30	0.21
	Gaia DR3 2056444914159643008	2025.4426	0.49	0.31
	Gaia DR3 2056444914159643136	2024.6781	0.50	0.33
	Gaia DR3 2056444948519384064	2025.4426	0.51	0.33
	Gaia DR3 2062485390533084544	2024.6780	0.30	0.20
	Gaia DR3 2062485390533085568	2024.6780	0.32	0.23
	Gaia DR3 2066763860841212672	2024.6783	1.48	1.12
	Gaia DR3 2066763865140783104	2024.6783	2.93	2.51
	Gaia DR3 2067274450853577344	2025.4455	0.70	0.38
	Gaia DR3 2067274515272929536	2025.4427	0.29	0.20
	Gaia DR3 2076871091425583232	2025.4399	1.29	0.88
	Gaia DR3 2076871091425586944	2025.4399	0.91	0.51
	Gaia DR3 2078886285778453632	2025.4400	0.73	0.41
	Gaia DR3 2078886290079138560	2025.4400	0.59	0.36
	Gaia DR3 2079604404307344128	2025.4372	0.20	0.14
	Gaia DR3 2079604442969955968	2025.4372	0.82	0.49
	Gaia DR3 2086713404118555520	2025.4426	0.37	0.26
	Gaia DR3 2086713404118555648	2025.4426	0.28	0.20
	Gaia DR3 2087586175833524480	2024.6780	0.35	0.25
	Gaia DR3 2087586175833525376	2024.6780	0.23	0.14
	Gaia DR3 2091495764301335424	2025.4452	0.11	0.10
	Gaia DR3 2091495798661081344	2025.4452	0.13	0.11
	Gaia DR3 2098996731404747776	2025.4399	0.53	0.33
	Gaia DR3 2098996731404747904	2025.4399	1.47	1.02
	Gaia DR3 2098996804424367360	2025.4399	0.37	0.25
	Gaia DR3 2099859268216511488	2025.4399	1.14	0.77
	Gaia DR3 2099859268216512000	2025.4399	1.41	0.90
	Gaia DR3 2100011516217168640	2025.4399	1.46	1.03
	Gaia DR3 2100011516217169920	2025.4399	1.49	1.00
	Gaia DR3 210045163010504256	2025.4399	1.26	0.83

**Table 10** *continued*

**Table 10** (continued)

	Gaia DR3 2100451630105041152	2025.4399	0.38	0.26
	Gaia DR3 2100501760964021504	2025.4399	0.37	0.25
	Gaia DR3 2100502001482188032	2025.4399	0.41	0.28
	Gaia DR3 2104998900960077056	2025.4398	0.00	0.00
	Gaia DR3 2104999343337767424	2025.4398	0.60	0.35
	Gaia DR3 211413206732904960	2024.8650	0.34	0.23
	Gaia DR3 211413206732905600	2024.8650	0.37	0.26
	Gaia DR3 2116748243555689728	2025.4397	0.48	0.32
	Gaia DR3 2116748247853607168	2025.4397	0.26	0.18
	Gaia DR3 2116892318236994816	2025.4398	0.22	0.16
	Gaia DR3 2119132916774654080	2025.4398	0.36	0.25
This is a triple system.				
The third component has no Gaia identification;				
its separation from DR3 2119132916774654208 is 0.334''.				
This is a triple system.	Gaia DR3 2119132916774654208	2025.4398	1.11	0.73
The third component has no Gaia identification;				
its separation from DR3 2119132916774654208 is 0.334''.				
	Gaia DR3 2126777988630768000	2025.4400	0.75	0.44
	Gaia DR3 2126777992924832128	2025.4400	1.00	0.65
	Gaia DR3 2128304179486008704	2025.4426	0.37	0.26
	Gaia DR3 2128304183783972992	2025.4426	0.28	0.20
	Gaia DR3 2129540099271049216	2025.4426	0.82	0.46
	Gaia DR3 2129540103571086592	2025.4426	0.99	0.56
	Gaia DR3 2130903047014230528	2025.4426	0.63	0.37
	Gaia DR3 2130903223113004032	2025.4426	0.33	0.23
	Gaia DR3 2137630172689997824	2025.4372	0.31	0.21
	Gaia DR3 2137630172690002176	2025.4372	0.29	0.20
	Gaia DR3 2140767319879292160	2025.4372	0.39	0.28
	Gaia DR3 2140767560397457536	2025.4453	0.29	0.21
	Gaia DR3 2148617626742496512	2025.4371	0.29	0.20
	Gaia DR3 2148617729821714688	2025.4371	0.43	0.29
	Gaia DR3 2157622725756418816	2025.4398	0.29	0.21
	Gaia DR3 2157623451608162688	2025.4398	0.88	0.47
	Gaia DR3 2171870747199482496	2024.6864	1.03	0.59
	Gaia DR3 2171870751495498752	2024.6864	0.67	0.38
	Gaia DR3 2179261496856372224	2024.6864	0.93	0.58
	Gaia DR3 2179261496856372352	2024.6864	0.92	0.56
	Gaia DR3 2182397334073261568	2024.6782	1.03	0.62
	Gaia DR3 2182397338377483264	2024.6782	0.84	0.47
	Gaia DR3 2186439383632375296	2024.6863	2.40	1.77
	Gaia DR3 2186439482412215808	2024.6863	0.62	0.40
	Gaia DR3 219593745044391552	2024.8618	0.37	0.26
	Gaia DR3 219605599154126976	2024.8618	0.49	0.32
	Gaia DR3 2196841961921480960	2024.6864	0.86	0.53
	Gaia DR3 2196841966222594944	2024.6864	1.75	1.40
	Gaia DR3 2201661091331626752	2024.6867	0.25	0.18
	Gaia DR3 2201661297490052096	2024.6867	0.24	0.17
	Gaia DR3 2201834466266276864	2024.6867	0.23	0.16
	Gaia DR3 2201834470572701952	2024.6867	0.28	0.20
	Gaia DR3 222299432702445184	2024.8618	1.45	1.07
	Gaia DR3 222299436999652096	2024.8618	1.48	1.13

**Table 10** *continued*

**Table 10** (*continued*)

Too weak	Gaia DR3 2242465891977167872	2025.4426	0.24	0.17
	Gaia DR3 2242465891977204992	2025.4426	0.43	0.30
	Gaia DR3 229737942400057728	2024.8618	0.59	0.36
	Gaia DR3 229737942400695424	2024.8618	1.75	1.35
	Gaia DR3 2503402743097074304	2024.8618	1.01	0.58
	Gaia DR3 2503402747391938688	2024.8618	0.83	0.45
	Gaia DR3 2512615551025883136	2024.6868	0.95	0.54
	Gaia DR3 251261555321101696	2024.6868	0.31	0.22
	Gaia DR3 2514529598906714880	2024.8618	0.52	0.33
	Gaia DR3 2514541414361083648	2024.8618	> 2..	> 2..
	Gaia DR3 2524864836409161728	2024.6868	0.36	0.26
	Gaia DR3 2529474126591876096	2024.6815	0.41	0.28
	Gaia DR3 2529661799483080192	2024.6815	0.29	0.21
	Gaia DR3 2531509253895359744	2024.6868	0.23	0.17
	Gaia DR3 2531509253895360000	2024.6868	0.29	0.21
	Gaia DR3 2555905080453468544	2024.6815	0.30	0.21
	Gaia DR3 2555905080453468800	2024.6815	0.26	0.19
	Gaia DR3 2556421335522520576	2024.6816	0.29	0.21
	Gaia DR3 2556421610401138176	2024.6816	0.44	0.30
	Gaia DR3 2565584802867037696	2024.6868	0.19	0.13
	Gaia DR3 2565584837226776576	2024.6868	0.21	0.14
	Gaia DR3 2572437745309855488	2024.6869	0.23	0.14
	Gaia DR3 2572437749605558272	2024.6869	0.35	0.24
	Gaia DR3 2573278051366910336	2024.6869	0.16	0.12
	Gaia DR3 2573278120086386432	2024.6869	0.16	0.12
Triple system, variable	Gaia DR3 2581429521337662464	2024.6868	0.26	0.18
	Gaia DR3 2581429521338139264	2024.6868	0.28	0.20
Triple system, variable	Gaia DR3 2586004584926025600	2024.6869	0.30	0.21
	Gaia DR3 2586004589220994560	2024.6869	0.28	0.20
Triple system, variable	Gaia DR3 2611384547405130752	2024.6840	0.34	0.24
	Gaia DR3 2611384547405183488	2024.6840	0.32	0.23
Triple system, variable	Gaia DR3 2621082995876646400	2024.6840	0.31	0.22
	Gaia DR3 2621082995876646528	2024.6840	0.37	0.26
Triple system, variable	Gaia DR3 2638615189818036608	2024.6840	0.13	0.11
	Gaia DR3 2638615189818036736	2024.6840	0.13	0.11
Triple system, variable	Gaia DR3 2642922251741817344	2024.6840	0.51	0.32
	Gaia DR3 2642922286101533696	2024.6840	0.56	0.34
Triple system, variable	Gaia DR3 266993755737826176	2024.8650	1.07	0.65
	Gaia DR3 266993755740665600	2024.8650	1.09	0.68
Triple system, variable	Gaia DR3 2683565561622947584	2024.6839	0.48	0.32
	Gaia DR3 2683565630342923520	2024.6839	0.24	0.17
Triple system, variable	Gaia DR3 2688137537130343936	2024.6838	0.17	0.12
	Gaia DR3 2688137537130451456	2024.6838	0.22	0.16
Triple system, variable	Gaia DR3 2722918766408972288	2024.6839	0.34	0.24
	Gaia DR3 2722918796473758720	2024.6839	0.38	0.26
Triple system, variable	Gaia DR3 2725049173267026560	2024.6838	0.17	0.12
	Gaia DR3 2725049173267027968	2024.6838	0.29	0.21
Triple system, variable	Gaia DR3 2731572610114153856	2024.6840	0.19	0.14
	Gaia DR3 2731572610114154112	2024.6840	0.24	0.18
Triple system, variable	Gaia DR3 2738818666619511808	2024.6868	0.32	0.22

**Table 10** *continued*

**Table 10** (*continued*)

Too weak	Gaia DR3 2738818666619512064	2024.6868	0.35	0.24
	Gaia DR3 2739496687336986112	2024.6841	0.20	0.14
	Gaia DR3 2739498199165473792	2024.6841	0.25	0.18
	Gaia DR3 2741770924059034624	2024.6814	0.48	0.30
	Gaia DR3 2741770958420224000	2024.6814	0.21	0.15
	Gaia DR3 2743364563085132800	2024.6841	1.73	1.42
	Gaia DR3 2743364563085132928	2024.6841	1.77	1.44
	Gaia DR3 2752042939643757952	2024.6868	0.23	0.16
	Gaia DR3 2752042939643758080	2024.6868	0.22	0.15
	Gaia DR3 2763789469038658432	2024.6841	0.23	0.16
	Gaia DR3 2763789469039961472	2024.6841	0.17	0.12
	Gaia DR3 2799550942998190592	2024.6815	0.00	0.00
	Gaia DR3 2799550947293531648	2024.6814	0.42	0.28
	Gaia DR3 280403536989156224	2024.8650	0.32	0.23
Too weak	Gaia DR3 280403541287570176	2024.8650	> 2.	> 2.
	Gaia DR3 2813290096701231104	2024.6840	0.77	0.39
	Gaia DR3 2813290100998398464	2024.6840	0.75	0.40
	Gaia DR3 2833895636096202752	2024.6840	0.32	0.22
	Gaia DR3 2833895636096692224	2024.6757	0.28	0.21
	Gaia DR3 2836313908842872704	2024.6866	0.29	0.19
	Gaia DR3 2836313908842872832	2024.6866	0.25	0.17
	Gaia DR3 2837991381336616320	2024.6867	0.45	0.31
	Gaia DR3 2837991454349643136	2024.6867	0.45	0.30
	Gaia DR3 2847357575430420992	2024.6815	0.26	0.18
	Gaia DR3 2847357575430421120	2024.6815	0.65	0.38
	Gaia DR3 2849031405789315328	2024.6814	0.20	0.13
	Gaia DR3 2849031410085904640	2024.6814	0.33	0.23
	Gaia DR3 2860343426229962752	2024.6814	0.24	0.16
	Gaia DR3 2865611564396936192	2024.6866	0.29	0.21
	Gaia DR3 2865611564396936320	2024.6866	0.35	0.24
	Gaia DR3 2868784063464098048	2024.6866	0.78	0.49
	Gaia DR3 2868784136478476032	2024.6866	0.20	0.13
	Gaia DR3 2874196929143032192	2024.6815	1.22	0.83
	Gaia DR3 2874196929143032448	2024.6815	1.20	0.77
	Gaia DR3 2879160021551346176	2024.6866	0.52	0.34
	Gaia DR3 2879160021551346688	2024.6866	0.43	0.29
	Gaia DR3 293553975230799104	2024.6869	0.31	0.21
	Gaia DR3 293554074014451200	2024.6869	0.21	0.13
	Gaia DR3 2989629982019538304	2024.8621	2.52	1.85
	Gaia DR3 2989630016379276160	2024.8621	2.23	1.86
	Gaia DR3 3002343871195786496	2024.8622	0.38	0.27
	Gaia DR3 3002531548383047296	2024.8622	0.37	0.26
	Gaia DR3 3015129546453825920	2024.8622	1.38	0.95
	Gaia DR3 3015130405447132288	2024.8621	1.34	0.89
	Gaia DR3 3033070586928188416	2024.8624	0.47	0.32
	Gaia DR3 3033070655647665536	2024.8624	1.47	1.16
	Gaia DR3 3033419235197542912	2024.8624	0.74	0.43
	Gaia DR3 3033442909056369792	2024.8624	0.63	0.39
	Gaia DR3 3033693700785580800	2024.8624	0.95	0.56
Too weak	Gaia DR3 303369370078558152	2024.8624	> 2.	> 2.

**Table 10** *continued*

**Table 10** (*continued*)

Too weak	Gaia DR3 3035042522369773824	2024.8624	1.27	0.87
	Gaia DR3 3035042526672692096	2024.8624	1.12	0.83
	Gaia DR3 3042299715729341056	2024.8624	1.03	0.63
	Gaia DR3 3042300093686461312	2024.8624	0.95	0.57
	Gaia DR3 3046204150242468480	2025.2173	0.58	0.37
	Gaia DR3 3046204180298475264	2025.2173	0.43	0.30
	Gaia DR3 3048356684771809536	2024.8624	0.37	0.27
Too weak	Gaia DR3 3048357539467185280	2024.8624	> 2.	> 2.
	Gaia DR3 3061488839331542912	2024.8624	0.90	0.52
	Gaia DR3 3061488839334653696	2024.8624	0.91	0.54
	Gaia DR3 3075884367113894400	2024.8625	1.57	1.30
	Gaia DR3 3075884367113894528	2024.8625	1.22	0.83
	Gaia DR3 3079739250589041024	2024.8625	1.70	1.30
	Gaia DR3 3079739254881696256	2024.8625	1.18	0.68
	Gaia DR3 3084652044636398976	2024.8625	0.35	0.25
	Gaia DR3 3084652044636399104	2024.8625	0.38	0.27
	Gaia DR3 3103862814877943296	2024.8622	0.38	0.27
	Gaia DR3 3103862814877944064	2025.2174	0.45	0.31
	Gaia DR3 3107726150841412224	2024.8624	1.54	1.31
	Gaia DR3 3107726155141310080	2024.8624	1.52	1.25
	Gaia DR3 3155908468358227968	2024.8624	1.20	0.85
	Gaia DR3 3155908575735398400	2024.8624	1.01	0.67
	Gaia DR3 3158878734598549376	2025.2173	0.48	0.31
	Gaia DR3 3158878734598549504	2024.8623	0.63	0.37
	Gaia DR3 3158926322836178816	2025.2173	0.42	0.28
	Gaia DR3 3158926322836178944	2024.8623	0.95	0.49
	Gaia DR3 3170300942420466176	2025.2173	0.28	0.20
	Gaia DR3 3170303755624614528	2024.8623	0.48	0.31
	Gaia DR3 3170303759920420224	2024.8623	0.33	0.23
	Gaia DR3 3170394607068638336	2025.2173	0.30	0.22
	Gaia DR3 3174712286151938944	2024.8621	1.19	0.80
	Gaia DR3 3174712354871414912	2024.8621	0.97	0.58
	Gaia DR3 3194331181363949312	2024.8619	0.96	0.55
	Gaia DR3 3194331284443164288	2024.8619	0.86	0.48
Too weak	Gaia DR3 3194720786437148032	2024.8619	> 2.	> 2.
	Gaia DR3 3194720889516362880	2024.8619	1.08	0.72
	Gaia DR3 3201928153876092416	2024.8620	1.78	1.46
	Gaia DR3 3201928153876683648	2024.8620	1.97	1.60
	Gaia DR3 3208097204381858304	2024.8622	0.78	0.43
	Gaia DR3 3208097582339739136	2024.8622	0.71	0.40
	Gaia DR3 3208920321978859008	2024.8622	0.43	0.30
	Gaia DR3 3208920326274769664	2024.8622	1.48	1.07
Too weak	Gaia DR3 3211638593895777792	2024.8622	> 2.	> 2.
	Gaia DR3 3211638593896898944	2024.8622	0.42	0.28
	Gaia DR3 3213811602532945152	2024.8622	1.48	1.13
	Gaia DR3 3213811641189319680	2024.8622	1.52	1.14
	Gaia DR3 3216741186843662720	2024.8622	2.00	1.60
	Gaia DR3 3216741186843662848	2024.8622	2.88	2.44
Too weak	Gaia DR3 3223175082210855936	2024.8622	> 2.	> 2.
	Gaia DR3 3223175082210856192	2024.8622	1.37	0.88

**Table 10** *continued*

**Table 10** (*continued*)

Too weak	Gaia DR3 3233274852427241216	2024.8620	0.51	0.33
	Gaia DR3 3233274955506455936	2024.8620	> 2.	> 2.
	Gaia DR3 3237157051889659904	2024.8622	0.70	0.40
	Gaia DR3 3237157159265190400	2024.8622	0.83	0.46
	Gaia DR3 3239798461074336512	2024.8649	0.68	0.39
	Gaia DR3 3239798461074336640	2024.8649	0.79	0.43
	Gaia DR3 3242368702645853184	2024.8649	0.83	0.45
	Gaia DR3 3242368706941778688	2024.8649	0.77	0.43
	Gaia DR3 3251884739561945472	2024.8620	2.90	2.34
	Gaia DR3 3251884739561945600	2024.8620	0.93	0.54
	Gaia DR3 3258912371210481152	2024.8620	0.72	0.41
	Gaia DR3 3258912439929957376	2024.8620	1.19	0.83
	Gaia DR3 3266980170921153920	2024.8618	1.18	0.74
Too weak	Gaia DR3 3266980243936341248	2024.8618	> 2.	> 2.
	Gaia DR3 3270823243234194432	2024.8618	1.30	0.93
	Gaia DR3 3270823243234194944	2024.8618	1.09	0.73
	Gaia DR3 3279804084274429440	2024.8620	2.52	2.10
	Gaia DR3 3279804844484336128	2024.8620	0.61	0.36
	Gaia DR3 3285744612456150016	2024.8620	0.32	0.23
	Gaia DR3 3285755951169814528	2024.8620	0.42	0.28
	Gaia DR3 3288572968680438528	2024.8621	0.22	0.15
	Gaia DR3 3288572968680438912	2024.8621	0.20	0.14
	Gaia DR3 3290322734060874752	2024.8649	0.63	0.37
	Gaia DR3 3290322738355773696	2024.8649	0.81	0.42
Too weak	Gaia DR3 329054064352008448	2024.8649	> 2.	> 2.
	Gaia DR3 3290540746599303296	2024.8649	0.63	0.37
	Gaia DR3 3308694065827291648	2024.8621	0.47	0.31
	Gaia DR3 3308694065827292160	2024.8621	0.71	0.39
	Gaia DR3 3338164860103556352	2024.8649	0.40	0.28
	Gaia DR3 3338164860104174592	2024.8649	1.23	0.73
	Gaia DR3 3344333085975753216	2024.8623	0.63	0.37
	Gaia DR3 3344333292134182400	2024.8623	1.06	0.62
	Gaia DR3 3346799805954385408	2024.8649	0.48	0.31
	Gaia DR3 3346799805954387456	2024.8649	0.19	0.14
	Gaia DR3 3360175090027418496	2024.8624	0.44	0.29
	Gaia DR3 3360175090027418880	2024.8624	1.80	1.48
	Gaia DR3 3365948002813451648	2024.8623	1.40	1.00
	Gaia DR3 3365948002813451776	2024.8623	1.45	1.08
	Gaia DR3 3371529368651025664	2024.1278	0.40	0.28
	Gaia DR3 3371529467432172672	2024.1279	0.48	0.33
	Gaia DR3 3399607116051404032	2024.8649	0.59	0.36
Too weak	Gaia DR3 3399608589223938816	2024.8649	> 2.	> 2.
	Gaia DR3 3400637667683964544	2024.8649	0.55	0.34
	Gaia DR3 3400637702043702656	2024.8649	0.41	0.27
	Gaia DR3 3402090259984528768	2024.1278	0.40	0.28
This is a triple system.				
The third component is DR3 3402090466140560128				
This is a triple system.	Gaia DR3 3402090466142958464	2024.1278	0.51	0.33
The third component is DR3 3402090466140560128	Gaia DR3 3410692942038997120	2024.8621	0.39	0.27
	Gaia DR3 3410692942038997760	2024.8621	0.43	0.29

**Table 10** *continued*

**Table 10** (*continued*)

	Gaia DR3 3417608762800814080	2024.8650	0.32	0.23
	Gaia DR3 3417608767098501120	2024.8650	0.37	0.26
	Gaia DR3 3418915433586276096	2024.8649	0.33	0.24
	Gaia DR3 3418915433588729856	2024.8649	1.06	0.56
	Gaia DR3 3451266742171824640	2024.8650	0.20	0.15
	Gaia DR3 3451267120128948992	2024.1278	0.19	0.15
	Gaia DR3 3593154766362734336	2025.2179	0.31	0.23
	Gaia DR3 3593154766362734464	2025.2179	0.31	0.23
	Gaia DR3 3609320267350909696	2025.4392	0.47	0.32
	Gaia DR3 3609320503573212416	2025.4392	0.53	0.36
	Gaia DR3 3609413309226560768	2025.4392	1.15	0.85
	Gaia DR3 3609413485320886528	2025.4392	0.35	0.26
	Gaia DR3 3618102204160590080	2025.4446	0.45	0.32
	Gaia DR3 3618102204160590208	2025.2181	0.27	0.20
	Gaia DR3 3627968323859543680	2025.4446	0.34	0.26
	Gaia DR3 3627968328155313024	2025.4446	1.40	1.06
	Gaia DR3 3629449713915122688	2025.4446	0.25	0.19
	Gaia DR3 3629449713915123072	2025.4446	1.00	0.65
	Gaia DR3 3636691509812473856	2025.4392	0.26	0.18
	Gaia DR3 3636714977513779712	2025.4392	0.31	0.22
	Gaia DR3 3639520621950395776	2025.4447	0.12	0.10
	Gaia DR3 3639520621950395904	2025.4447	0.12	0.10
	Gaia DR3 3641315024925921024	2025.4393	0.27	0.20
The third component has no Gaia identification; its separation from DR3 3641315024925921024 is 0.482	Gaia DR3 3641315024927514880	2025.4393	0.69	0.40
The third component has no Gaia identification; its separation from DR3 3641315024925921024 is 0.482	Gaia DR3 3666150003300751744	2025.4448	0.22	0.16
	Gaia DR3 3666150003300991744	2025.4448	0.25	0.18
	Gaia DR3 367020421620737536	2024.6815	0.28	0.20
	Gaia DR3 367020421621893120	2024.6815	0.26	0.19
	Gaia DR3 3677417214346066048	2025.2180	0.34	0.25
	Gaia DR3 3677417214346902144	2025.2180	0.58	0.37
	Gaia DR3 3680089852236243584	2025.2180	0.23	0.17
	Gaia DR3 3680089852236243712	2025.2180	0.25	0.19
	Gaia DR3 3686259727375524864	2025.4392	0.43	0.29
	Gaia DR3 3686261307923490688	2025.4392	0.25	0.18
	Gaia DR3 3717756234385505792	2025.4446	0.19	0.14
	Gaia DR3 3717756337464721152	2025.4364	0.76	0.50
	Gaia DR3 3718581417862169344	2025.4364	0.35	0.26
	Gaia DR3 3718581520941384320	2025.4447	0.41	0.29
	Gaia DR3 372066046121799168	2024.6870	0.00	0.00
	Gaia DR3 372066076185339648	2024.6869	0.26	0.18
	Gaia DR3 3724521696934640384	2025.4447	0.20	0.14
	Gaia DR3 3724521701229940096	2025.4447	0.34	0.24
	Gaia DR3 3738783878870503424	2025.4365	0.34	0.25
	Gaia DR3 3738783878870503552	2025.4365	0.77	0.53
	Gaia DR3 3739054324371407232	2025.4447	0.43	0.31
	Gaia DR3 3739054324371407488	2025.4447	0.24	0.18
	Gaia DR3 374529119673672576	2024.6870	0.38	0.25
	Gaia DR3 374529123966850944	2024.6870	0.29	0.20

**Table 10** *continued*

**Table 10** (*continued*)

	Gaia DR3 3768566346037170304	2025.2178	0.34	0.25
	Gaia DR3 3768566350332212352	2025.2178	0.34	0.25
	Gaia DR3 377244848968006016	2024.6816	0.26	0.18
	Gaia DR3 377245055126435072	2024.6816	0.22	0.15
	Gaia DR3 3792739899447945216	2024.1285	0.73	0.52
	Gaia DR3 3792740006822516608	2024.1285	1.10	0.89
	Gaia DR3 3793106419072038272	2025.2178	0.26	0.19
	Gaia DR3 3793107930900527616	2025.2178	0.20	0.14
	Gaia DR3 3838561363635304448	2024.8679	0.35	0.25
	Gaia DR3 3838561363635829632	2024.8679	0.34	0.24
	Gaia DR3 3841514200895729152	2024.8679	0.37	0.24
	Gaia DR3 3841514200898362368	2024.8679	0.33	0.23
	Gaia DR3 3890860179670959104	2025.2178	0.25	0.18
	Gaia DR3 3890860183966486656	2025.2178	0.24	0.17
The third component is DR3 3895404602964088448. No parallax information.	Gaia DR3 3895404602962524544	2025.2179	0.20	0.15
The third component is DR3 3895404602964088448. No parallax information.	Gaia DR3 3895404602964117504	2025.2179	0.32	0.23
Too weak	Gaia DR3 3907465249087614976	2025.2179	0.50	0.32
	Gaia DR3 3907466035066193664	2024.1286	> 2.	> 2.
	Gaia DR3 3930274446007361664	2025.4365	0.21	0.16
	Gaia DR3 3930274613510165504	2025.4365	0.17	0.13
This is a multi-component system. One of the components is DR3 3936935287448996864.	Gaia DR3 3936935283153115008	2025.4419	0.24	0.16
This is a multi-component system. One of the components is DR3 3936935287448996864.	Gaia DR3 3936947278997113216	2025.4419	1.03	0.81
	Gaia DR3 3945118265299248128	2025.4447	0.14	0.11
	Gaia DR3 3945118643256370688	2025.4447	0.16	0.12
	Gaia DR3 3974007108685133056	2024.1285	1.00	0.70
	Gaia DR3 3974007585425593472	2025.2179	0.68	0.40
	Gaia DR3 3975566491051012480	2025.2179	0.25	0.18
	Gaia DR3 3975566491051012608	2025.2179	0.25	0.18
	Gaia DR3 4007902062872083456	2024.1285	0.41	0.30
	Gaia DR3 4007902269030513920	2024.1285	0.95	0.70
	Gaia DR3 4025108384759142272	2025.2179	0.60	0.37
	Gaia DR3 405028575795255808	2024.6870	0.26	0.19
	Gaia DR3 405028683170219392	2024.6870	0.31	0.22
	Gaia DR3 4103210548364197376	2025.4452	0.23	0.17
	Gaia DR3 4103210582723957120	2025.4452	0.31	0.24
	Gaia DR3 418549201560407040	2024.6815	0.45	0.32
	Gaia DR3 418549205864071296	2024.6815	0.43	0.30
	Gaia DR3 4197023904013455872	2025.4371	0.19	0.13
	Gaia DR3 4197023904014523776	2025.4371	0.16	0.12
	Gaia DR3 4218533748765026560	2025.4373	0.32	0.23
	Gaia DR3 4218533959216594176	2025.4373	0.77	0.44
	Gaia DR3 4230699329529382400	2025.4373	0.28	0.20
	Gaia DR3 4230699363889120128	2025.4373	0.18	0.13
	Gaia DR3 4231853855392895104	2024.6783	0.94	0.48
	Gaia DR3 4231853855392895360	2024.6783	1.24	0.70
	Gaia DR3 4232150409999693056	2024.6783	0.42	0.29

**Table 10** *continued*

**Table 10** (*continued*)

Gaia DR3 4232150410001183872	2024.6783	0.42	0.29	
Gaia DR3 4243504314963260672	2024.6780	0.36	0.25	
Gaia DR3 4243504314963261696	2024.6780	1.10	0.68	
Gaia DR3 4245247040891396480	2024.6782	1.53	1.23	
Gaia DR3 4245247247049828480	2024.6782	0.41	0.29	
Gaia DR3 4249024035142729728	2024.6782	1.19	0.74	
Gaia DR3 4249024035142730368	2024.6782	0.38	0.26	
Gaia DR3 428811394564909568	2024.6814	0.24	0.17	
Gaia DR3 428811428924644352	2024.6814	0.32	0.23	
Gaia DR3 4292414749731991808	2025.4371	0.31	0.21	
Gaia DR3 4292415883603395456	2025.4371	0.46	0.30	
Gaia DR3 4335277282059878656	2025.4343	0.53	0.36	
Gaia DR3 4335277282066850048	2025.4343	0.56	0.37	
Gaia DR3 4350763323519241600	2025.4343	0.63	0.39	
Gaia DR3 4350763323519241984	2025.4343	0.80	0.45	
Gaia DR3 4353764371788098944	2025.4369	0.36	0.26	
Gaia DR3 4353764436210206080	2025.4369	0.26	0.19	
Gaia DR3 4368065856969737728	2025.4396	0.20	0.15	
Gaia DR3 4368065921391001600	2025.4396	0.77	0.42	
Gaia DR3 4385319393432940544	2025.4395	0.81	0.44	
Gaia DR3 4385319427793947648	2025.4395	0.32	0.22	
Gaia DR3 4390274857979921408	2025.4396	0.47	0.31	
Gaia DR3 4390274857979922432	2025.4396	0.26	0.19	
Gaia DR3 4395522998779760128	2025.4367	0.29	0.21	
Gaia DR3 4395523033138822656	2025.4367	0.29	0.21	
Gaia DR3 4404091664690806016	2025.4340	0.23	0.17	
Gaia DR3 4404091664691143168	2025.4340	0.28	0.20	
Gaia DR3 4407541313703639424	2025.4369	1.07	0.69	
Gaia DR3 4407544268641139712	2025.4369	1.12	0.74	
Gaia DR3 441620979895171840	2024.8619	0.30	0.22	
Gaia DR3 441620979901788544	2024.8619	0.64	0.39	
Gaia DR3 4430185034123000960	2025.4341	0.26	0.19	
Gaia DR3 4430185068482324864	2025.4367	0.24	0.17	
Gaia DR3 4435683451255623808	2025.4395	0.24	0.17	
Gaia DR3 4435689739087756800	2025.4395	0.11	0.10	
Gaia DR3 4441920942064076288	2025.4395	0.47	0.31	
Gaia DR3 4441920946360132096	2025.4395	0.37	0.25	
Gaia DR3 4445849153513150080	2025.4450	0.25	0.18	
Gaia DR3 4445849157808061312	2025.4450	0.25	0.18	
Gaia DR3 4451719690908056192	2025.4341	0.28	0.20	
Gaia DR3 4451731819895701376	2025.4341	1.02	0.64	
Gaia DR3 4454413455738305792	2025.4341	0.60	0.38	
Gaia DR3 4454413460037125888	2025.4341	0.62	0.38	
Gaia DR3 4466613022581649152	2025.4343	0.78	0.48	
Gaia DR3 4466613022581649664	2025.4343	0.64	0.41	
Gaia DR3 4471562916556377856	2025.4397	0.27	0.20	
Gaia DR3 4471658131695403264	2025.4397	0.77	0.41	
Gaia DR3 4474801218817508864	2025.4370	0.72	0.41	
Gaia DR3 4474801257476653952	2025.4370	0.34	0.24	
The third component is DR3 4493544082437142784 ,	Gaia DR3 4493544082437142400	2025.4370	0.84	0.49

**Table 10** *continued*

**Table 10** (*continued*)

no parallax data available.					
The third component is DR3 4493544082437142784 ,	Gaia DR3 4493544185516358656	2025.4370	0.84	0.47	
no parallax data available.					
	Gaia DR3 4502416488439872128	2025.4370	0.24	0.17	
	Gaia DR3 4502416488439872256	2025.4370	0.26	0.18	
	Gaia DR3 4513425898394508288	2025.4398	0.31	0.22	
	Gaia DR3 4513425932752582144	2025.4398	0.42	0.28	
	Gaia DR3 4513771449965175296	2025.4398	0.60	0.36	
	Gaia DR3 4513771832248074240	2025.4398	1.31	0.92	
	Gaia DR3 4541750383049979904	2025.4396	0.38	0.26	
	Gaia DR3 4541753303627759104	2025.4396	0.24	0.17	
	Gaia DR3 4544016820111855360	2025.4370	0.20	0.14	
	Gaia DR3 4544017129349496832	2025.4370	0.32	0.22	
	Gaia DR3 4558397710654524288	2025.4344	0.26	0.20	
	Gaia DR3 4558397710655578368	2025.4344	0.38	0.28	
	Gaia DR3 4571298692894669824	2025.4344	0.77	0.44	
	Gaia DR3 4571298692894670336	2025.4344	0.91	0.50	
	Gaia DR3 4572807566444752128	2025.4395	0.32	0.22	
	Gaia DR3 4577271961615916032	2025.4370	0.33	0.23	
	Gaia DR3 4577272270853565952	2025.4370	0.21	0.15	
	Gaia DR3 4584470704757139968	2025.4397	0.46	0.30	
	Gaia DR3 4584470739116876800	2025.4397	0.35	0.23	
	Gaia DR3 4589844945796230016	2025.4452	0.17	0.12	
	Gaia DR3 4589850065397245824	2025.4452	0.30	0.21	
	Gaia DR3 459661938487951360	2024.8617	0.49	0.32	
	Gaia DR3 459661938487952000	2024.8617	0.98	0.56	
	Gaia DR3 4599117333509619200	2025.4397	1.12	0.63	
	Gaia DR3 4599118119486450688	2025.4397	0.70	0.37	
	Gaia DR3 4599984504586131456	2025.4397	0.23	0.17	
	Gaia DR3 4599984642025088128	2025.4397	0.14	0.11	
	Gaia DR3 4600068239268380928	2025.4370	0.00	0.00	
	Gaia DR3 4600068239268381312	2025.4370	0.27	0.19	
	Gaia DR3 460621193663868160	2024.8617	0.34	0.25	
	Gaia DR3 460621296743080960	2024.8617	1.24	0.84	
	Gaia DR3 4724021644644224	2024.8617	1.23	0.86	
	Gaia DR3 4725155516009856	2024.8617	1.15	0.77	
	Gaia DR3 5110662129034491904	2024.8619	1.02	0.62	
	Gaia DR3 5110662129034492032	2024.8619	0.61	0.37	
	Gaia DR3 5114544745110388736	2024.8619	0.70	0.41	
	Gaia DR3 5114547700047887360	2024.8619	0.88	0.50	
	Gaia DR3 5166931251492281472	2024.8619	1.24	0.89	
Too weak	Gaia DR3 51669313595089502208	2024.8619	> 2.	> 2.	
	Gaia DR3 5169322066511702016	2024.8619	0.51	0.33	
	Gaia DR3 5169322070807079552	2024.8619	0.77	0.45	
Too weak	Gaia DR3 5181911234131665920	2024.8619	> 2.	> 2.	
	Gaia DR3 5181911238426924288	2024.8619	0.42	0.29	
	Gaia DR3 53720557585606912	2024.8621	1.14	0.73	
	Gaia DR3 53720561882110336	2024.8621	1.04	0.62	
	Gaia DR3 5737419559713009024	2024.8625	2.01	1.69	
	Gaia DR3 5737419559713009152	2024.8625	1.11	0.69	

**Table 10** *continued*

**Table 10** (*continued*)

	Gaia DR3 5741344919302959104	2024.8679	0.24	0.18
	Gaia DR3 5741344919302959360	2025.2123	0.29	0.23
	Gaia DR3 5741345125461458944	2024.8679	0.25	0.19
	Gaia DR3 5741345125461459200	2025.2123	0.26	0.20
	Gaia DR3 5755402484702384128	2024.8625	0.42	0.29
	Gaia DR3 5755402720924702720	2024.8625	0.76	0.43
	Gaia DR3 57604756957776013568	2024.8625	1.44	1.02
	Gaia DR3 5760475695777562880	2024.8625	1.37	1.00
	Gaia DR3 579529081235551360	2024.8679	0.19	0.12
	Gaia DR3 579529081235551488	2024.8679	0.18	0.12
	Gaia DR3 594453852070106624	2024.8679	0.19	0.11
	Gaia DR3 594453852070765696	2025.2176	0.25	0.18
	Gaia DR3 601946577137602816	2024.8625	2.29	1.90
	Gaia DR3 601946955094723968	2024.8625	0.77	0.43
	Gaia DR3 619889232512875648	2024.8679	0.25	0.18
	Gaia DR3 619890709981625344	2024.8679	0.28	0.20
	Gaia DR3 6321593106912540288	2025.4340	0.53	0.36
	Gaia DR3 6321593111208064384	2025.4340	0.42	0.30
	Gaia DR3 6321929729270985472	2025.4339	0.24	0.19
	Gaia DR3 6321929733564266752	2025.4339	0.18	0.12
	Gaia DR3 633627316769035264	2024.8679	0.40	0.27
	Gaia DR3 633627321064388096	2024.8679	0.33	0.23
	Gaia DR3 639517366199833344	2024.8679	0.30	0.21
	Gaia DR3 639517366199833472	2024.8679	0.27	0.19
	Gaia DR3 644549800855341184	2024.8680	0.25	0.18
Too weak	Gaia DR3 644549869574817792	2024.8680	> 2.	> 2.
	Gaia DR3 644936691509435520	2024.8680	0.33	0.23
	Gaia DR3 644936691509435648	2025.2177	0.37	0.26
	Gaia DR3 648508863053616384	2025.2177	0.28	0.20
	Gaia DR3 648508867348963840	2024.8680	0.60	0.36
Too weak	Gaia DR3 656657519823458688	2024.8652	> 2.	> 2.
	Gaia DR3 656657622902671488	2024.8652	0.66	0.37
	Gaia DR3 661127824863058176	2024.1279	0.24	0.18
	Gaia DR3 661128752575993600	2024.8652	0.28	0.20
Too weak	Gaia DR3 668946623847575936	2024.8652	> 2.	> 2.
	Gaia DR3 668947001804697472	2024.8652	0.45	0.30
	Gaia DR3 675639449909479040	2024.8652	1.28	0.83
	Gaia DR3 675639449911182336	2024.8652	1.30	0.86
	Gaia DR3 680661782802091392	2025.2175	0.58	0.34
	Gaia DR3 680662573076074752	2024.8652	0.32	0.22
	Gaia DR3 6840365615137220608	2024.6838	0.29	0.22
	Gaia DR3 6840365718216434688	2024.6838	0.22	0.16
	Gaia DR3 6903444700303516160	2024.6782	0.46	0.32
	Gaia DR3 6903444700303516800	2024.6782	0.95	0.50
	Gaia DR3 6906039925703317248	2024.6781	0.29	0.21
	Gaia DR3 6906039925703317376	2024.6781	0.29	0.21
	Gaia DR3 6909250362214709248	2024.6839	0.38	0.27
	Gaia DR3 6909250362214915072	2024.6839	0.35	0.25
	Gaia DR3 6912178464759019520	2024.6839	0.38	0.27
	Gaia DR3 6912178464759020544	2024.6839	0.45	0.32

**Table 10** *continued*

**Table 10** (*continued*)

Too weak	Gaia DR3 695440421670598400	2024.8680	0.31	0.22
	Gaia DR3 695440421670598656	2024.8680	0.32	0.21
	Gaia DR3 710817744619067520	2024.8652	1.50	1.24
	Gaia DR3 710817744619067648	2024.8652	0.40	0.26
	Gaia DR3 758958211973432704	2025.2179	0.26	0.19
	Gaia DR3 758958929232265472	2025.2179	0.43	0.29
	Gaia DR3 77161217776670208	2024.8617	0.30	0.21
	Gaia DR3 77161222072044288	2024.8617	0.28	0.19
	Gaia DR3 787833483266126080	2025.2123	0.34	0.25
	Gaia DR3 787833551986183168	2025.2123	0.31	0.22
	Gaia DR3 796311542548505984	2024.8680	0.27	0.19
	Gaia DR3 796311954865365888	2024.1279	1.19	0.89
	Gaia DR3 803485581043936768	2025.2123	0.41	0.28
	Gaia DR3 803485615403673728	2025.2123	0.30	0.22
	Gaia DR3 817937454502566528	2024.8680	0.41	0.28
	Gaia DR3 817937458796755200	2024.8680	0.53	0.34
	Gaia DR3 820692212165053056	2024.8680	0.19	0.12
	Gaia DR3 820692216460834944	2025.2177	0.20	0.14
	Gaia DR3 853328573431352576	2025.2178	0.39	0.28
	Gaia DR3 853328573431352704	2025.2178	0.32	0.24
	Gaia DR3 87111458705996800	2024.8617	0.97	0.58
	Gaia DR3 87111905382846976	2024.8617	> 2.	> 2.
Too weak	Gaia DR3 883478861596266880	2024.8623	0.75	0.41
	Gaia DR3 883478865892528128	2024.8623	1.08	0.69
	Gaia DR3 898728439334815616	2024.8650	0.58	0.35
	Gaia DR3 898728439334815744	2024.8650	0.39	0.26
	Gaia DR3 899627393169280384	2024.8651	0.42	0.26
	Gaia DR3 899627393169280512	2024.8651	0.44	0.29
	Gaia DR3 904299046277136768	2024.8652	1.44	0.99
	Gaia DR3 904299046277137024	2024.8652	0.54	0.33
	Gaia DR3 914241517609344128	2024.8652	0.26	0.17
	Gaia DR3 914244399532441472	2024.8652	0.25	0.17
	Gaia DR3 916482150508905856	2024.8652	0.19	0.12
	Gaia DR3 917982605923642752	2024.8652	0.24	0.16
	Gaia DR3 922595430863222144	2024.1279	0.87	0.59
	Gaia DR3 922601585552127104	2024.1279	0.28	0.21
	Gaia DR3 930712128780483840	2024.8652	1.68	1.36
	Gaia DR3 930712133074729856	2024.8652	1.63	1.25
	Gaia DR3 937667952870488704	2024.8623	0.23	0.16
	Gaia DR3 937667952871051776	2025.2174	0.23	0.17
	Gaia DR3 951148377744097024	2024.8651	0.38	0.26
	Gaia DR3 951148446463574016	2024.8651	0.35	0.24
	Gaia DR3 951621305182882432	2024.8650	2.64	2.10
	Gaia DR3 951621305182882944	2024.8650	1.87	1.37
	Gaia DR3 953178312430077312	2024.8651	1.54	1.16
	Gaia DR3 953178312430645376	2024.8651	0.55	0.34
	Gaia DR3 982674365408534400	2024.8651	> 2.	> 2.
	Gaia DR3 982674434128011904	2024.8651	0.54	0.35
	Gaia DR3 98692339803443328	2024.6869	0.23	0.15
	Gaia DR3 98692614681349248	2024.6869	0.14	0.11

**Table 10** *continued*

**Table 10** (*continued*)

---

Gaia DR3 990524191236435200	2024.8651	0.48	0.32
Gaia DR3 990524191236435456	2024.8651	0.39	0.27
Gaia DR3 992789150829982848	2024.1278	0.28	0.21
Gaia DR3 992789872384490496	2024.8650	0.29	0.21

---